PERFORMANCE INVESTIGATION OF A PILOT-SCALE INTEGRATED ANAEROBIC DIGESTION-SOLID-OXIDE FUEL CELL SYSTEM CALIBRATED TO EXPERIMENTAL STACK DATA

ENQUÊTE DE PERFORMANCE SUR UN SYSTÈME À L'ÉCHELLE PILOTE DE PILES À COMBUSTIBLE À OXYDE SOLIDE INTÉGRÉ À LA DIGESTION ANAÉROBIE ET CALIBRÉ AVEC DONNÉES DE PILES EXPÉRIMENTALES

A Thesis Submitted
to the Division of Graduate Studies of the Royal Military College of Canada
by

Stephen Trevor Wartman, B.A.Sc.

In Partial Fulfillment of the Requirements for the Degree of
Master of Applied Science

September 2014

ACKNOWLEDGEMENTS

At the onset, I would like to thank some of the major contributors to this work. First, I would like to thank my primary supervisors, Drs. Thurgood and Peppley, for the expertise and advice they consistently provided. I would also like to thank Dr. Champagne who played a critical role in securing and managing the funding for this work; her contributions are graciously acknowledged here.

I would like to thank Gordon McAlary of Canadian Shield Energy Systems (CanSES) and Simon Chun for their assistance during the construction phase of the experimental apparatus. Additionally, Mr. McAlary's physical presence during the experiments was much appreciated.

I would also like to thank the colleagues who I interacted with on a daily basis: Dr. Wojtek Halliop, Dr. Ela Halliop, Rajesh Parmar, Mayur Mundhwa, Harsh Dhingra, Dr. Aidu Qi, Alexandru Sonoc, and Matthew Williston all provided insights which helped shape the final outcome of this project.

Lastly, but far from least, I would like to thank my parents. Though not direct contributors, their ongoing love and support significantly contributed to the final outcome of this work.

ABSTRACT

Wartman, S. Trevor, M.A.Sc., Royal Military College of Canada, September 2014; Performance investigation of a pilot-scale integrated anaerobic digestion-tubular solid-oxide fuel cell system calibrated to experimental stack data; Dr. C. Thurgood, principal supervisor, Royal Military College of Canada, Kingston, Ontario, and Dr. B. A. Peppley, co-supervisor, Queen's University, Kingston, Ontario.

Biogas is a renewable-energy by-product produced at many wastewater treatment plants (WWTPs) by anaerobic digestion. Unfortunately, biogas is currently underutilized at smaller facilities because of the capital and maintenance capital costs associated with combined heat and power (CHP) technologies and biogas purification. Solid oxide fuel cell (SOFC) systems are a CHP technology currently entering commercial markets that could lead to a rise in biogas utilization at WWTPs because they are the CHP technology with the highest electrical efficiencies and most environmentally-friendly emissions profiles.

A $2kW_e$ biogas-fed SOFC pilot plant has been proposed for construction at the Ravensview wastewater treatment plant in Kingston, ON, that is to be directly integrated with one of the on-site digesters. Importantly, the pilot plant will include a biogas purification system comprised of inexpensive adsorbents that selectively targets the two most detrimental contaminant species, hydrogen sulphide and siloxanes.

This work began with an experimental component in which a prospective SOFC stack for the pilot plant was operated on processed biogas. Subsequently, a process model of the pilot plant was developed using the UniSim Design™ simulation software. The process model is enhanced by the inclusion of a tunable empirical cell model that was calibrated to the prospective stack performance. A series of sensitivity analyses were performed on the pilot plant model which revealed that the system could be operated on the expected range of biogas compositions generated at WWTPs. The maximum feasible gross electrical and CHP efficiencies were estimated to be 62 and 77 % for operation on Ravensview biogas.

KEYWORDS: biogas, solid-oxide fuel cell, anaerobic digestion, integrated system, pilot plant, combined heat and power, biogas purification, siloxane, hydrogen sulphide, activated carbon, activated alumina, wastewater treatment, sensitivity analysis.

RÉSUMÉ

Wartman, S. Trevor, M.Sc.A, Collège militaire royal du Canada, septembre 2014; Enquête de performance sur un système à l'échelle pilote de piles à combustible à oxyde solide intégré à la digestion anaérobie et calibré avec données de piles expérimentales; Dr. C. Thurgood, directeur, Collège militaire royal du Canada, Kingston, Ontario, et Dr. B. A. Peppley, directeur, l'Université Queen's, Kingston, Ontario.

Le biogaz est un sous-produit de l'énergie renouvelable produite dans de nombreuses usines de traitement des eaux usées par digestion anaérobie. Malheureusement, le biogaz est actuellement sous-utilisé à des installations plus petites en raison des coûts d'investissement et d'entretien associés aux technologies de cogénération et de purification de biogaz. Les systèmes de piles à combustible à oxyde solide (SOFC) sont une technologie de cogénération entrant actuellement les marchés commerciaux qui pourrait conduire à une augmentation de l'utilisation du biogaz aux stations d'épuration, car ils sont une technologie de cogénération avec les efficacités électriques les plus élevées et les profils d'émissions les plus respectueuses de l'environnement.

Une usine pilote SOFC, alimentée au biogaz et avec une capacité de 2 kW_e a été proposé pour être intégré directement avec l'un des digesteurs à l'usine de traitement des eaux usées Ravensview à Kingston, ON. Fait important, l'installation pilote comprend un système de purification de biogaz constitué d'adsorbants peu coûteux qui cible sélectivement les deux impuretés les plus néfastes, le sulfure d'hydrogène et les siloxanes.

Ce travail a commencé avec un composant expérimental dans lequel une pile SOFC prospective pour l'usine pilote a été opéré avec biogaz traité. Par la suite, un modèle de procédés de l'usine pilote a été développé en utilisant le logiciel de simulation UniSim Design^{TM}. Le modèle de procédés a été renforcé par l'inclusion d'un modèle empirique de cellules qui a été réglé selon la pile prospective. Une série d'analyses de sensibilité ont été réalisées sur le modèle de l'usine pilote qui a révélé que le système pourrait être utilisé sur le rang de compositions de biogaz générés aux stations d'épuration. Les efficacités maximales réalisables de chaleur et d'énergie électrique combinée bruts ont été estimées à 62 et 77% pour le fonctionnement au biogaz produit à Ravensview.

MOTS-CLÉS: biogaz, pile à combustible à oxyde solide, la digestion anaérobie, système intégré, usine pilote, cogénération, purification de biogaz, siloxane, sulfure d'hydrogène, charbon actif, alumine activée, traitement des eaux usées, analyse de sensibilité.

TABLE OF CONTENTS

LIST OF TABLES

LIST OF FIGURES

LIST OF ABBREVIATIONS AND ACRONYMS

AC	Activated carbon/alternating current
AD	Anaeorobic digestion
AGR	Anode gas recycle
APSAT	Advanced Power Systems Analysis Tools
ATR	Autothermal reforming
BD	Boudouard reaction
BOP	Balance-of-plant
CanSES	Canadian Shield Energy Systems
CHP	Combined heat and power
COR	Carbon monoxide reduction reaction
DC	Direct current
DIR	Direct internal reforming
DR	Dry reforming
HHV	Higher heating value
HMCTS	Hexamethylcyclotrisiloxane
HX	Heat exchanger
IIR	Indirect internal reforming
LHV	Lower heating value
MD	Methane decomposition reaction
MeOH	Methanol
MGD	Million gallons per day
MSR	Methane steam reforming
NMVOC	Non-methane volatile organic compound
NH mix	Nitrogen-hydrogen mixture
P&ID	Piping and instrumentation diagram
POX	Partial oxidation
PSOFC	Planar solid oxide fuel cell
SLPM	Standard litre per minute
SOFC	Solid oxide fuel cell
SR	Steam reforming
SSR	Sum of squared residuals
TOTO Ltd.	Tōyō Tōki Limited
TSOFC	Tubular solid oxide fuel cell
TVOC	Total volatile organic compounds
VOC	Volatile organic compound
WGS	Water-gas shift
WWTP	Wastwater treatment plant

LIST OF SYMBOLS AND NOMENCLATURE

A	Total heat exchange area (m^2)
A_{cell}	Total active area of a single cell (cm^2)
α_{BD}	Carbon activity for the Boudouard reaction (unitless)
α_{COR}	Carbon activity for the carbon monoxide reduction reaction (unitless)
α_{MD}	Carbon activity for the methane decomposition reaction (unitless)
C_a	Constant for the $\Delta V_{cell,a}$ empirical correlation (V)
C_c	Constant for the $\Delta V_{cell,c}$ empirical correlation (V)
C_i	Constant for the $\Delta V_{cell,i}$ empirical correlation ($V \cdot cm^2 \cdot mA^{-1}$)
C_p	Constant for the $\Delta V_{cell,p}$ empirical correlation (V)
C_T	Constant for the $\Delta V_{cell,T}$ empirical correlation ($V \cdot K^{-1} \cdot mA^{-1}$)
ΔG_R^o	Standard Gibbs free energy of reaction ($J \cdot mol^{-1}$)
$\Delta G_{R,T,BD}^0$	Standard Gibbs free energy of reaction for the Boudouard reaction calculated at the reactor temperature ($J \cdot mol^{-1}$)
$\Delta G_{R,T,COR}^0$	Standard Gibbs free energy of reaction for the carbon monoxide reduction reaction calculated at the reactor temperature ($J \cdot mol^{-1}$)
$\Delta G_{R,T,MD}^0$	Standard Gibbs free energy of reaction for the methane decomposition reaction calculated at the reactor temperature ($J \cdot mol^{-1}$)
$\Delta G_{R,T_{cell}}^o$	Standard Gibbs free energy of reaction calculated at the average cell temperature ($J \cdot mol^{-1}$)
$\Delta V_{cell,a}$	Empirical correlation that predicts the difference in cell voltage between any two operating points, "1" and "2", in which the only difference between them is their anode composition (V)
$\Delta V_{cell,c}$	Empirical correlation that predicts the difference in cell voltage between any two operating points, "1" and "2", in which the only difference between them is their cathode composition (V)
$\Delta V_{cell,i}$	Empirical correlation that predicts the difference in cell voltage between any two operating points, "1" and "2", in which the only difference between them is their average cell current density (V)

$\Delta V_{cell,p}$	Empirical correlation that predicts the difference in cell voltage between any two operating points, "1" and "2", in which the only difference between them is their cell pressure (V)
$\Delta V_{cell,T}$	Empirical correlation that predicts the difference in cell voltage between any two operating points, "1" and "2", in which the only difference between them is their average cell temperature (V)
ΔT_{LMTD}	Heat exchange log-mean temperature difference (°C)
ΔT_{min}	Heat exchanger minimum approach temperature (°C)
E	Internal energy (J)
η_{act}	Activation polarization (V)
η_{CHP}	Gross combined heat and power efficiency (%)
η_{conc}	Concentration polarization (V)
η_e	Gross system electrical efficiency (%)
η_{ohm}	Ohmic polarization (V)
F	Faraday's constant (96485 C·mol^{-1})
$\dot{H}_{anode\ exhaust}$	Enthalpy flow rate of the anode exhaust stream (product of molar flow rate and molar enthalpy) (J·s^{-1})
$\dot{H}_{cathode\ exhaust}$	Enthalpy flow rate of the cathode exhaust stream (product of molar flow rate and molar enthalpy) (J·s^{-1})
$\dot{H}_{cathode\ feed}$	Enthalpy flow rate of the cathode feed stream (product of molar flow rate and molar enthalpy) (J·s^{-1})
$\dot{H}_{reformer\ feed}$	Enthalpy flow rate of the reformer feed stream (product of molar flow rate and molar enthalpy) (J·s^{-1})
$\dot{H}_{system\ exhaust}$	Enthalpy flow rate of the system exhaust stream (product of molar flow rate and molar enthalpy) (J·s^{-1})
$\dot{H}_{vented\ exhaust}$	Enthalpy flow rate of the vented exhaust stream (product of molar flow rate and molar enthalpy) (J·s^{-1})
i_{cell}	Average cell current density (mA·cm^{-2})
$i_{cell,1}$	Average cell current density for cell operating point "1" (mA·cm^{-2})
$i_{cell,2}$	Average cell current density for cell operating point "2" (mA·cm^{-2})
$K_{eq,COR}$	Equilibrium constant for the carbon monoxide reduction reaction (unitless)
$K_{eq,BD}$	Equilibrium constant for the Boudouard reaction (unitless)
$K_{eq,MD}$	Equilibrium constant for the methane decomposition reaction (unitless)
kW_e	Kilowatt of electricity (kW)
kW_{th}	Kilowatt of thermal power (kW)

λ	Excess air ratio (unitless)
N_{cell}	Total number of cells in a stack (unitless)
n_{biogas/m^3}	Moles of biogas per m^3 of biogas ($mol \cdot m^{-3}$)
n_{decane/m^3}	Moles of decane per m^3 of biogas ($mol \cdot m^{-3}$)
$\dot{n}_{air}$	Air stream molar flow rate ($mol \cdot s^{-1}$)
$\dot{n}_{biogas}$	Molar flow rate of biogas ($mol \cdot s^{-1}$)
$\dot{n}_{CH4,biogas}$	Molar flow rate of CH_4 in the biogas ($mol \cdot s^{-1}$)
$\dot{n}_{O2,elec}$	Molar consumption rate of O_2 in the stack by electrochemical reaction ($mol \cdot s^{-1}$)
$\dot{n}_{water}$	Water stream molar flow rate ($mol \cdot s^{-1}$)
$(\dot{n}_{H2} + \dot{n}_{CO})_{elec}$	Molar consumption rate of H_2 equivalents (H_2) in the stack by electrochemical reaction ($mol \cdot s^{-1}$)
$(\dot{n}_{H2} + \dot{n}_{CO})_{fuel}$	Molar flow rate of H_2 equivalents (both H_2 and CO) fed to the stack ($mol \cdot s^{-1}$)
MW_e	Megawatt of electricity (MW)
P_e	Gross electrical power output (DC) (W)
P_{th}	Thermal power output (W)
p_{cell}	Cell pressure (bar)
$p_{cell,1}$	Cell pressure for cell operating point "1" (bar)
$p_{cell,2}$	Cell pressure for cell operating point "2" (bar)
p_{CH4}	Partial pressure of methane (bar)
p_{CO}	Partial pressure of carbon monoxide (bar)
p_{CO2}	Partial pressure of carbon dioxide (bar)
p_{H2}	Partial pressure of hydrogen (bar)
p_{H2O}	Partial pressure of water (bar)
p_{O2}	Partial pressure of oxygen (bar)
$\bar{p}_{H2}$	Arithmetic average of the inlet and outlet hydrogen partial pressures in the anode (bar)
$\bar{p}_{H2,1}$	Arithmetic average of the inlet and outlet hydrogen partial pressures in the anode for "operating point 1" (bar)
$\bar{p}_{H2,2}$	Arithmetic average of the inlet and outlet hydrogen partial pressures in the anode for "operating point 2" (bar)
$\bar{p}_{H2O}$	Arithmetic average of the inlet and outlet water vapour partial pressures in the anode (bar)
$\bar{p}_{H2O,1}$	Arithmetic average of the inlet and outlet water vapour partial pressures in the anode for "operating point 1" (bar)
$\bar{p}_{H2O,2}$	Arithmetic average of the inlet and outlet water vapour partial pressures in the anode for "operating point 2" (bar)
$\bar{p}_{O2}$	Arithmetic average of the inlet and outlet oxygen partial pressures in the cathode (bar)

$\bar{p}_{O2,1}$	Arithmetic average of the inlet and outlet oxygen partial pressures in the cathode for "operating point 1" (bar)
$\bar{p}_{O2,2}$	Arithmetic average of the inlet and outlet oxygen partial pressures in the cathode for "operating point 2" (bar)
Q_{BD}	Reaction quotient for the Boudouard reaction (unitless)
Q_{COR}	Reaction quotient for the carbon monoxide reduction reaction (unitless)
Q_{MD}	Reaction quotient for the methane decomposition reaction (unitless)
$\dot{Q}$	Rate of heat transfer ($J \cdot s^{-1}$)
$\dot{Q}_{loss}$	Heat loss through the hotbox shell boundary (W)
R	Ideal gas constant (8.314 $J \cdot mol^{-1} \cdot K^{-1}$)
R_{ASR}	Area specific resistance ($V \cdot cm^2 \cdot mA^{-1}$)
$r_{decane/biogas}$	Moles of decane per mole of Ravensview biogas (mol decane·mol $biogas^{-1}$)
$r_{H2O/C}$	Steam-to-carbon ratio (unitless)
$r_{O2/C}$	Oxygen-to-carbon ratio (unitless)
T_{burner}	Afterburner temperature (K/°C)
T_c	Any temperature on the cold side of a heat exchanger (K/°C)
$T_{cathode\ feed}$	Temperature of the cathode feed stream (K/°C)
T_{cell}	Average cell temperature (K/°C)
$T_{cell,1}$	Average cell temperature of cell operating point "1" (K/°C)
$T_{cell,2}$	Average cell temperature of cell operating point "2" (K/°C)
T_h	Any temperature on the hot side of a heat exchanger (K/°C)
$T_{reformer}$	Reformer temperature (K/°C)
$T_{reformer\ feed}$	Temperature of the reformer feed stream (K/°C)
$T_{system\ exhaust}$	Temperature of the pilot plant exhaust stream (°C)
t	Time (s)
U	Overall heat transfer coefficient ($W \cdot m^2 \cdot °C^{-1}$)
u_f	Fuel utilization (%)
$u_f^{'}$	Surrogate fuel utilization value calculated during the iteration of biogas feed rate (%)
u_{ox}	Oxidant utilization (%)
V_{cell}	Cell voltage (V)
$V_{cell,1}$	Cell voltage of cell operating point "1" (V)
$V_{cell,2}$	Cell voltage of cell operating point "2" (V)

$V_{cell,Nernst}$	Maximum cell voltage as calculated by the Nernst equation (V)
V_{OCV}	Open circuit voltage (V)
W_e	Watts of electricity (W)
W_{th}	Watts of thermal power output (W)

1. INTRODUCTION

Anaerobic digestion (AD) is a biochemical process that consumes organic matter and produces an overhead by-product called biogas. AD is often used at agricultural sites, landfills, and wastewater treatment plants (WWTPs) because it reduces both the volume and pathogen content of the biomass that must be dealt with at these sites [1]. The composition of the biogas varies according to digestion conditions and feedstock composition [2], but typically contains about 60 vol. % CH_4, 40 vol. % CO_2, and a variety of other trace compounds. Table 1.1 outlines the general composition of biogas produced by WWTP digesters:

Table 1.1. Approximate composition of WWTP biogas. The data taken from Wheeldon *et al*. (2007) [3] is specific to the province of Ontario. (*) indicates that the wet/dry basis is not provided. "n.d." indicates that the species is below the detection limit. The TVOC value includes all non-methane organic compounds.

Constituent	Representative Value	Range	Reference
CH_4 (%) (dry basis)	60.8	58 - 70	[3]
CO_2 (%) (dry basis)	34.8	30 - 43	[3]
H_2S (ppmv) (dry basis)	78	2.5 - 3450	[3]
O_2 (vol. %) (dry basis)	1.5	0.1 - 2	[3]
N_2 (vol. %) (dry basis)	2.4	1.2 - 7.1	[3]
H_2O (vol. %)	6	5.9 - 15.3	[1]
Siloxanes (ppmv) (wet basis)	0.8	0.2 - 10	[1]
Halogens (ppmv)*	1.4	n.d. - 2.6	[4]
Organic Sulphur (ppmv)*	0.8	0.1 - 1.6	[4]
TVOCs ($mg \cdot m^{-3}$)*	not provided	13 - 268	[5]

The TVOC (Total Volatile Organic Compound) designation includes all non-methane volatile organic compounds (NMVOCs) found in the biogas: siloxanes, halogens, COS, CS_2, mercaptans, and various other aromatic and aliphatic hydrocarbons. Relative to WWTP biogas, landfill biogas generally contains lower CH_4 [6] and has higher loadings of halogenated species [7]; agricultural biogas typically has lower loadings of siloxane species [5, 7].

The classic treatment of the biogas by-product has been to flare it to mitigate the CH_4 emission [1]. However, given its relatively high energy content (approx. 24 $MJ \cdot m^{-3}$ HHV [3]) and biogenic origin, biogas is now broadly recognized as a renewable source of energy. It is now quite common for larger WWTPs to recover the biogas energy using boilers or combined heat and power (CHP) technologies such as reciprocating engines and microturbines. Well-designed biogas utilization systems can reduce both the environmental footprint and operating cost of the facility by offsetting the amount fuel or electricity imported to the site [8].

As a CHP technology, solid oxide fuel cell (SOFC) systems appear to be uniquely suited for biogas applications. Similar to other CHP technologies, SOFC systems can provide a mix of both electrical and thermal power when supplied with biogas. However, studies have demonstrated biogas-fed SOFC systems to have superior electrical efficiencies [9, 10, 11], and this would likely be desirable at many sites. For example, Farhad *et al*. (2010) [9] showed that biogas-fed SOFC systems are much more likely to generate a surplus of electricity at WWTPs compared to reciprocating engine technology, and such surpluses could be sold by the plant for a profit. In addition, SOFC systems have reduced sound and particulate emissions [12]. In fact, fuel cell systems have been referred to as the CHP systems with the cleanest exhaust emissions [1].

Despite the promise of biogas-fed SOFC systems, SOFC technology has remained largely in the demonstration phase, which has precluded their installation at WWTPs [1, 11]. To the author's knowledge, there are no SOFC systems that have been directly connected to a digester in long term operation; although, a handful of insightful demonstrations have been carried out [13, 14, 15, 16, 17, 18, 19]. Regardless, since 2010 there has been mounting evidence that SOFC technology is reaching commercial status [20, 21, 22]. Therefore, the study of SOFC systems within the context of biogas application warrants ongoing investigation.

1.1. Problem Statement

Currently, only a small fraction of WWTPs have on-site biogas utilization systems; the ones that do tend to be larger in size as smaller facilities are deterred by the associated capital and maintenance costs [23, 24]. Using the United States as an example, only about 19 % of WWTPs that use AD and treat greater than 5 MGD of wastewater utilize their biogas (this includes both CHP technologies and boilers) [23].

Requirements for biogas purification contribute to the cost of integrating power generators with the AD process. Many species listed in table 1.1 cause the degradation of materials and equipment if their loadings are not significantly reduced. Given their abundance and destructive power, the two most concerning species are H_2S and siloxane [1]. In addition, due to the catalytic materials used, fuel cell systems are particularly sensitive to many of the VOC species; particularly the halogens, organic sulphur species, unsaturated hydrocarbons, and aromatics [14, 25, 26, 27, 28].

H_2S is highly corrosive [7, 29] and will poison catalytic materials used for any downstream fuel processing [4, 26] of the biogas. For humid biogas, adsorption using iron sponge material is an established and inexpensive means of H_2S abatement [1, 29]. Alternatively, for dehumidified biogas, adsorption using alkali-impregnated activated carbon (AC) is an established and inexpensive [3] means for H_2S removal, but only if the biogas has an H_2S loading less than 200 ppmv and an O_2 loading between 0.3 and 0.5 vol. % [3, 4]. Wheeldon *et al*. (2007) [3] conducted a survey on biogas production at WWTPs in the province of Ontario and found that the majority of biogases contain less than 200 ppmv H_2S, suggesting that alkali-impregnated AC would be applicable at the majority of sites. Both iron sponge and AC adsorbents will reduce the TVOC content by various amounts, but subsequent downstream VOC polishing is generally required, especially for the siloxanes [1, 30]. Other technologies for H_2S abatement exist, but these often bring an additional level of expense and/or complexity to the system [29].

Siloxanes are polymers with backbone chains made of alternating silicon and oxygen atoms and can have linear or cyclic conformations; hydrocarbon groups are attached to the remaining bond sites of the silicon atoms and are typically methyl groups. Siloxanes are manufactured for use in many household and industrial products such as shampoos and detergents; they enter WWTPs through household and industrial runoff and appear in the biogas because their volatility is enhanced in the digester (*i.e.*, digesters are typically operated at elevated temperatures above ambient conditions, between 35 and 40°C) [2, 29]. Siloxanes of low molecular weight tend to be more volatile than those of higher molecular weight [6]. Unfortunately, at elevated temperatures typical of combustion, siloxanes decompose to form amorphous silica (SiO_2) deposits that coat the inner surfaces of process equipment. These coatings lead to accelerated mechanical abrasion, flow restrictions, and reductions in heat transfer rates [6, 29, 30, 31]. Urban *et al*. (2009) [30] provide an illustration of a cylinder head that was completely coated after about 3500 h of operation:

Figure 1.1.1. Cylinder head coated by amorphous silica deposits after 3500 hours of operation. Reproduced from Urban *et al*. (2009) [30].

In general, both iron sponge and ACs are not very selective toward siloxanes [1, 30]. In fact, low molecular weight siloxanes are known to be displaced from the AC surface by higher molecular weight siloxanes and other VOCs present in the biogas [6]. This is unsettling given that the loading and composition of siloxanes and VOCs in the biogas is variable in nature. Rasi *et al*. (2011) [7] claim that, on a weekly basis, siloxane loadings can vary by up to a factor of 3 at some WWTPs. In spite of this, AC is currently the most common technology used for siloxane removal from WWTP biogas [1, 6], which suggests that higher-than-desirable amounts of adsorbent are being used. Similar to the case of H_2S abatement, alternative technologies exist for siloxane removal, but most of these are currently more complex than simple physical adsorption and can be highly energy- and process-intensive [6, 29, 30].

1.2. Scope of this Work

Recently, two works [30, 31] have demonstrated activated alumina as a highly selective adsorbent material for siloxanes. Activated alumina is commonly used as a desiccant material, is widely-available, and is considered to be quite

inexpensive. Finocchio *et al*. (2008) [31] showed that at temperatures between 250 and 400°C hexamethylcyclotrisiloxane (abbreviated as "D3") chemically and irreversibly decomposes onto the surface of activated alumina from a model biogas mixture. Importantly, a 100 % removal efficiency was reported along with the claim that siloxane decomposition had not taken place on the surfaces within the peripheral reactor system. Additional insights were provided by Urban *et al*. [30] who showed that, in addition to siloxanes, the loadings of a wide range of deleterious VOCs can be reduced using a heated activated alumina bed.

In short, the works of Finocchio *et al*. [31] and Urban *et al.* [30] suggest that a hot activated alumina stage preceded by either an alkali-impregnated AC stage or iron sponge stage could serve as the basis for an inexpensive and simple biogas purification system.

A 2 kW_e (nominal) pilot-scale CHP system has been proposed for construction at the Ravensview WWTP in Kingston, ON. The pilot plant will demonstrate the direct integration of SOFC technology and the AD process, and is proposed to include the novel purification sequence of adsorbents elucidated above: an initial alkali-impregnated AC stage for H_2S adsorption followed by a hot activated alumina stage for the selective chemical adsorption of siloxane species. The pilot plant is proposed to serve as a highly electrically efficient and environmentally-friendly alternative to the incumbent CHP technologies, and will promote the uptake of biogas utilization at smaller WWTPs.

The purpose of this work is to provide an initial performance assessment of the proposed pilot plant operating under various design conditions. To this end, a preliminary process model (steady-state) of the system was developed using the UniSim Design™ R400 process modeling software. The process model has been configured to the most recent proposal for the plant layout, but can accommodate future design updates and/or changes. The model is further enhanced to include an empirical cell model that was developed to be tunable to the performance of prospective SOFCs through regression.

Building on the latter point, this thesis work also involved an experimental performance study in which a pilot-scale SOFC stack provided by TOTO Ltd.[1] was operated on biogas reformate (processed biogas). The TOTO stack was considered to be the first prospective stack for the plant and its performance was incorporated into the process simulation via the empirical cell model (*i.e.*, the cell model was regressed to the data gathered from the performance study).

[1]Tōyō Tōki Limited. TOTO Ltd. is a Japan-based toilet manufacturer. As part of its business model, the company leverages its expertise in ceramic products to develop SOFCs and SOFC power systems [32].

Prior to the results and discussion of section 4, the experimental performance study, cell model regression, and process model are discussed in section 3. Section 3 ends with the presentation of the system performance according to a set of reference design conditions.

In section 4.1, the cell model is revisited and regressed to a surrogate data set found in the literature in order to demonstrate its general applicability. The remainder of section 4 is dedicated to demonstrating the process model as a valuable design tool. Specifically, a series of sensitivity analyses are carried out in which the process model is used to predict the dependence of pilot plant performance on key design variables. The sensitivity analyses were all carried out relative to the predefined reference conditions of section 3 and were bound by a set of practical design constraints. In addition, because the system was originally scaled to produce 2 kW_e gross electrical power output, the current density – which heavily influences the electrical power output – was held constant at 75 $mA \cdot cm^{-2}$.

There were many possible sensitivity analyses that could have been carried out, but the studies were narrowed to focus on the effects of variations in the system feed streams. Therefore, the biogas composition (section 4.2.1), water feed rate (section 4.2.2), air feed rate (section 4.2.3), and biogas feed rate (section 4.2.4) were chosen as the independent variables. The process model has been developed to control the water, air, and biogas feed rates through the steam-to-carbon ratio, oxidant utilization, and fuel utilization, respectively. Lastly, in section 4.2.5, the effect of steam-to-carbon ratio, oxidant utilization, and fuel utilization are simultaneously considered and conditions for maximum possible performance are discussed for the pilot plant operating on Ravensview biogas.

As a final note, this work focused on macro system performance. Therefore, the biogas contaminant species were neglected because the adsorption reactions have little impact on the material and energy balances of the system. By extension, it was assumed that the adsorbents remove 100 % of the contaminants and, as a result, there is no fuel cell degradation.

2. LITERATURE REVIEW

The objective of this section is to establish the current status and understanding of integrated AD-SOFC systems. A bulk of the relevant information is provided in reports of various demonstrations and modeling studies.

Focus will be limited to systems as a whole. Studies of individual plant components, including the individual cells, are numerous and are considered outside the scope of this review. Section 2.1 will serve as a general introduction to SOFC systems. Modeling studies involving biogas-fed SOFC systems are covered in section 2.2 and a review of the reported system demonstrations are covered in section 2.3.

2.1. SOFC System Basics

Figure 2.1.1 outlines the basic structure and function of a single SOFC.

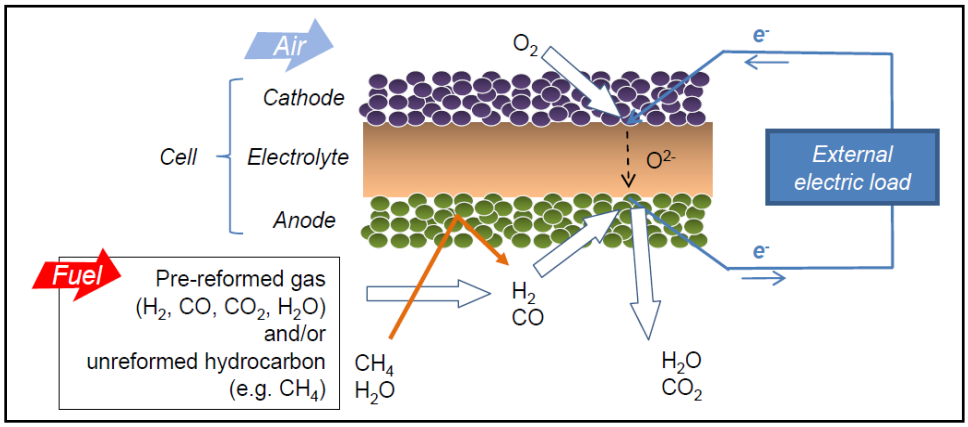

Figure 2.1.1. A generic SOFC operating under closed-circuit conditions. Reproduced from Shiratori *et al*. (2011) [33].

As shown, O_2-rich and H_2-rich streams flow along opposite sides of a multi-layered barrier. The barrier is comprised of a non-porous ceramic electrolyte

bonded between two porous and catalytically-active electrode layers. These electrode layers are the anode and the cathode. Typically, the anode, cathode and electrolyte are made of Ni-impregnated ZrO_2 cermet, Sr-doped $LaMnO_3$, and Y_2O_3-doped ZrO_2, respectively [25].

On the cathode side, molecular oxygen permeates the porous layer from the bulk stream and is reduced according to the following electrochemical reaction:

$$½O_2\,(g) + 2e^- \rightarrow O^{2-} \qquad (2.1.1)$$

At typical SOFC operating temperatures (between 600 and 1000°C), the solid electrolyte becomes an O^{2-} ion conductor allowing the ions to diffuse down the concentration gradient to the anode side. Within the anode are catalytically-active sites that facilitate the electrochemical reaction between the O^{2-} ions emerging from the electrolyte and H_2 and/or CO molecules diffusing in from the bulk fuel stream:

$$O^{2-} + H_2\,(g) \rightarrow H_2O\,(g) + 2e- \qquad (2.1.2)$$

$$O^{2-} + CO\,(g) \rightarrow CO_2\,(g) + 2e- \qquad (2.1.3)$$

The electrons at the anode have a higher potential energy than those at the cathode; therefore, when a closed-circuit is provided between the anode and cathode, the resulting flow of electrons can provide useful electrical work. The power output of a single cell is low (tens of watts) so, typically, in full-scale systems, many cells are electrically-linked to form a "stack".

In general, there are two SOFC structures: planar (PSOFC) and tubular (TSOFC). PSOFCs are represented well by figure 2.1.1 in that they are sheet-like structures. By contrast, TSOFCs are essentially PSOFCs that have been fabricated into hollow tubes, with the fuel flowing outside and the oxidant flowing inside (or vise versa).

There is a tradeoff between the cell types. TSOFCs are more resilient to thermal stress because less sealing is required between the cells in the stack. PSOFC stacks require more sealing, but the cells can be packed closer together yielding smaller stacks with greater power density [25].

The following overall cell reactions can be derived from reactions 2.1.1, 2.1.2, and 2.1.3:

$$½O_2\ (g) + H_2\ (g) \rightarrow H_2O\ (g) \quad (2.1.4)$$

$$½O_2\ (g) + CO\ (g) \rightarrow CO_2\ (g) \quad (2.1.5)$$

Reactions 2.1.4 and 2.1.5 are just the combustion of H_2 and CO, respectively. A portion of the heat liberated by these reactions is used to maintain the temperature of the stack (the stack is housed within an insulated hotbox). In short, it can be said that an SOFC is a device capable of extracting electrical power from the managed combustion of H_2 and CO. As a side note, additional reactions are possible in the anode and this will be addressed later in this sub-section.

The maximum possible cell voltage (between the electrodes) is realized when there are no irreversibilities occurring within the cell. This happens when the feed streams are flowing, but the external circuit is left open (no current flow). The voltage at these conditions is referred to as the open-circuit voltage (V_{OCV}) and the Nernst Equation is commonly used to calculate its value. For a cell operating on a feed mixture containing only H_2 as the combustible species the Nernst equation is:

$$V_{cell,Nernst} = \frac{\left(-\Delta G^{o}_{R,T_{cell}}\right)}{2F} + \frac{RT_{cell}}{2F}\ln\left(\frac{p_{H2}p_{O2}^{0.5}}{p_{H2O}}\right) \quad (2.1.6)$$

In equation 2.1.6, $\Delta G^{0}_{R,Tcell}$ is the standard Gibbs reaction energy for H_2 combustion (equation 2.1.4) calculated at the cell operating temperature, R is the ideal gas constant, and F is Faraday's constant. p_{H2} and p_{H2O} are the partial pressures of H_2 and H_2O in the bulk anode stream and p_{O2} is the partial pressure of O_2 in the bulk cathode stream. The appearance of partial pressures indicates the dependence of cell voltage on species concentration.

In practice, electrical power is never provided at the V_{OCV}. Figure 2.1.2 shows the experimental performance of a two-celled TSOFC stack (two cells

connected in series)[2]. The curves in the figure are commonly referred to as "polarization curves".

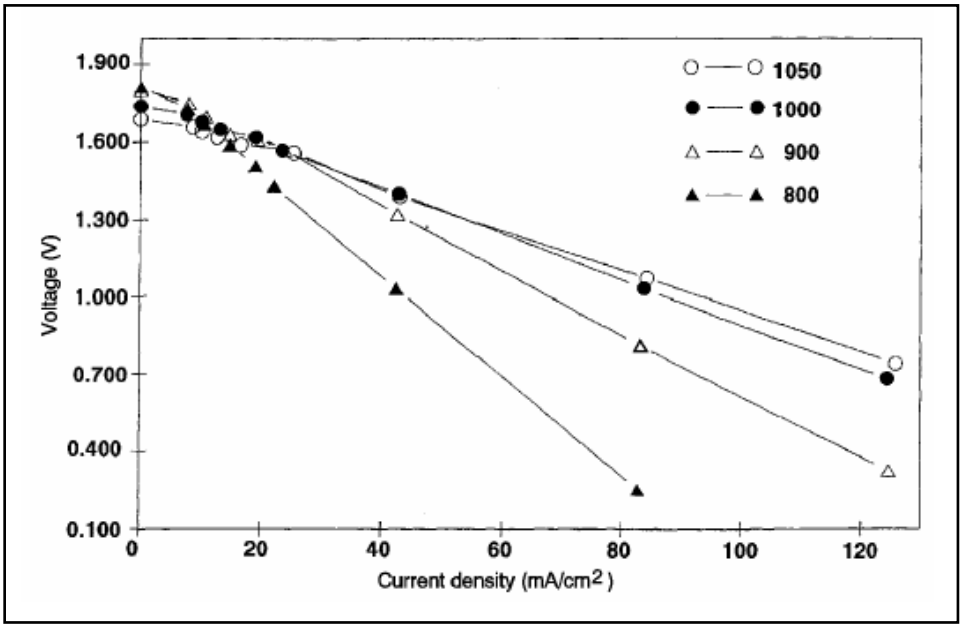

Figure 2.1.2. Example performance of a TSOFC stack containing two cells electrically connected in series as presented by EG&G Technical Services, Inc. (2004) [25]. The cathode feed is air. The anode feed mixture is composed of H_2 (67 %), CO (22 %), and H_2O (11 %).

In figure 2.1.2, the voltage is reported as a function of current density, which is just the single cell current divided by the active surface area of the cell. At zero current density, the cell voltage (divide the stack voltage in figure 2.1.2 by 2) equals the V_{OCV} (assuming there's no current leakage through the electrolyte). Shown in figure 2.1.2 is that the V_{OCV} decreases with a rise in temperature.

As shown in figure 2.1.2, individual polarization curves are approximately linear with respect to current density. This is because the voltage drop through the cell materials is approximately proportional to the cell current according to Ohm's Law. This particular type of voltage drop, which is dependent on the cell resistance, is referred to as "ohmic polarization" or "ohmic overpotential" (η_{ohm}). The other two commonly-cited polarizations (phenomenon

[2] For single cell voltage, divide the y-axis voltage by 2.

resulting in cell voltage drop) are the activation polarization (η_{act}), which is derived from the irreversibilties associated with the electrochemical reactions, and the concentration polarization (η_{conc}), which is derived from the irreversibilities associated with diffusion and concentration gradients. During typical SOFC operation, these latter polarizations are far less significant than the ohmic polarization [33].

A noteworthy trend is that the magnitude of the slopes of the polarization curves increase as temperature is reduced. This is because the cell materials are more resistive (less conductive) at the lower temperatures [25]. Contrastingly, the V_{OCV} increases as temperature is reduced. These opposing behaviors may cause the polarization curves of different temperatures to cross at low current density values (occurs in figure 2.1.2 at approx. 10 $mA \cdot cm^{-2}$).

Most SOFC systems contain a catalytic reformer for the fuel processing (conversion) of hydrocarbons into H_2-rich fuel for the cell. Reforming is typically carried out above 800°C, conditions which thermodynamically favour high CH_4 conversion. The various possible reforming reactions are listed below:

$CH_4\ (g) + H_2O\ (g) \leftrightarrow 3H_2\ (g) + CO\ (g)$	(SR)	(2.1.7)
$CH_4\ (g) + CO_2\ (g) \leftrightarrow 2H_2\ (g) + 2CO\ (g)$	(DR)	(2.1.8)
$CH_4\ (g) + ½O_2\ (g) \rightarrow 2H_2\ (g) + CO\ (g)$	(POX)	(2.1.9)
$2CO\ (g) \leftrightarrow CO_2\ (g) + C\ (s)$	(BD)	(2.1.10)
$CH_4\ (g) \leftrightarrow 2H_2\ (g) + C\ (s)$	(MD)	(2.1.11)
$CO\ (g) + H_2\ (g) \leftrightarrow H_2O\ (g) + C\ (s)$	(COR)	(2.1.12)
$CO\ (g) + H_2O\ (g) \leftrightarrow H_2\ (g) + CO_2\ (g)$	(WGS)	(2.1.13)

The top three (2.1.7 to 2.1.9) are the primary reforming reactions: steam reforming (SR), dry reforming (DR), and partial oxidation (POX). Each reaction has unique characteristics which influence the final system configuration and performance. For example, SR requires a supply of steam. To provide the steam, one option is to vapourize water that has been externally provided to the system. Another option is to re-direct a portion of the H_2O-rich anode exhaust (see reaction 2.1.4) back to the fuel processor in an anode gas recycle (AGR) loop. An AGR can potentially

eliminate the need for an external H_2O supply but the balance of plant (BOP) components required to circulate the hot gas are not readily available, especially for smaller scale systems [34, 35]. Apart from the practical concerns of steam supply, SR is very endothermic and must be thermally-integrated into the system in order to receive the heat necessary to drive the reactions.

DR requires a supply CO_2 and is also endothermic. POX requires the supply of O_2, but this can be provided in the form of air. A major advantage to the POX reaction is that it is exothermic and, therefore, the requirement for strategic thermal integration within the system is somewhat relaxed. With that said, POX reforming has some major disadvantages. First, relative to the SR and DR reactions, POX produces one less mole of fuel molecule (H_2 and CO) per mole of CH_4 converted. Second, there is a risk of over-oxidation of the fuel and even explosion [36]. Third, the air supplied dilutes the reformate stream with N_2 which serves to lower the voltage of the cells downstream.

Combinations of SR, DR, and POX are possible. For example, SR and POX can be carried out simultaneously by adding both steam and O_2 (air). This operation is referred to as autothermal reforming (ATR) because the POX reaction can provide the thermal duty for SR. In addition, the presence of CO_2 in the biogas means some degree of DR is also possible. Regardless, only SR and POX reforming are commercially relevant at this point [37, 38] with the caveat that some degree of DR may occur (*i.e.*, in the case of biogas reforming).

Reactions 2.1.10 through 2.1.12 are the carbon-forming Boudouard (BD), methane decomposition (MD), and carbon monoxide reduction (COR) reactions. The accumulation of surface carbon reduces catalyst activity by blocking or denaturing the active sites. Carbon accumulation can be mitigated by assuring that a high enough amount of oxidant (H_2O, O_2, or CO_2) is provided in the fuel processor [9, 25, 39]. Although biogas has an inherent CO_2 content capable of carrying out some degree of DR, it's not enough to suppress carbon formation [9]. Therefore, additional steam or air must always be provided. In this work, when biogas is reformed with steam, the process is referred to as dry-SR; similarly, it will be referred to as dry-POX when air is used. This accounts for the possibility of concurrent DR due to the inherent CO_2 content.

There is an enhanced likelihood for carbon formation within the system when higher-hydrocarbons are present in the feedstock. At typical reformer and SOFC temperatures (approximately greater than 600°C), higher-hydrocarbons will thermally crack to form highly-reactive, carbon free radicals that lead to the formation of carbon deposits on surfaces and deactivate catalytic materials. For this reason, it is common for natural gas-fed SOFC systems to contain a catalytic pre-reformer unit. Pre-reformers are generally run in the 350 to 550°C temperature range and convert all higher-hydrocarbons to CH_4 upstream of the main reformer (does not include halogens, siloxanes, or sulphurous species). Like steam reforming, pre-reforming requires the addition of steam. However, unlike steam

reformers, pre-reformers are run adiabatically with the temperature generally dropping along the length of the bed due to the endothermic reactions. Pre-reformer use with natural gas is an established industrial practice [40]. Less established is pre-reformer use in biogas applications. Nevertheless, they have appeared in some biogas-fed demonstration systems [41, 42].

The final reaction (2.1.13) is known as the water-gas shift (WGS) reaction. At high temperatures typical of the fuel processor and stack in SOFC systems, the WGS reaction is fast and often assumed to reach equilibrium by fuel cell researchers [25]. This makes it a highly influential reaction within the context of SOFC systems.

SOFC anode materials are actually catalytically active for the SR, DR, POX, and the WGS reactions [14, 25, 43, 44], making direct internal reforming (DIR) possible within the cells. Although DIR of biogas has been demonstrated [14, 45, 46, 47, 48, 49, 50], it is still generally desirable to carry out some degree of fuel processing external to the cells to protect against carbon deposition [3, 10], excessive thermal gradients [51, 52, 53], and biogas contaminants. An interesting approach is to house the reformer within the hotbox with the stack. This is referred to as indirect internal reforming (IIR) and is most useful when the fuel processing is endothermic; in this case, the reforming duty is provided by the stack.

Many SOFC system configurations can be found throughout the literature, but there are some commonalities. At the heart of all systems is the stack. Excess fuel and oxidant are always provided to the cells so that the partially-depleted streams can be post-combusted to provide a hot tail gas stream. This tail gas stream is fed back through a recuperative heat exchange network, providing sensible heat for, say, steam generation, stream pre-heating, fuel processing, and digester heating (as in the case of fully integrated AD-SOFC systems). The still-remaining sensible heat of this stream can even be used for climate control at the WWTP and/or local district heating. The remaining variability among system configurations is due to the choice of fuel processing technology and stack operating temperature.

2.2. Modeling Studies

The earliest modeling study found in the literature of a biogas-fed PSOFC system was published by Van herle *et al*. [13] in 2003. In their work, Van herle *et al*. [13] developed a steady-state process model in order study the effect of relevant design variables on system performance.

The process included a theoretical reformer capable of carrying out either dry-SR or dry-POX, a 100-celled PSOFC stack, an afterburner, and blowers. The tail gas stream provided the thermal power required for pre-heating and steam generation, but this was assumed only in a macro sense; for example, only the process flow sequence up to the afterburner was defined (*i.e.*, the recuperative heat exchanger network was not defined).

The process was programmed into a customized modeling environment (VALI™ chemical manufacturing software interfaced with MATLAB™). Their major assumptions were that each unit operated isothermally and that chemical equilibrium is achieved in all reactors. It was previously mentioned that only the process sequence up to the afterburner was defined; as a result, the thermal output of the system was calculated from a simple tally of heat sources and sinks and the thermal output was simply the tally surplus [13].

Van herle *et al*. [13] began their performance analysis by defining a reference design case which relied solely on dry-POX reforming. The conditions of the reference case are listed in table 2.3.1.

Table 2.3.1. Reference conditions for the Van herle *et al*. (2003) [13] simulations.

Operating Variable	Value(s)
Biogas composition (vol. %)	60 CH_4, 40 CO_2
Biogas feed rate, $\dot{n}_{biogas}$ ($Nm^3 \cdot h^{-1}$)	1.5
Steam-to-carbon ratio, $r_{H2O/C}$	0.35
Oxygen-to-carbon ratio, $r_{O2/C}$	0
Excess air ratio, λ	3
Reformer temperature, $T_{reformer}$ (°C)	800
Number of cells, N_{cell}	100
Active cell area, A_{cell} (cm^2)	100
Average cell temperature, T_{cell} (°C)	800
Fuel utilization, u_f (%)	80
Average cell current density, i_{cell} ($mA \cdot cm^2$)	568
System pressure (bar)	1.05

At reference conditions, the system provided 3.1 kW_e and 5.16 kW_{th} with net electrical and CHP efficiencies of 33.8 % and 91.4 % (LHV basis), respectively [13].

The remainder of their work consisted of a series of sensitivity analyses carried out relative to the reference conditions. In general, a single design variable was swept while the others were held at their reference case values. However, usually an additional second operating variable was "selected-out" to serve as a calculated degree of freedom [13]. An example of this would be selecting-out the fuel utilization to serve as a floating value as stack current is adjusted.

A sweep of biogas composition was carried out which was based on compositional data collected at the Maison Blanche farm site in Lully, Switzerland. Composition data from the site showed that the CO_2 content varied between 25 and 50 vol. %. In light of this, Van herle *et al*. [13] swept the biogas CO_2 content from 20 to 65 %; the balance included CH_4 only. Throughout the sweep, fuel utilization was constrained to 80 % by floating the stack current. Inspection of the results revealed a 6 % increase in net electrical efficiency (from 30 to 36 %) over the sweep range. The authors noted that this was a counter-intuitive result. One would expect the efficiency to drop since the CH_4 content is diluted in the stack. The key realization was that the calculated current density was declining in order to meet the 80 % fuel utilization constraint. As a result, there was a substantial reduction in ohmic overpotential which led to the aforementioned rise in electrical efficiency. In a grander sense, these results demonstrated a major strength of SOFC systems: at biogas compositions too lean for reciprocating engines (less than 50 % CH_4), the electrical efficiency of a SOFC system could be expected to increase [13]. The authors did not report how the electrical power output was influenced.

The oxygen-to-carbon ratio for POX reforming was swept from 0.3 to 0.6. Throughout the sweep, the stack current was held constant (50 A) and the fuel utilization was allowed to float. Overall, this resulted in a modest net electrical efficiency decline of 2 % which was largely attributed to an increase in CH_4 conversion via the POX reaction. The POX reaction goes to completion, but produces one less H_2-equivalent (H_2 and CO) per mole of CH_4 converted than the other possible reforming reactions (SR and DR). As a result, as the extent of POX reforming increased, the partial pressure of fuel molecules downstream in the cells was reduced. Not mentioned by the authors was the effect of increasing N_2 dilution that would have accompanied the rising air feed rate. Regardless, both effects promote a lowering of the cell voltage and decline in stack power output. In the same analysis, the CHP efficiency was found to increase by about 2 percentage points. This was largely attributed to the exothermic quality of the POX reaction and its downstream effect on the tail gas stream [13].

Two sensitivity analyses were carried out with respect to H_2O addition. In the first case, H_2O was fed to the system with the reference case biogas and air feed rates (autothermal reforming). In the second case, only H_2O was fed to the system (dry-SR). In both cases, the steam-to-carbon ratio was swept from about 0.1 to 2 while the fuel utilization (80 %) and stack current were held constant.

Results showed that adding H_2O to the system always decreased the system performance (power output and efficiencies). Specifically, the additional H_2O diluted the fuel line and lowered the V_{OCV}, which caused a corresponding decline in net electrical power output and efficiency. Furthermore, the additional requirement for steam generation diminished the thermal surplus of the system. From these findings, it can be said that only a minimum amount of H_2O should be added to SOFC systems because all performance metrics are lowered when the amount added is increased [13].

Under conditions of constant fuel utilization (80 %), the stack temperature was swept from 750 to 1000°C. This essentially doubled the net electrical efficiency and net electrical power output (from 25 to 49 % and 2.2 to 4.4 kW_e, respectively). This rise in performance was due to an increase in cell conductivity. However, the trend of rising performance was largely diminished by the time 1000°C was reached; at 1000°C the increase in cell conductivity was balanced by the decline in V_{OCV} [13].

In a subsequent publication, Van herle *et al*. (2004) [39] scaled-up the model used in Van herle *et al*. [13] to study the system's performance operating on-site of a WWTP. In addition to scaling-up the model, the cell model was updated to account for concentration polarization.

Similar to their previous work ([13]), Van herle *et al*. [39] began their analysis by defining a reference design case which is listed in table 2.3.2. Contrary to their previous work ([13]), this reference case relied solely on dry-SR fuel processing.

At reference conditions, the system produced 131 kW_e and 107 kW_{th} at 48.7 % and 88.2 % net electrical and CHP efficiencies (HHV basis), respectively. Van here *et al*. [39] compared this performance with that of the reciprocating engine that was currently installed on-site of the WWTP. It was determined that the SOFC system would provide a more appropriate energy balance for the site because it provided a greater proportion of electrical power as its total power output. The engine achieves an average net electrical efficiency of only 21 % (HHV basis) and satisfies only about 52 % of the site's electrical demand. In addition, it produces an overabundance of heat which reportedly has to be rejected to the environment [39].

Similar to their previous work, a series of sensitivity analyses were carried out with respect to the reference design case. An excess air ratio (cathode air) sweep was conducted from a value of 1 to 5. Results showed that the reformer duty, heat generated by the stack, and heating duty for pre-heating the cathode feed air (from 600 to 800°C) were perfectly balanced at an excess air ratio of 3. The implication is that an excess air ratio of 3 will lead to an approximate thermal balance for a hotbox operating at 800°C containing both a stack and biogas steam reformer [39].

Table 2.3.2. Reference conditions for Van herle *et al.* (2004) [39] simulations.

Operating Variable	Value(s)
Biogas composition	63 CH_4, 35 CO_2, 1.5 H_2O, 0.5 N_2
Biogas feed rate, $\dot{n}_{biogas}$ ($Nm^3 \cdot h^{-1}$)	43
Oxygen-to-carbon ratio, $r_{O2/C}$	0
Steam-to-carbon ratio, $r_{H2O/C}$	0.5
Excess air ratio, λ	3
Reformer temperature, $T_{reformer}$ (°C)	800
Number of cells, N_{cell}	2400
Active cell area, A_{cell} (cm^2)	361
Average cell temperature, T_{cell} (°C)	800
Fuel utilization, u_f (%)	80
Average cell current density, i_{cell} ($mA \cdot cm^2$)	239
System pressure (bar)	1.1

The effect of biogas composition was studied. CO_2 content was swept from 30 to 50 %. The current density was floated in order to maintain 80 % fuel utilization. A modest increase in net electrical efficiency was observed (from 48 % to 51 %) resulting from a decrease in current density and, hence, ohmic losses. However, the decrease in current density also caused a decline in net electrical power output (from 140 to 104 kW_e). Regardless, the results suggest that SOFC systems are capable of providing a significant electrical power output at competitive efficiency when biogas is too lean for a reciprocating engine (*i.e.*, below 50 % CH_4) [39].

Van herle *et al*. [39] studied the impact of sweeping the steam-to-carbon ratio. The performance trend was similar to that of Van herle *et al*. [13] in that increasing the amount of H_2O fed to the system always reduced system performance. However, the authors remarked that the decline in electrical performance was minimal in this case. For example, when the steam-to-carbon ratio was doubled from 0.5 to 1.0 the reduction in net electrical power output and efficiency dropped by only 4 kW_e and 1.7 percentage points, respectively, relative to the reference condition. In any event, doubling the steam-to-carbon ratio still yielded a competitive performance to reciprocating engines [39].

Toward the end of their work, Van herle *et al*. [39] used the model to compare the performance of different modes of operation. Four of these modes are of interest here and included a CH_4-feeding case whereby steam reforming was used ("steam-reformed CH_4"), a biogas-feeding case whereby dry-SR was used

("steam-reformed biogas"), a biogas-feeding case whereby dry-POX was used ("biogas POX"), and a pure H_2-feeding mode ("H_2"). In all cases, the fuel feed rates were normalized to provide an enthalpy flow of 269.3 kW (product of flow rate and HHV). Interestingly, it was found that the steam reforming of biogas (dry-SR) is more endothermic than the steam reforming of pure CH_4. Therefore, the steam-reformed biogas case provided a greater sink for the stack heat than the steam-reformed CH_4 case, and less air was required for stack cooling (*i.e*., maintaining the hotbox temperature at 800°C). In the "biogas POX" and "H_2" cases the endothermic heat sink was diminished relative to the steam reforming cases, which increased the air cooling and blower power demand. Overall, the two highest net electrical efficiencies were provided by the "steam-reformed CH_4" (49.2 %) and "steam-reformed biogas" (48.7 %) cases (HHV basis). The two lowest net electrical efficiencies were provided by the "H_2" (42.5 %) and "biogas POX" cases (42.9 %) (HHV basis). Although these performances strongly correlated with the air cooling requirement, additional factors noted by the authors contributed to the various system performances [39].

Yi *et al*. (2005) [54] developed a steady-state process model of a pre-commercial 576-cell Siemens Westinghouse TSOFC system in order to compare its performance on four different fuel feeds.

The process included a fuel compressor, an external recuperative reformer co-fed by an AGR (dry-SR), a 576-cell TSOFC stack, afterburner, two air recuperators, an air feed blower, and a natural gas compressor [54]. Contrary to the Van herle *et al*. [13] and Van herle *et al*. [39] systems, the tail gas sequence through a recuperative heat exchange network was defined, making this a more comprehensive process model [39].

The process model was developed using the Advanced Power Systems Analysis Tools (APSAT^{TM}) modeling software developed at the University of California, Irvine. Reportedly, the software included a library of chemical process sub-component models and a capability for linking them into larger process models. Yi *et al*. [54] indicated that the model was quite comprehensive, accounting for complex heat transfer phenomenon occurring within the stack and through its insulation. Unlike the cases of Van herle *et al*. [13] and Van herle *et al*. [39], the tail gas flow sequence through the recuperative heat exchangers was defined and the calculation of thermal power output was more comprehensive than a simple tally of heat sources and sinks. The cell model is believed to have been programmed according to the performance of Siemens-Westinghouse TSOFCs, but details were not provided. Chemical reactions were likely modeled to reach equilibrium, but this was not explicitly stated [54].

Yi *et al*. [54] compared the system performance on four different fuel feeds: pipeline natural gas (96% CH_4), pre-reformed diesel (50% CH_4, 30% H_2, 20% CO_2), biogas (60% CH_4, 40% CO_2), and coal-derived syngas (0% CH_4, 36%

H_2, 18% CO_2, 46% CO). Only a single performance point was calculated for each case. A handful of operating variables were set equal for all cases (stack temperature, current density, overall fuel utilization, and air feed flow rate) and the optimal system efficiency was solved relative to two adjusted variables: the AGR ratio and the by-pass flow rate of feed air around the low-temperature recuperator.

The optimal electrical efficiencies for the natural gas, pre-reformed diesel and biogas cases were similar in magnitude (approximately 36 % net electrical efficiency, LHV basis). The stack power outputs for these three cases were also quite similar (approximately 21 kW_e DC). These results suggest that biogas is an all-around competitive fuel for SOFC systems. The coal-derived syngas case, however, yielded a drastically lower performance (26.5 % net electrical efficiency, 19.7 kW_e DC). It was pointed out that the reason the CH_4-containing fuels yielded a better performance was because of the role the endothermic reforming reactions played in recovering thermal energy from the tail gas stream and converting it to chemical energy. Contrastingly, in the syngas feeding case, no reforming occurred and a greater proportion of thermal energy was simply evacuated from the system. Thus, the benefit of incorporating endothermic fuel processing was demonstrated [54].

In 2007, Wheeldon *et al*. [3] developed a steady-state process model of a biogas-fed SOFC system in order to estimate how such a system would perform at three different WWTPs in Ontario.

The process included an initial AC adsorbent stage for H_2S removal, making this the first modeled system to include some level of biogas purification. Also included were two reformers (one for DR, one for MSR), an anode feed compressor, stack, afterburner, air compressor and water pump. Similar to the cases of Van herle *et al*. [13] and Van herle *et al*. [39], the flow sequence of the tail gas was not defined and the various heat flows were simply tallied to determine the system surplus.

The process model was developed using the UniSim Design™ simulation software, but many of the modeling approaches were similar to those taken by Van herle *et al*. [13] and Van herle *et al*. [39]. For example, the reformers and stack were isothermal and operated at pre-set temperatures, and chemical equilibrium was assumed. However, contrary to those works, the cell model was much simpler. For example, the electrical power output was based on a simple calculation that assumed the stack was 47 % electrically efficient at 80 % fuel utilization [3].

Only one performance case was calculated for each facility. In each case, the facility's average biogas production rate and composition were set as the process feed conditions. In all cases, the reformers and stack temperatures were set to 800°C, the steam-to-carbon ratio was set to 3, the excess air ratio was set to 3

(cathode feed), and the stack pressure was set to 1.1 bar. A summary of the results is presented in table 2.3.3.

Table 2.3.3. Results from the Wheeldon *et al*. (2007) [3] simulations.

	Ravensview (Kingston)	Humber (Toronto)	Ashbridges Bay (Toronto)
Biogas production rate ($m^3 \cdot day^{-1}$)	1900	25000	48600
Biogas H_2S loading (ppmv)	2.5	146	26
Estimated required AC ($kg \cdot year^{-1}$)	0.95	715	61
Net power output (kW_e)	117	1500	3100
Thermal power output, P_{th} (kW_{th})	249	1900	4000
Net CHP efficiency (HHV basis) (%)	55	58	60

Subsequently, based on the above results, a representative CHP efficiency of 60% was assumed for biogas-fed SOFC systems; applying this value to province-wide sewage biogas production data, it was estimated that a total of 1.27 $GWh \cdot day^{-1}$ (electrical plus thermal) could be recovered using SOFC technology in Ontario [3].

Carbon dioxide is often viewed as a useful biogas constituent because it can be used to process fuel through the DR reaction. At the same time, however, it dilutes the energy content of the biogas and can consume H_2 via the WGS reaction. In 2009, Piroonlerkgul *et al*. [55] developed the steady-state process models of five different biogas-fed PSOFC systems, four of which included membrane-based CO_2-removal modules. A series of sensitivity analyses were carried out to compare the system performances [55].

The first system served as a reference system and did not include a CO_2 removal model. The process flow was very similar to that presented by Van herle *et al*. [39] with dry-SR fuel processing. Similar to the cases of Van herle *et al*. [13], Van herle *et al*. [39], and Wheeldon *et al*. [3], the heat exchanger network was not defined and the various system heat flows were tallied to determine the excess amount.

The remaining four systems were variations of the reference system and each included a single CO_2 removal module. Two of the systems had the module at the entrance for removing CO_2 directly from the feed biogas. The remaining two systems had the module directly after the fuel processor for removing CO_2 from the anode feed stream. For each of these pairings, there was a vacuum pump

case and a sweep gas case. In the two vacuum pump cases, the permeate stream was fed back to the afterburner so that the fuel leaked through the membrane could be recycled (combusted). In the two sweep gas cases, the permeate stream was simply exhausted from the system because it was considered too lean to be of use [55].

All five models were developed using Microsoft Visual Basic™. Many of the modeling approaches and assumptions were similar to the ones of the previous works by Van herle *et al*. [13], Van herle *et al*. [39], and Wheeldon *et al*. [3] (*i.e*. isothermal reformer and stack, chemical equilibrium). However, the Piroonlerkgul *et al*. [55] systems were unique in one critical way: their stack sizes were not set, but were allowed to scale as a calculated degree of freedom throughout the sensitivity analyses according to constant stack temperature (800°C) and cell voltage (0.7) settings.

The sensitivity analyses were carried out as follows: first, for the four membrane module systems, membrane area was swept; second, for the sweep gas systems, the sweep gas flow rate was swept and; third, for the vacuum pump systems, the permeate stream pressure was swept. The various performance metrics calculated throughout the analyses were total cell area (stack size), power density, net electrical efficiency, CO_2 removal efficiency, and fuel leakage through the membrane (H_2, CO, and CH_4) [55].

The reference system achieved a net electrical efficiency of 52.5 % (LHV basis) and power density of 0.290 $W \cdot cm^{-2}$. It was found that the four systems containing the CO_2-removal modules always achieved higher power density because the modules always enriched the anode feed fuel (*i.e.*, led to a higher cell voltage for a given current and stack size). With that said, the case for electrical efficiency was not so unanimous. The only system capable of surpassing the electrical efficiency of the reference system was the one that removed CO_2 directly from the biogas using the vacuum pump; for this system, a membrane area and permeate pressure were found that yielded a maximum net electrical efficiency of 52.65 %. The sweep gas systems never achieved the electrical efficiency of the reference system due to the high amount of fuel leaked through the membrane and exhausted with the sweep gas [55].

Farhad *et al*. [9] developed steady-state process models of three biogas-fed SOFC systems to assess their hypothetical operation at the Robert O. Pickard WWTP in Ottawa, Ontario. The three systems varied according to their fuel processing technology. The three systems were identified as “AGR”, “SR”, and “POX” indicating the use of anode gas recycling, dry-steam reforming, and dry-partial oxidation, respectively.

The process flows of the three systems were presented in a single diagram with the key differences overlaid. All systems included a “reformer control volume” in which dry-POX or dry-SR was carried out. It was mentioned

that the reformer control volume was also capable of carrying out biogas purification, but details were not provided. In addition, the process flow included a PSOFC stack, afterburner, recuperative heat exchangers, and an air blower. In the "AGR" case, the AGR stream was fed back to the "reformer control volume". In the "SR" and "POX" cases, H_2O or air were provided externally to the "reformer control volume". The heat exchanger network was detailed except for the sequence within the "reformer control volume". Before exiting the system, the tail gas passed through a final heat exchanger which generated hot water for district heating (provided the system thermal output) [9].

The modeling software was not mentioned by Farhad *et al*. [9], but many of the modeling approaches were. Similar to the cases of Van herle *et al*. [13], Van herle *et al*. [39], Wheeldon *et al*. [3], and Piroonlerkgul *et al*. [55], the reformer and stack temperature were isothermal and chemical equilibrium was assumed. Importantly, the models of Farhad *et al*. [9] were similar to those of Piroonlerkgul *et al*. [55] in that the stack sizes were left as a model-calculated degree of freedom relative to constant stack temperature (800°C) and cell voltage (0.7) settings. Mention was made by Farhad *et al*. [9] that the cell models were programmed according to the physical characteristics of the ACS 3 PSOFCs manufactured by H.C. Starck [9].

At reference conditions, the "AGR" system achieved the highest net electrical efficiency (45.1 %, LHV basis) and produced the highest amount of net electrical power (2.92 MW_e). Relative to the "AGR" system, the "SR" system achieved a slightly reduced net electrical efficiency (43.0 %) and produced slightly less net electrical power (2.78 MW_e), but had the highest power density of the three systems. The "POX" system achieved the lowest net electrical efficiency (33.0 %) and net electrical power output (2.14 MW_e), but produced the most thermal power which led to it having the highest CHP efficiency of all three systems [9]. Based on these performances, the authors remarked that the "POX" system would be unsuitable for the Picard WWTP because it would produce an excess of heat that would have to be rejected to the environment. Furthermore, the net electrical efficiency was only about the same as that of the currently-installed reciprocating engines (32 %). The "AGR" and "SR" systems were claimed to be more suitable because they provided enough heat for the facility and produced an excess of electricity that could be sold back to the utility company [9].

The sensitivity analysis yielded some interesting results: for all three systems, increasing the fuel utilization and operating voltage always enhanced the electrical performance (efficiency and power output), but decreased the thermal power output and increased the number of required cells. Again, these were the performance trends of process configurations as opposed the performance trends of systems sized in absolute terms [9].

The first found literature to assess the steady-state performance of a fully integrated AD-SOFC system was published by Corigliano *et al*. (2010) [10]. The work was carried out in order to assess the system's possible performance operating on-site of the University of Calabria [10].

The process flow had three main sections within the system boundary. The first section included the digester stages which accepted the raw organic waste collected at the University. The second section included a CO_2-removal module which accepted the digester gas and produced a CH_4-rich retentate stream. The CH_4-rich retentate stream was fed to the third section which included two Siemens-Westinghouse 110 kW_e (nominal) power generators in parallel operation. Details were somewhat limited, but the process flow within the generators included a reformer co-fed by an AGR (dry-SR), a TSOFC stack, afterburner and recuperative heat exchanger network capable of stream pre-heating and providing a thermal power output. Therefore, these power generators were CHP generators. A portion of the thermal power output was supplied to the digesters before exiting the system boundary, but the mechanism was not detailed [10].

Contrary to the previously discussed works, the Corigliano *et al*. [10] model may best be described as a collection of spreadsheet calculations. An iterative procedure was used to size the digester according to the collection rate and quality of the organic material. Empirical correlations were used to estimate the production rate of the digester gas (1940 $m^3 \cdot day^{-1}$); this calculated production rate was what initially indicated that two power generators should be used. To calculate the net performance of the power generators, a data set was consulted that displayed the performance of a single generator relative to the CH_4/CO_2 feed composition (useful downstream of the CO_2-removal module). It was assumed that the system components external to the power generators (digesters, pumps, blowers, etc.) would consume 15 % of the electrical power and 35 % of the thermal power produced by power generators [10].

Corigliano *et al*. [10] considered performance cases relative to varying degrees of CO_2 removal from the biogas. For the case of 100 % CO_2 removal, net electrical and thermal power generation were estimated to be 212 kW_e and 115 kW_{th} at 40 and 61 % electrical and CHP efficiency (LHV basis), respectively. When a digester gas composition of 40 % CO_2/60 % CH_4 was fed to the power generators, the net electrical power output and efficiency dropped to 157 kW_e and 29.3 %, respectively [10].

The authors carried out an analysis to compare how the integrated system would perform if the two TSOFC power generators were replaced by a reciprocating engine or a microturbine (assuming 100 % CO_2 removal from the digester gas). Shown in table 2.3.4 is that the electrical performance of the TSOFC system was superior.

Table 2.3.4. Comparative electrical performances of integrated systems based on TSOFC, reciprocating engine, and microturbine technology as calculated by Corigliano *et al*. (2010) [10].

	Generator Type		
	TSOFC	Reciprocating Engine	Microturbine
Net electrical power (kW_e)	212	146	132
Net electrical efficiency (LHV basis) (%)	40	27	25
Net thermal power, P_{th} (kW_{th})	115	185	182
Net CHP efficiency (LHV basis) (%)	61	62	58

However, also shown in table 2.3.5 is that the CHP efficiencies of the reciprocating engine and microturbine systems were competitive because of their superior thermal power outputs.

2.3. Demonstration Studies

In 2004, Van herle *et al*. [19] reported the demonstration of an integrated AD-SOFC system carried out at Maison Blanche in Lully, Switzerland. For the demonstration, a 50-cell Sulzer Hexis PSOFC CHP power generator of 1 kW_e size (nominal) was coupled to an on-site digester system that provided 35 $m^3 \cdot day^{-1}$ of biogas (approx. 60 % CH_4, 40 % CO_2, between 70 and 700 ppmv H_2S) [13, 19].

Van herle *et al*. [19] provided a basic illustration of the power generator: the process included a dry-SR reformer (IIR), a 50-cell PSOFC stack, afterburner section, an air blower, and recuperative heat exchange zones for stream pre-heating and the generation of hot water for district heating. For biogas purification, only the use of AC was mentioned [19]. Reportedly, the system was operated for 1 year and was able to provide an electrical power output at 28 % electrical efficiency (LHV basis) [39]. Additional details were not provided.

Four years later, in 2008, researchers at Fraunhofer IKTS demonstrated an integrated AD-SOFC pilot plant system which was installed on-site of a WWTP in Rosswein, Germany. The pilot plant appeared to be quite comprehensive. Indicated in the process flow was a digestion stage, a biogas purification stage using a proprietary AC adsorbent, a dry-POX reformer, two 40-celled PSOFC stacks, an afterburner and a recuperative heat exchange network. Available information indicated that the tail gas stream supplied a thermal duty to the

digesters making this an SOFC system that has been highly integrated with the digestion process [16, 56, 57].

In their 2008 annual report, Fraunhofer IKTS claimed a total of 1600 operating hours for the system. The maximum gross electrical power output and efficiency were reported as being 1.32 kW_e and 43.9 % (unknown heating value basis), respectively [16]. The net performance values of the fully integrated system were not provided. During the testing period, the system was operated on both simulated biogas and raw biogas that was derived from the system digesters. The purification system was reported to remove the full spectrum of contaminants, including sulphurous and siloxane compounds, but actual performance in terms of adsorbent capacity and selectivity were not provided. Some technical difficulty was noted for the case of raw biogas feeding; specifically, it was difficult to maintain uniform conditions within the digesters (*i.e.*, foam formation) which resulted in widely fluctuating biogas compositions. These fluctuations turned out to be a challenge for the control system [56].

In 2010, Wartsila advertised on their company website that one of their WFC20 units had been successfully operated on landfill gas at the Vaasa Housing fair in Finland [58]. The WFC20 is a packaged PSOFC unit that includes a control system and all balance of plant components necessary for start up and long-term operation [42]. According to an online presentation [42], the process flow of the unit included activated carbon beds for contaminant removal, a pre-reformer co-fed by an AGR (pre-reforming followed by dry-SR DIR within the cells), a PSOFC stack, afterburner, and a recuperative heat exchanger network for pre-heating and hot water generation for district heating [42].

More than 1500 operating hours were claimed for the system [58], but it is not clear how much of this time was committed solely to the direct feeding of landfill gas. Also claimed were achieved power outputs of 20 kW_e and 17 kW_{th} [58], and net electrical and CHP efficiencies of 43 % and 76 % (LHV basis), respectively [42]. The AC bed was claimed to lower the contaminant loadings to acceptable levels [59], but, as with the previous demonstrations, adsorbent capacity and selectivity were not provided.

The Biocell project funded by the European Life+ Program culminated in the demonstration of an integrated AD-SOFC pilot plant system, which was installed and maintained at the Mataro WWTP in Spain. The project duration lasted from early 2009 to mid 2012 and included a host of industrial partners which collaborated on the construction. The process flow was essentially a pre-commercial Staxera-EBZ PSOFC CHP power generator linked to a very extensive biogas purification system [60].

The Biocell process accepted raw biogas (approx. approx. 0.86 $Nm^3 \cdot h^{-1}$, 3000 ppmv H_2S) from the one of the digesters of the WWTP. The purification

sequence began with a biofiltration stage for bulk H_2S removal which was followed by an iron-oxide adsorbent stage for H_2S polishing. The biogas then passed through a chiller for dehumidification and AC adsorbent stages for siloxane removal. The purified biogas stream was then fed to the aforementioned PSOFC CHP power generator [60]. The contents of the Staxera-EBZ unit are not outlined in the Biocell report, but an alternate literature [41] indicated that the power generator included a pre-reformer (pre-reforming followed dry-SR DIR within the cells), a PSOFC stack, afterburner, and recuperative heat exchanger network for pre-heating and the generation of a hot water [41].

Some difficulties were reported during operation of the Biocell process. The biofiltration unit was prone to leaking and experienced a control sensor failure. In addition, basic engineering and design flaws were discovered for the iron sponge polishing system. Lastly, the power generator had to be returned to Staxera-EBZ for the sealing of a leak in the afterburner zone. Following all repairs, the integrated system was operated successfully for a one month period and was able to achieve net power outputs of 0.79 kW_e and 1.98 kW_{th}. The integrated system achieved net electrical and net CHP efficiencies of 14.8 % and 52.4 % (unknown heating value basis), respectively. These low efficiencies were likely due to the high parasitic consumption of the extensive purification system. The system was not restarted after the one month operating period because the project duration had officially ended [60].

The demonstrations reported in this section were the only found examples of integrated AD-SOFC systems in physical operation. A lot of this is because, prior to 2010, SOFCs remained in the pre-commercial phase [1]. The main reasons for this are as follows: the high operating temperatures of SOFCs increases the expense of their construction materials and BOP components; the cells have been prone to failure due to thermal stress, sealing leaks, and corrosion of metal components; and the cell fabrication process is challenging, which contributes to their final expense [25]. With that said, since 2010 there has been mounting evidence that these challenges are being overcome. For example, in 2012 Adams *et al*. [22] reported that there were five companies offering SOFC systems for commercial purpose. They also reported that one of the manufacturers, Bloom Energy, has brought their system installed cost down to about $\$8000 \cdot kW_e^{-1}$ [22], which is roughly two to four times that of reciprocating engines [61]. This is a promising development for the highly efficiency SOFC technology.

In closing, the potential for integrated AD-SOFC systems at WWTPs appears to be high. Modeling studies have shown biogas-fed SOFC systems to have superior electrical performance over systems based on other CHP

technologies (*i.e.*, reciprocating engines and microturbines), especially if endothermic reforming is used [9, 10, 39].

A handful of projects have demonstrated and proven the concept of directly integrating SOFC technology with the AD process. However, only basic performances have been reported absent of any economic analysis. The system demonstrated by Wartsilla achieved efficiencies that approach what has been predicted by the modeling studies (for systems in which the digester power consumption has not been considered). Comparing the high performance of the Wartsilla system with the low performance of the Biocell system, it is evident that complex purification systems involving mechanical units (such as biotrickling filters and chillers) can dramatically reduce the overall efficiency. Both Fraunhofer IKTS and Wartsilla claim to have been able to remove the full spectrum of biogas contaminants using AC alone with their demonstration systems [56, 59]. However, this is always possible if a large enough quantity of the adsorbent is used. In both cases, the amount of adsorbent used and its capacity were not indicated.

There are currently no known instances of integrated AD-SOFC systems in long-term operation. However, this type of highly efficient system will become more attractive for biogas utilization applications as the commercial status of SOFC systems advances and their overall cost is reduced.

The pilot plant process developed in this work is considered to be a technological advancement in the field of integrated AD-SOFC systems because it includes a purification subsystem comprised of inexpensive adsorbent materials that selectively targets the main contaminant species of concern, H_2S and siloxane. In addition, the process model was enhanced to include real stack performance via a calibrated empirical cell model. Endothermic reforming (IIR) has been also been incorporated to ensure that the system out-perform conventional CHP technologies in terms of electrical efficiency.

In subsequent sections, the process model is used as design tool to explore the feasible operating region for performance. Estimates for the maximum system performance are ultimately provided in section 4.2.5.

3. METHODOLOGY AND DEVELOPMENT

Section 3 focuses on the development of the pilot plant process model. In section 3.1, the experiments used to generate the TSOFC stack performance data are presented. In section 3.2, the empirical cell model and its calibration to the stack performance data are discussed. Lastly, in section 3.3, the process model of the pilot plant, itself, is presented.

3.1. Experimental Data Collection

Stack performance data was collected using a test rig supporting environment made available by Canadian Shield Energy Systems (CanSES). Figure 3.1.1 is a photograph of the CanSES test rig.

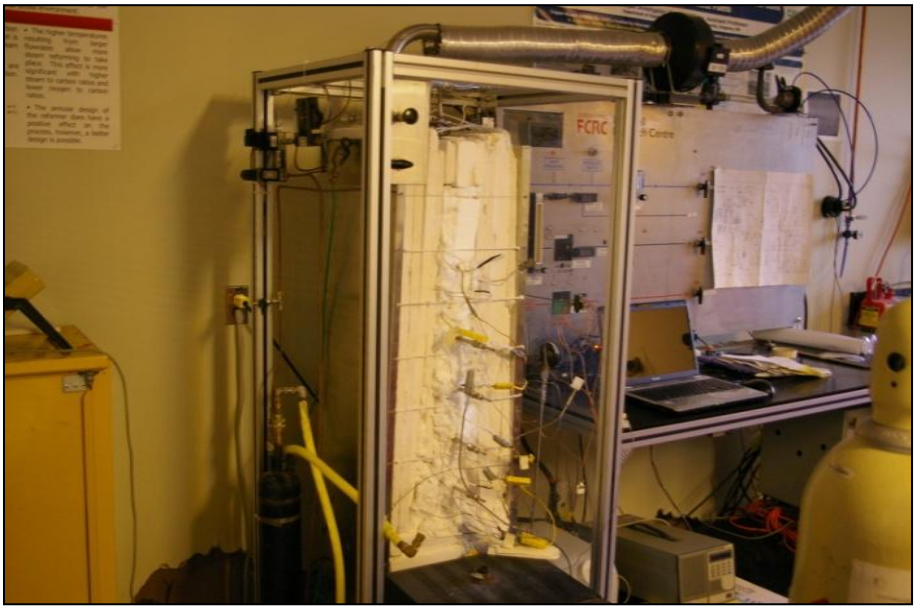

Figure 3.1.1. Experimental TSOFC test rig provided by Canadian Shield Energy Systems (CanSES).

The CanSES test rig can be configured in a variety of ways depending on the nature of the experiments, but there are some central features. The core of the system is comprised of an insulated SOFC hotbox lined with resistive heaters, a post-combustion zone, and a recuperator zone for pre-heating the cathode air feed from ambient temperature. The system is also equipped with other features such as a water pump, steam generator, gas linkages for cylinder feeds, metering valves, mass flow controllers, a furnace for pre-heating anode-side feed streams, a centrifugal blower for controlling the cathode air feed rate, an AMREL FEL 300-1 programmable load for the controlling stack current, and various thermocouples, voltage taps, and pressure sensors for monitoring system performance. System control and data logging are carried out by a laptop linked to a National Instruments cDAQ-9178 data acquisition system and a pair of side panels containing modules for field power distribution.

The CanSES test rig configuration, as used in this work, is presented in figure 3.1.2.

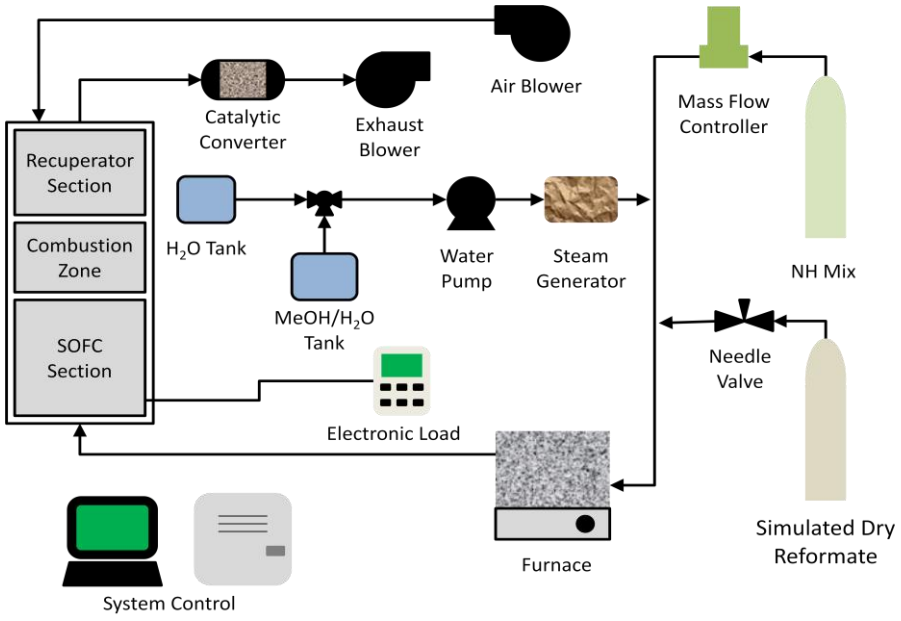

Figure 3.1.2. Configuration of the experimental TSOFC test rig used in this work.

After being pre-heated in the furnace, all anode-side flow streams ("NH mix", "MeOH/H_2O", "H_2O", and "simulated dry reformate") are fed into the bottom of the CanSES unit to the bottom of the cells. Air is blown into the top of the CanSES unit and to the bottom of the cells via thin alumina feed tubes. There is one feed tube per cell and each of these tubes passes through both the recuperator and combustion zones in order to pre-heat the air feed. After passing through the cells, the depleted anode and cathode streams are burned in the combustion zone to produce a hot tail gas. The tail gas then passes through the recuperator to pre-heat the air feed. Before exiting the system, the tail gas is passed through a catalytic converter to ensure that all hydrogen equivalents (H_2 and CO) are fully combusted. A P&ID for the system is presented in Appendix A. The corresponding tag lists for the P&ID are provided in Appendix B.

The demonstration stack was leased from TOTO Ltd. and consisted of 8 identical TSOFCs of 200 cm^2 of active surface area and 30 W_e nominal power output rating. The cells of the stack were arranged into 2 parallel rows of 4 cells in series. Other information pertaining to cell materials, dimensions, and performance was considered proprietary by the manufacturer and was not provided.

The purpose of the experiments was to collect performance data as a function of temperature, current and flow stream composition for the stack operating in the ohmic region (see section 2.1) on simulated biogas reformate. However, there were a handful of operating constraints that had to be adhered to during system operation. The constraints are listed below in table 3.1.1. Noting these constraints and the fact that the stack behavior was not known in advance, the operating boundaries could only be discovered during real-time operation. Therefore, all that was proposed ahead of time in terms of a data-collecting procedure was that a sweep pattern be used. This sweep pattern is presented later in this section.

The CanSES system did not include a fuel processor so a simulated biogas reformate mixture had to be provided to the stack during the experiments. To carry this out, two compositions referred to as the "simulated reformate" and "simulated dry reformate" had to be calculated in advance. The calculations of these mixtures are briefly described in the following paragraph. For greater detail, the reader is referred to Appendix C.

Table 3.1.1. Operating constraints followed during the experiments.

Constraint	Justification
The cell voltage must remain above 0.62 V	There is an elevated risk of cell degradation if the cell degradation at low voltage [61]
The thermal gradient along the length of the cells must be less than 150°C	High thermal stress can lead to mechanical degradation of the cells [61]
The bottom of the cells must remain approx. 50°C cooler than the average stack temperature	The local current density is greater at the bottom of the cells, so damage from resistive heating in this part of the cell must be mitigated [61]
The air feed rate to the stack must be at least 4 times the amount required to combust all of the fuel in the anode feed	There is a risk of overheating the combustion zone at low air flow rates and all fuel should be combusted before entering the building's exhaust system [61]
The "simulated dry reformate" feed rate must remain below 5.5 SLPM	The maximum flow rate of the mass flow meter calibration was 5.5 SLPM
The water feed rate must remain below 3.0 $mL \cdot min^{-1}$ (as liquid feed at 25°C)	The maximum flow rate of the water pump calibration was 3.0 $mL \cdot min^{-1}$

To begin, "simulated reformate" refers to the gas composition fed directly to the stack during the experiments and is an estimate for the gas composition that will be exiting the steam reformer in the pilot plant. The composition was determined through an equilibrium calculation in which a model biogas mixture was reacted with steam at a steam-to-carbon ratio of 2.76, pressure of 1atm, and temperature of 800°C (estimated operating conditions of the pilot plant steam reformer). The calculation, itself, was carried out using a basic steam reformer simulation developed in UniSim Design™. The stream exiting the steam reformer was taken as the simulated reformate composition and contained about 38.6 vol. % H_2O. The dry composition of the simulated reformate – the "simulated dry reformate" – was calculated using a knock-out drum which was added to the simulation. A chemical manufacturer was contacted to provide a gas cylinder with the simulated dry reformate composition. During the experiments, the simulated reformate composition was reconstituted by combining the cylinder mixture with the appropriate amount of H_2O/steam. The compositions of both the simulated reformate and simulated dry reformate are listed in table 3.1.2.

Table 3.1.2. Compositions of the simulated reformate (model-calculated) and simulated dry reformate (model-calculated and actual).

Gas Description	Gas Composition				
	H_2 (%)	CO_2 (%)	CO (%)	N_2 (%)	H_2O (%)
Simulated reformate (model calculated)	40.8	10.1	9.8	0.5	38.6
Simulated dry reformate (model calculated)	65.4	16.2	15.8	0.7	0
Simulated dry reformate (cylinder mixture)	66.7	16.5	16.1	0.7	0

The experiments began with a gradual heating of the stack over a 45-hour period to approximately 670°C. Throughout this period, the rate of increase of the average stack temperature was kept below $60°C \cdot h^{-1}$ and an air feed rate of 30 SLPM was maintained on the cathode side. A reducing environment on the anode side was maintained using NH mix gas (4% H_2, 96% N_2) and a methanol/H_2O mixture ("MeOH/H_2O" mixture in figure 3.1.2) which chemically decomposed in the furnace to produce a H_2-rich fuel stream. After the 45-hour heating period, approximately 10 h were spent in a trial mode whereby current was drawn and the system controls were tested. The current was then discontinued and the heated system was left overnight on a steady flow of air (30 SLPM) and NH Mix (2 SLPM). The NH mix feed was necessary to maintain the anode reducing environment and ensure that the anode catalytic sites were sufficiently activated [63, 64] for the main data collection period which occurred the following day.

Once the stack was brought to a reasonable average stack temperature (greater than 750°C) the programmable load was turned on and the simulated reformate mixture was fed. Data collection began and was carried out according to the aforementioned sweep pattern which is now divulged to the reader in figure 3.1.3.

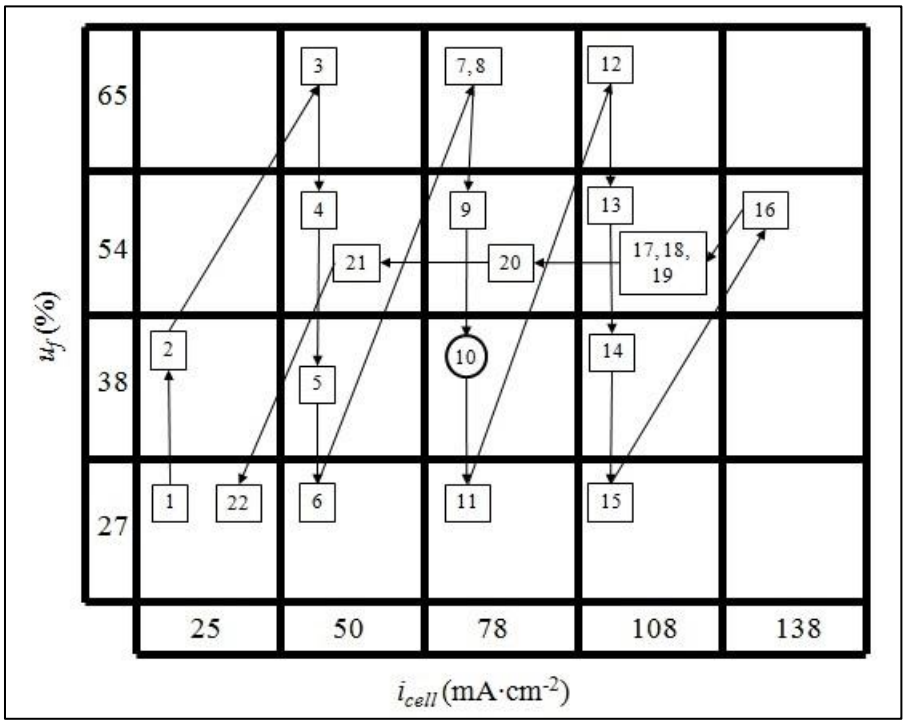

Figure 3.1.3. Sweep pattern used to collect the experimental data.

Figure 3.1.3 shows that a total of 22 data points were collected. Because the system was in continuous operation, the data points were essentially snapshots of the system operation at particular points in time. To "collect" a data point, the time into the experiment was recorded so that the instrument measurements at that time could be identified later in the log file. At least 2 minutes and 10 anode flow stream turnovers were allowed to pass before a data point was considered eligible for collection. As will be explained in the next section, data point 10 was selected to serve as the "reference data point" during the calibration procedure and has been circled in figure 3.1.3 to set it apart from the other data. The data points are organized graphically into current–voltage plots in Appendix C.

Referring to figure 3.1.3, data point 1 was collected at a current density of 25 mA·cm^{-2} and fuel utilization of 27 %. This was considered a reasonable starting point because the cell voltage (0.85 V) was well above its lower constraint and the flow rates of the water (0.66 mL·min^{-1}) and simulated dry reformate (1.3 SLPM) were well below their upper constraints (see table 3.1.1). Data point 2 was collected at 25 mA·cm^{-2} and 38 % fuel utilization, and was achieved by reducing the simulated reformate flow rate (*i.e.*, by reducing the simulated dry reformate

and water flow rates in proportion to each other). The third data point was achieved by increasing the current density to 50 $mA \cdot cm^{-2}$. The remaining data points were achieved by making adjustments to the current density and simulated reformate. Adjustments were also made to the heater power outputs and air feed rate in order to manage the stack thermal gradients. The sweep pattern depicted up to data point 16 was followed for two reasons; first, it ensured that reasonable spread of data points were collected in the ohmic region; second, it allowed the constraints of table 3.1.1 (*i.e.*, lower cell voltage, upper water flow rate and upper simulated dry reformate flow rate) to be approached slowly and safely. At data point 16, the upper limit of the simulated dry reformate flow rate (5.5 SLPM) was approached and the sweep was stopped. The operating pattern was then followed back along a path of 54 % fuel utilization in an attempt to collect duplicate data points. Throughout the data collection, the stack operating pressure was approximately atmospheric.

As will be discussed in the next section, calibration of the empirical cell model required that the stack performance data be further manipulated prior to regression. For each data point, the following variables had to be calculated from the log file: average cell current density (i_{cell}), average cell temperature (T_{cell}), average cell partial pressures of H_2, H_2O, and O_2 ($\bar{p}_{H2}$, $\bar{p}_{H2O}$, and $\bar{p}_{O2}$, respectively), and the average cell voltage (V_{cell}).

The i_{cell} values were calculated as the total stack current (in mA) divided by the number of cell rows in parallel (*i.e.*, 2) and the cell active surface area (*i.e.*, 200 cm^2).

To calculate the T_{cell} values, the temperature measurements made at the bottom, middle, and top of the stack had to be considered. First, the arithmetic averages of each section were calculated. Then the final T_{cell} values were determined by arithmetically averaging the three sectional averages.

The $\bar{p}_{H2}$, $\bar{p}_{H2O}$, and $\bar{p}_{O2}$ values calculated as the arithmetic average of the inlet and outlet partial pressures. A pressure of 1 atm was assumed for the calculations (corroborated by pressure measurements). On the anode side, chemical equilibrium was assumed at both the inlet and outlet of the stack (*i.e.*, WGS equilibrium). On both the anode and cathode sides, the outlet compositions were adjusted according to the electrochemical consumption.

The V_{cell} values were calculated as the total stack voltage divided by the number of cells in series (*i.e.*, 4) in each of the cell rows.

The values for all 22 data points are listed in tabular form in Appendix D, but the ranges of their values are listed in table 3.1.3.

Table 3.1.3. Approximate ranges of i_{cell}, T_{cell}, $\bar{p}_{H2}$, $\bar{p}_{H2O}$, $\bar{p}_{O2}$, and V_{cell} for the data.

Variable	Low	High
i_{cell} (mA·cm^{-2})	25	138
T_{cell} (°C)	785	821
$\bar{p}_{H2}$ (bar)	0.27	0.36
$\bar{p}_{H2O}$ (bar)	0.45	0.54
$\bar{p}_{O2}$ (bar)	0.21	0.21
V_{cell} (V)	0.60	0.85

Notably, it was not possible to collect a broad range of $\bar{p}_{O2}$ values because adhering to the air feed rate constraint meant that the amount of O_2 passing through the cathodes was far in excess of the electrochemical consumption rate.

Due to the complexities of managing the stack temperature, it was difficult to acquire duplicate samples. Samples 4 and 21 had the same operating condition settings and were the closest two data points in terms of average stack temperature; therefore, they were selected as the best candidates for being considered duplicates. A comparison between these two data points is made in table 3.1.4.

Table 3.1.4. Comparison between duplicate data points, 4 and 21.

Sample #	i_{cell} (mA·cm^{-2})	u_f (%)	$r_{H2O/C}$ of the anode feed	T_{cell} (°C)	V_{cell} (V)
4	50	54	2.0	811	0.78
21	50	55	2.0	814	0.79

The close agreement in cell voltage between these two suggests that cell activity was consistent throughout the 6-hour data collection period.

3.2. Cell Model Development and Calibration

The empirical cell model developed in this work was inspired by the work of Campanari (2001) [65]. At the heart of the Campanari [65] model is a single polarization curve collected at experimental conditions referred to as the "reference conditions". In order to extrapolate cell voltages away from the reference conditions, Campanari [65] considered a family of correlations published by Hirschenhofer *et al*. (1994) [66]:

$$\Delta V_{cell,a} = C_a \ln\left(\frac{(\bar{p}_{H2,2}/\bar{p}_{H2O,2})}{(\bar{p}_{H2,1,}/\bar{p}_{H2O,1})}\right) \quad (3.2.1)$$

$$\Delta V_{cell,c} = C_c \ln\left(\frac{\bar{p}_{O2,2}}{\bar{p}_{O2,1}}\right) \quad (3.2.2)$$

$$\Delta V_{cell,T} = C_T\left(T_{cell,2} - T_{cell,1}\right) i_{cell,2} \quad (3.2.3)$$

$$\Delta V_{cell,i} = C_i\left(i_{cell,2} - i_{cell,1}\right) \quad (3.2.4)$$

$$\Delta V_{cell,p} = C_p \ln\left(\frac{p_{cell,2}}{p_{cell,1}}\right) \quad (3.2.5)$$

where C_a, C_c, C_T, C_i, and C_p are empirical constants. As further explained by EG&G Technical Services, Inc. (2004) [25], the correlations can be used to estimate the voltage difference between two operating points, "1" and "2", residing within the ohmic region of the polarization curve. From top to bottom (expression 3.2.1 down to 3.2.5), the correlations estimate the difference in voltage arising from the difference in average anode composition, difference in average cathode composition, difference in average cell temperature, difference in average cell current density, and difference in total cell pressure, respectively. To calculate the total voltage difference between points "1" and "2", the correlations are simply added as shown:

$$V_{cell,2} - V_{cell,1} = \Delta V_{cell,a} + \Delta V_{cell,c} + \Delta V_{cell,T} + \Delta V_{cell,i} + \Delta V_{cell,p} \quad (3.2.6)$$

These correlations are highly empirical. For example, the mathematical form of the $\Delta V_{cell,a}$, $\Delta V_{cell,c}$, and $\Delta V_{cell,p}$ correlations are inspired by the mathematical form of Nernst equation in which the terms in front of the logarithm have been replaced by empirically-estimated constants (*i.e.*, C_a, C_c, and C_p). The mathematical form of the $\Delta V_{cell,T}$ correlation is based on the behaviour observed in figure 2.1.2.; namely that, in the ohmic region, cell voltage increases with temperature but the magnitude of the voltage increase is also dependent on the current density. The mathematical form of the $\Delta V_{cell,i}$ is also based on the observed behaviour in figure 2.1.2.; namely that, in the ohmic region, a polarization curve is essentially a line.

Campanari [65] rearranged expression 3.2.6 to calculate an explicit cell voltage output, $V_{cell,2}$, as

$$V_{cell,2} = V_{cell,1} + \Delta V_{cell,a} + \Delta V_{cell,c} + \Delta V_{cell,T} + \Delta V_{cell,i} + \Delta V_{cell,p} \qquad (3.2.7)$$

Substituting the correlations into expression 3.2.7 yielded:

$$V_{cell,2} = V_{cell,1} + C_i\left(i_{cell,2} - i_{cell,1}\right) + C_T\left(T_{cell,2} - T_{cell,1}\right)i_{cell,2} + C_c ln\left(\frac{\bar{p}_{O2,2}}{\bar{p}_{O2,1}}\right) + C_a ln\left(\frac{\left(\frac{\bar{p}_{H2,2}}{\bar{p}_{H2O,2}}\right)}{\left(\frac{\bar{p}_{H2,1}}{\bar{p}_{H2O,1}}\right)}\right) + C_p \ln\left(\frac{p_{cell,2}}{p_{cell,1}}\right) \qquad (3.2.8)$$

Campanari [65] set point "1" (*i.e.*, $V_{cell,1}$, $\bar{p}_{H2,1}$, $\bar{p}_{H2O,1}$, $\bar{p}_{O2,1}$, $T_{cell,1}$, $i_{cell,1}$, $p_{cell,1}$) to values derived from their experimental polarization curve (*i.e.*, their "reference conditions") and left expression 3.2.8 as a function of the point "2" operating conditions (*i.e.*, $\bar{p}_{H2,2}$, $\bar{p}_{H2O,2}$, $\bar{p}_{O2,2}$, $T_{cell,2}$, $i_{cell,2}$, $p_{cell,2}$).

The C_a, C_c, C_T, C_i, and C_p values used by Campanari [65] were referenced from the literature and, therefore, were not specific to their experimental cells. In this work expression 3.2.8 was used as the basis for the empirical cell model, but the correlation constants were treated as regression coefficients. In addition, the $\Delta V_{cell,p}$ correlation was dropped from further consideration because the cell performance data was collected at atmospheric conditions and the process model assumes atmospheric pressure for the stack.

The fact that the data collected in section 3.1 was not carried out with the intent of producing a well-defined polarization curve meant that a different means

of establishing the point "1" values had to be adopted. The approach taken was to consider a single "reference point" as opposed to an entire reference polarization curve. Specifically, a single data point was selected-out from among the 22 collected in order to serve as a permanent substitution as data point "1". Data point 10 was chosen for this purpose because of its approximate central location within the data set in terms of average cell voltage, temperature, current density and fuel utilization (see Appendix D). This data point was selected from visual inspection.

Before the calibration was carried out, it was realized that there would be difficulty in regressing the C_c constant due to the narrow range of the $\bar{p}_{O2}$ values (approx. constant at 0.21 bar). Also, it was decided not to simply use the value reported in the literature [25, 65, 66] because it was for cell operation at 1000°C, which is almost 180°C higher than the highest cell temperature of the data set.

It has been demonstrated that a reasonable estimate for C_p can be determined from the Nernst Equation [34] and the same approach was followed here for C_c. To begin, if all operating conditions between two hypothetical operating points, "1" and "2", are held constant except their $\bar{p}_{O2}$ values, the Nernst Equation predicts the difference in cell voltage to be:

$$V_{cell,2} - V_{cell,1} = \left[\frac{(-\Delta G_R^o)}{2F} + \frac{RT_{cell}}{2F} ln\left(\frac{\bar{p}_{H2}\bar{p}_{O2,2}^{0.5}}{\bar{p}_{H2O}}\right)\right] - \left[\frac{(-\Delta G_R^o)}{2F} + \frac{RT_{cell}}{2F} ln\left(\frac{\bar{p}_{H2}\bar{p}_{O2,1}^{0.5}}{\bar{p}_{H2O}}\right)\right]$$

which simplifies to

$$V_{cell,2} - V_{cell,1} = \Delta V_{cell,c} = \left(\frac{RT_{cell}}{4F}\right) \ln\left(\frac{\bar{p}_{O2,2}}{\bar{p}_{O2,1}}\right)$$

Comparing the expression immediately above with expression 3.2.2 reveals that C_c = (RT_{cell}/$4F$). The average cell temperature of reference data point (data point 10)

was chosen as a reasonable value for T_{cell} (1088K) which yielded a value of 0.023 V for C_c.

With the reference data point identified (data point 10) and C_c and determined, the empirical cell model (expression 3.2.8) essentially became a function of $\bar{p}_{H2,2}$, $\bar{p}_{H2O,2}$, $\bar{p}_{O2,2}$, $T_{cell,2}$, and $i_{cell,2}$, with C_i, C_T, and C_a remaining as the regression coefficients. All that remained was to calibrate the expression to the cell data; to carry this out, a spreadsheet in Microsoft Excel™ was developed. For each of the data points (excluding data point 10) a $V_{cell,2}$ value was calculated. In each case, data point 10 was set as the reference data point, C_c was set to the value determined above (0.023 V), and C_i, C_T, and C_a were set to values suggested by EG&G Technical Services, Inc. [25] as initial guesses (see table 3.2.1 below). In addition, a residual was calculated for each data point as the difference between the measured cell voltage (V_{cell}) and the predicted cell voltage ($V_{cell,2}$). Using Excel's SOLVER utility, the values of C_i, C_T, and C_a were adjusted until the sum of the squared residuals (SSR) was minimized, which concluded the calibration procedure. The settings of the SOLVER "Options" are listed in Appendix E. Three consecutive solves were made to ensure that the SSR was minimized.

The final values for C_i, C_T, C_a, and C_c are listed in table 3.2.1 along with the values used as initial guesses provided by EG&G Services, Inc. [25]. A more thorough discussion of the regressed values is provided in section 4.1.

Table 3.2.1. Values of C_i, C_T, C_a, and C_c after cell model calibration and the values recommended for use by EG&G Services, Inc. (2004) [25]. The values provided by EG&G Services, Inc. [25] have been converted; for example, the EG&G Services, Inc. [25] correlations use base-10 logarithms and units of millivolts.

Source	C_i x 10^3 ($V \cdot cm^2 \cdot mA^{-1}$)	C_T x 10^6 ($V \cdot K^{-1} \cdot mA^{-1}$)	C_a x 10^2 (V)	C_c x 10^2 (V)
CanSES data (current work)	-1.8	8.3	7.4	2.3
EG&G Services, Inc. [13]	-0.73	40	7.5	4.0

Figure 3.2.1 depicts a parity plot of the model-predicted cell voltage ($V_{cell,2}$) versus the corresponding experimental cell voltages for the collected data points (V_{cell}).

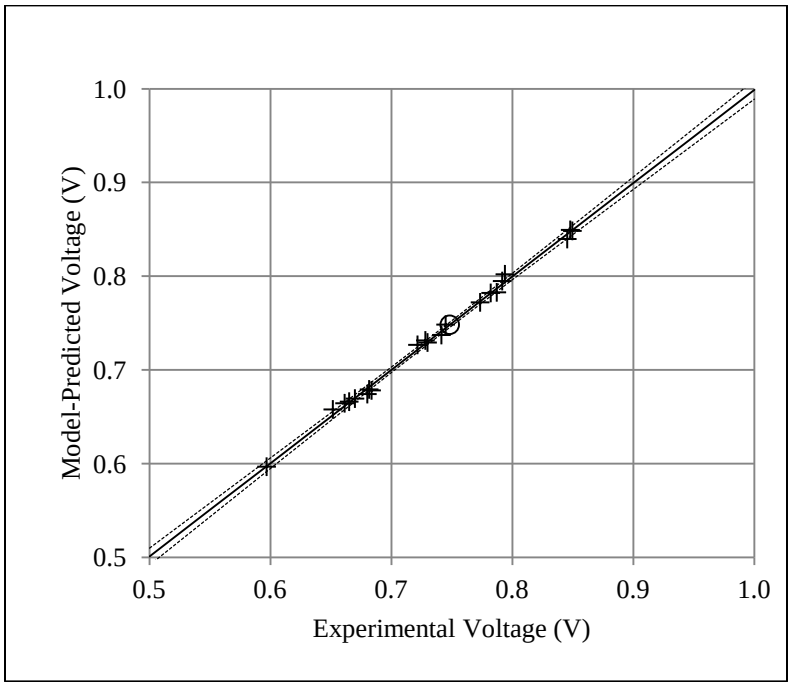

Figure 3.2.1. Parity plot of model-predicted versus experimental cell voltages for the collected data points.

Within the plot, data point 10 is represented by the open circle. The remaining 21 data points are represented by crosses. A regression line (solid black) has also been included along with plots of the upper and lower 99 % confidence intervals (dashed curves). The regressed line has a slope of 1 (0.9961), meaning that the calibrated cell model can reproduce the experimental values with a high level of accuracy; the extremely narrow confidence region indicates that this reproduction occurs with a high level of confidence.

A plot of residuals is shown in figure 3.2.2, which presents the residual values (V_{cell} - $V_{cell,2}$) as a function of data point number. The $\pm 1^{st}$, 2^{nd}, and 3^{rd} standard deviations are also included. Data point 10 is once again represented by an open circle. The magnitude of the largest residual is less than 10 mV indicating a high level of model precision; for example, an absolute error of 10 mV represents only a 2 % relative error on a cell voltage of 0.5 V. Approximately 62 % of the residuals lie between ±1 standard deviation and 100 % lie between ±2 deviations. These are very close to the values expected for normally-distributed residuals (*i.e.*, 68 % and 95 %, respectively).

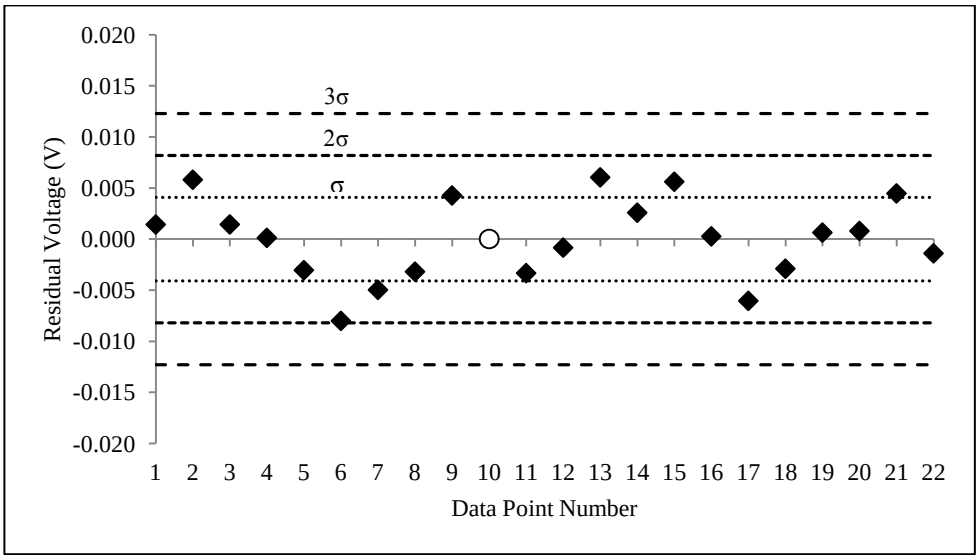

Figure 3.2.2. Plot of residual cell voltage versus data point number. Data point 10 is represented by the open circle.

3.3. Process Model and Development

A steady-state process model of the proposed pilot plant was developed using the UniSim Design™ simulation software. The process model is intended to serve as a flexible design tool capable of predicting system performance relative to design variables. UniSim Design™ is ideal for this because it contains an extensive library of pre-programmed sub-component models analogous to the various equipment and reactors available to the chemical manufacturing industry. These sub-component models can be quickly linked and organized to form larger chemical process models. In addition, UniSim Design™ also allows for the construction of spreadsheets that can be integrated with the flow sheet and programmed to carry out user-specific calculations. Once enough degrees of freedom have specified throughout the model by the user, UniSim Design™ will calculate the thermodynamic state of each material stream and sub-component in order to simulate the system in operation.

Figure 3.3.1 shows the process model as it appears within the UniSim Design™ modeling environment.

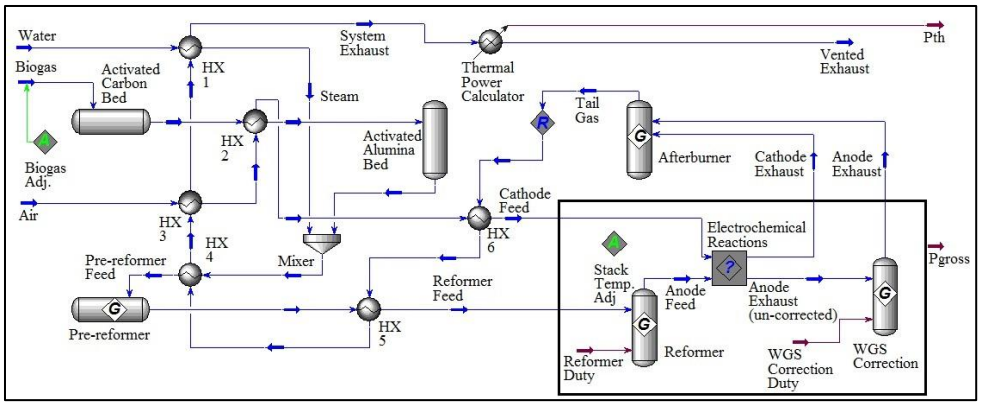

Figure 3.3.1. Process flow diagram of the proposed 2 kW_e integrated AD-SOFC pilot plant intended for construction at the Ravensview WWTP in Kingston, ON.

The process begins with the acceptance of dry biogas from a Ravensview digester. The biogas first passes through the purification sub-system which includes an alkali-impregnated AC stage for sulphur species removal and a downstream heated activated alumina stage (400°C) for siloxane removal. The purification system is based on the proven 98 % removal efficiency of H_2S using activated carbon (for biogas containing less than 200 ppmv H_2S) [3, 4], the demonstrated 100 % removal efficiency of hexamethylcyclotrisiloxane using activated alumina when heated between 250 and 400°C [31].

The purification system is followed by an adiabatic pre-reformer, which has been included for three reasons. First, the pre-reformer will convert any non-polar higher hydrocarbons not removed by the purification system into fuel before they have a chance to thermally crack at higher temperatures [40]. Second, the AC and heated activated alumina beds are expected to remove a portion of the VOCs (other than siloxanes) [30, 67, 68], but the pre-reformer will likely adsorb the remaining trace of catalyst poisons (*i.e.*, sulphur and halogens) prior to the main reformer bed(s) [69]. Third, the pre-reformed biogas stream can help keep the downstream reforming catalyst in a reduced state because of its H_2 content (approx 13 vol. % at equilibrium) [69, 70]. When the reformer feed is absent of H_2, the active sites on the catalyst (reduced nickel particles) are prone to oxidation by H_2O which deactivates the catalyst [70].

The pre-reformer exhaust is then fed to the reformer(s) located within the hotbox. Dry-SR is adopted based on previous works which found that systems using endothermic reforming provide superior electrical performance to systems

using exothermic reforming [9, 39, 54] (see section 2.2). IIR is chosen because biogas reforming has been shown to be well thermally-matched to the heat evolved from the cells [39] and the reformer position/orientation within the hotbox can be adjusted to manage the thermal gradients of the cells [71]. Although AGR can eliminate the need for an external water supply and enhance the system performance, it was not adopted at this time because of the additional complexity it adds to the system and the lack of commercially-available components required for its implementation [34, 35]. Moreover, the freedom to adjust the steam-to-carbon ratio as a fully independent operating variable was desired, so external water feeding was adopted.

UniSim Design™ does not contain an SOFC hotbox sub-component model, so one had to be developed using various UniSim™ functions and spreadsheets. Referring back to figure 3.3.1, the hotbox contents are outlined by the black box. The hotbox sub-component model is explained further in sections 3.3.1 and 3.3.2.

The process model contains a fully defined recuperative heat exchange network. On the hot-side, the network begins with a tail gas stream that has been generated from the combustion of the depleted anode and cathode exhaust streams exiting the hotbox. The tail gas stream provides the sensible heat required for pre-heating all cold-side feed streams. A notable feature of the heat exchange network is that the pre-heating of cathode air is been broken into two stages (HX 3 and HX 6). There are two reasons for this two-staged approach: first, splitting the air pre-heating into two stages leaves enough sensible heat in the tail gas stream to bring the reformer feed up to the approximate reformer temperature of 800°C; second, the air heated after the first stage (exiting HX 3 at 600°C) is well-matched to raise the temperature of the biogas stream up to the required temperature of the activated alumina bed (400°C). The remaining heat exchangers were positioned by matching their desired outlet temperatures with the temperature of the tail gas stream. Pre-heating the cathode air in two-stages was also the approach taken by Yi *et al*. [54] for their TSOFC system.

3.3.1. System Model Assumptions and Approximations

Listed below are the various assumptions inherent to the process (and cell) model:

- The process is steady-state.
- All feed streams enter at 25°C and 1 atm pressure.
- All streams and units of the system operate at 1 atm pressure (1.013 bar).

- The biogas is dehumidified prior to being fed to the system. This will be a requirement for the eventual pilot plant because moisture reduces the H_2S removal capacity of activated carbon [29]. The simplest way to achieve this dehumidification is to use an underground moisture trap [72]. For now, this step is assumed to be external to the plant boundary. As a side note, if simple dehumidification is not possible, iron sponge material may be considered in place of AC for the H_2S removal [1, 29].
- The concentration of biogas contaminants is low enough that their omission from the biogas feed does not impact the modeled system performance. This is equivalent to assuming that the various adsorption reactions and the pre-reforming of higher-hydrocarbons have little thermodynamic impact on the system performance. The error in the calculated pre-reformer temperature resulting from omission of higher hydrocarbons is estimated to be negligible in Appendix F.
- Chemical reaction only occurs within the pre-reformer, reformer, fuel cells, and afterburner. In addition, all chemical reactions are assumed to reach equilibrium (except for the electrochemical oxidation of H_2 occurring within cells, which is governed by the cell current).
- Compositions, temperatures, and pressures are assumed to be uniform in all reactors and material streams. Within the cells, the compositions of H_2, H_2O, and O_2 are also considered to be uniform; for example, the compositions of these species are considered to be uniform according to the arithmetic averages of their inlet and outlet partial pressures.
- Only H_2 is electrochemically oxidized by the anodes. This is a common assumption based on the much higher rates of diffusion and electrochemical oxidation of H_2 over CO [25]. With that said, CO is still considered to be a fuel molecule because it can react with H_2O to form H_2 via the WGS reaction. Both H_2 and CO are referred to as "H_2 equivalents".
- The hotbox and cells are assumed to operate isothermally and there is no resistance to heat flow between the SOFCs and reformer.
- The Peng-Robinson equation of state is appropriate at the modeling conditions. The Peng-Robinson equation of state is valid for multi-phase modeling over a wide range of operating conditions (temperatures as low as -271°C and pressures as high as 100000 kPa) [73]. Given the low operating pressure, low operating temperature, and simplicity of the chemical species, the ideal gas law probably would have yielded satisfactory results; however, due to the abundance of computing power, the more rigorous equation of state was used.
- The system is perfectly insulated and there are no heat losses. Ultimately, heat loss is a materials selection and economic issue, but the loss can be as little as 2 % of the incoming enthalpy flow (fuel flow rates

times the fuel LHV) for well-insulated SOFC systems [13, 19, 65]. Properly defining the heat losses also requires that the various units, including the hotbox, be fully sized so that the surface area of the insulation can be considered.

- The afterburner temperature is calculated as the adiabatic combustion temperature. This assumption produces the maximum possible afterburner temperature. In reality, the afterburner temperature will be lowered by heat losses. In addition, it is common among cathode-supported TSOFC systems to have the air feed tubes pass directly from the recuperator (HX 6), through the afterburner and into the bottom of the closed end of the cell tubes. Therefore, an amount of heat will likely be drawn from the combustion gases by the air feed tubes.
- Heat transfer only occurs within the heat exchangers and hotbox.
- The tail gas stream can reasonably provide thermal power down to a temperature of 100°C. As a result, the latent heat of condensation does not contribute to the system thermal output. With that said, schemes utilizing the heat of condensation are entirely possible. In fact, in these cases, the condensate could be recycled back to the water feed reserve. Regardless, these schemes are not considered here.

3.3.2. Process Model Calculations

Each sub-component model accepts a set of independent variables and calculates a set of dependent variables that may be passed onto other sub-component models via the material streams. In general, both independent and dependent variables can appear in either the feed or exhaust streams connected to the unit. In addition, various mechanical specifications for the units may be treated as independent or dependent variables.

All chemical reactors (pre-reformer, reformer and afterburner) have been modeled using the "Gibbs reactor", which is a UniSim Design™ sub-component model that calculates the equilibrium composition of feed streams by minimizing the Gibbs free energy of the mixture. Chemical reactions are not carried out in the material streams, but flash calculations leading to the determination of various physical properties are.

The model has been developed to calculate all feed stream flow rates as dependent variables. Specifically, these are the biogas feed rate ($\dot{n}_{biogas}$), air feed rate, ($\dot{n}_{air}$), and water feed rate, ($\dot{n}_{water}$). In addition, these flow rates are calculated from the following user-specified independent variables: fuel utilization, (u_f),

oxidant utilization, (u_{ox}), utilization, steam-to-carbon ratio (at the pre-reformer entrance), ($r_{H2O/C}$), average cell current density, ($i_{cell,2}$), cell area, (A_{cell}), and the number of cells, (N_{cell}).

$\dot{n}_{air}$ is calculated according to the following spreadsheet calculation:

$$\dot{n}_{air} = \frac{\dot{n}_{O2,elec}}{(0.21)u_{ox}} = \frac{A_{cell}N_{cell}i_{cell,2}}{(0.21)4Fu_{ox}} \quad (3.3.2.1)$$

which was derived using Faraday's constant, the stoichiometry of reaction 2.1.4 and the composition of O_2 in air (21 mol %).

$\dot{n}_{water}$ is calculated directly from $\dot{n}_{biogas}$ and $r_{H2O/C}$ as:

$$\dot{n}_{water} = (r_{H2O/C})\dot{n}_{biogas} \quad (3.3.2.2)$$

Expression 3.3.2.2 is based on the fact that there is 1 mole of carbon for every mole of biogas (*i.e.*, because CH_4 and CO_2 have 1 carbon each).

The calculation of $\dot{n}_{biogas}$ is complicated by the fact that there are chemical reactions occurring in the anode line upstream of the stack (*i.e.*, in the pre-reformer and reformer). As a result, $\dot{n}_{biogas}$ cannot be back-calculated using a simple expression and must be determined through iteration. In light of this, the calculation of $\dot{n}_{biogas}$ is broken into two parts. In the first part, a surrogate fuel utilization value, (u_f'), is calculated according to:

$$u_f' = \frac{(\dot{n}_{H2}+\dot{n}_{CO})_{elec}}{(\dot{n}_{H2}+\dot{n}_{CO})_{fuel}} = \frac{A_{cell}N_{cell}i_{cell,2}}{2F(\dot{n}_{H2}+\dot{n}_{CO})_{fuel}} \quad (3.3.2.3)$$

where $(\dot{n}_{H2} + \dot{n}_{CO})_{elec}$ is the molar consumption rate of hydrogen equivalents by the stack and $(\dot{n}_{H2} + \dot{n}_{CO})_{fuel}$ is the molar flow rate of hydrogen equivalents exiting the reformer. Similar to expression 3.3.2.1, expression 3.3.2.3 was derived using Faraday's law and the stoichiometry of reaction 2.1.4. The second part of calculation involves the iteration and is based fact that $\dot{n}_{biogas}$ influences the downstream value of $(\dot{n}_{H2} + \dot{n}_{CO})_{fuel}$ (denominator in expression 3.3.2.3). Specifically, the value of $\dot{n}_{biogas}$ is iterated by the "Biogas Adj." function (see

figure 3.3.1) until u_f' equals the u_f value specified by the user. The iteration stops when $u_f' = u_f \pm 0.01$ %; at this point the final $\dot{n}_{biogas}$ value is taken as the solved value. As a side note, $\dot{n}_{water}$ also varies throughout the iteration because it is tethered to $\dot{n}_{biogas}$ via expression 3.3.2.2.

Although the Biogas Adj. function is what solves for the biogas feed rate, the following condition was always found to be true upon convergence:

$$\dot{n}_{CH4,biogas} \approx \frac{1}{4}(\dot{n}_{H2} + \dot{n}_{CO})_{fuel} \approx \frac{1}{4}\left(\frac{i_{cell,2}A_{cell}N_{cell}}{2Fu_f}\right) \quad (3.3.2.4)$$

Expression 3.3.2.4 states that the molar flow rate of CH_4 in the feed biogas, $\dot{n}_{CH4,biogas}$, is always one quarter the molar flow rate of H_2 equivalents fed to the stack. This occurs because, at simulation conditions, CH_4 is always completely converted (> 98 %) by the end of the reformer and the MSR and DR reactions both produce four H_2 equivalents per mole of CH_4 consumed. Therefore, the full consumption of CH_4 always produces four H_2 equivalents regardless of the reaction pathway. The WGS reaction does not affect this "factor-of-four" relationship because the WGS reaction contains one mole of H_2 equivalents on either side of its chemical equation.

Referring back to expression 3.3.2.4, the contents of the far-right bracketed term are how the molar flow rate of H_2 equivalents to the stack can be hand calculated according to Faraday's Law. Because the $i_{cell,2}$, A_{cell}, N_{cell} variables are unchanged from their initial settings in this work, the only variable that later influences the $\dot{n}_{CH4,biogas}$ is u_f. The effect of fuel utilization on system performance is studied in section 4.2.4.

The heat exchangers use hot and cold stream energy balances to solve for the unknown inlet or outlet temperatures. Important and worth noting is that, in the current process model configuration, the heat exchanger areas (sizes) are calculated as dependent variables. These areas are calculated according to the log-mean temperature method,

$$A = \frac{\dot{Q}}{U \times \Delta T_{LMTD}} \quad (3.3.2.5)$$

where A is the heat exchanger surface area, $\dot{Q}$ is the rate of heat exchange between the hot and cold streams, U is the overall heat exchange coefficient, and ΔT_{LMTD} is

the log-mean temperature difference calculated across the terminal ends of the heat exchanger. The values of $\dot{Q}$ and ΔT_{LMTD} are determined from the solved inlet and outlet temperatures and energy balances. The U value for the steam generator is set to 25 $W \cdot m^{-2} \cdot C^{-1}$ while that of all other heat exchangers is set to 20 $W \cdot m^{-2} \cdot C^{-1}$. These values are the averages of the typical ranges provided by Kreith and Bohn (2001) [74].

In addition, each heat exchanger calculates a minimum approach temperature value, ΔT_{min}, which is defined as the minimum temperature difference between the hot and cold streams along the heat exchanger flow path:

$$\Delta T_{min} = (T_h - T_c)_{min} \tag{3.3.2.6}$$

Values for ΔT_{min} are a proxy for the economic viability of heat exchangers and occur at either one of the terminal ends of the heat exchanger (*i.e.*, heat exchanger inlet our outlet).

As mentioned in section 3.3, UniSim Design™ does not contain a hotbox sub-component model so one had to be developed that included both the reformer and stack. Referring back to figure 3.3.1, the hotbox boundary is depicted as the solid black rectangle. All contents within the boundary are assumed to operate isothermally and isobarically at $T_{cell,2}$ and 1 atm, respectively. The reformer is modeled as a Gibbs reactor that converts the reformer feed into an equilibrium mixture. Downstream of the reformer is the "Electrochemical Reactions" block which represents all stack spreadsheet calculations relating to the electrochemical reactions. Table 3.3.2.1 outlines how the anode and cathode streams are adjusted according to the electrochemical reactions.

Table 3.3.2.1. The mole table spreadsheet used to adjust the anode and cathode streams according to the electrochemical reactions.

Anode species	Imported anode feed flows rates ($mol \cdot s^{-1}$)	Anode flow rates after CO elimination ($mol \cdot s^{-1}$)	Anode flow rates after CO elimination and electrochemical adjustment ($mol \cdot s^{-1}$)
CO	$\dot{n}_{CO}$	$\dot{n}_{CO} - \dot{n}_{CO} = 0$	0
H_2	$\dot{n}_{H2}$	$\dot{n}_{H2} + \dot{n}_{CO}$	$\dot{n}_{H2} + \dot{n}_{CO} - \frac{i_{cell,2} A_{cell} N_{cell}}{2F}$
H_2O	$\dot{n}_{H2O}$	$\dot{n}_{H2O} - \dot{n}_{CO}$	$\dot{n}_{H2O} - \dot{n}_{CO} + \frac{i_{cell,2} A_{cell} N_{cell}}{2F}$
CO_2	$\dot{n}_{CO2}$	$\dot{n}_{CO2} + \dot{n}_{CO}$	$\dot{n}_{CO2} + \dot{n}_{CO}$
CH_4	$\dot{n}_{CH4}(\approx 0)$	$\dot{n}_{CH4}(\approx 0)$	$\dot{n}_{CH4}(\approx 0)$

Cathode species	Imported cathode feed flows rates ($mol \cdot s^{-1}$)	Cathode flow rates after electrochemical adjustment ($mol \cdot s^{-1}$)
O_2	$\dot{n}_{O2}$	$\dot{n}_{O2} - \frac{i_{cell,2} A_{cell} N_{cell}}{4F}$
N_2	$\dot{n}_{N2}$	$\dot{n}_{N2}$

Starting with the anode species, the calculations begin with all molar flow rates fed to the anodes being imported to a spreadsheet. In the second column, the approach of Wheeldon *et al.* [3] is applied whereby all CO in the anode stream is eliminated through an "artificial" forward shift of the WGS reaction. This artificial shift is eventually corrected for using an equilibrium calculation; but, initially, it simplifies the electrochemical reactions because all fuel is treated as H_2 only. In the last column, the electrochemical adjustments are applied using Faraday's law. Following the electrochemical adjustment, further adjustment of the anode species is required in order to bring the mixture into chemical equilibrium and correct for the previously applied artificial WGS shift; to this end; the anode flows are exported to the "Anode Exhaust (un-corrected)" stream and passed to the "WGS Correction" reactor. The WGS Correction reactor is just a theoretical unit (Gibbs reactor) used to carry out the equilibrium calculation at the cell temperature, $T_{cell,2}$,

and pressure (1 atm). The outlet of the WGS Correction unit is taken to be the true anode exhaust stream.

The electrochemical reaction calculations for the cathode species are much simpler. Similar to the anode species, the calculations begin with all molar flow rates fed to the cathodes being imported to a spreadsheet. Unlike the anode calculations, there is no water-gas shifting and only electrochemical adjustments are made. The values of the second column are simply exported to the "Cathode Exhaust" stream (see figure 3.3.1).

As a side note, the fuel cell model does not process CH_4, but this is not required because CH_4 is essentially fully converted before the stack (conversion always greater than 98 %). With that said, any residual amount is allowed to pass through the cells.

The stack electrical power output is calculated as:

$$P_e = i_{cell,2} A_{cell} V_{cell,2} N_{cell} \tag{3.3.2.7}$$

$V_{cell,2}$ is determined using the calibrated cell model of section 3.2:

$$V_{cell,2} = 0.75 - 1.8e^{-3}\left(i_{cell,2} - 77.6\right) + 8.3e^{-6}\left(T_{cell,2} - 1088\right)i_{cell,2} +$$

$$7.4e^{-2} ln\left(1.43\left(\frac{\bar{p}_{H2,2}}{\bar{p}_{H2O,2}}\right)\right) + 2.3e^{-2} ln\left(\frac{\bar{p}_{O2,2}}{0.21}\right) \tag{3.3.2.8}$$

To calculate the $\bar{p}_{H2}$, $\bar{p}_{H2O}$, and $\bar{p}_{O2}$ values, the inlet and outlet compositions of the cells are first imported into a spreadsheet. Within the spreadsheet, the inlet and outlet mole fractions of each species are arithmetically averaged and multiplied by 1.013 bar (1 atm) to yield the average partial pressures.

Another important dependent variable calculated by the process model is the steady-state hotbox temperature, $T_{cell,2}$. Because $T_{cell,2}$ is used in the reformer equilibrium calculation, the WGS correction calculation, and the cell voltage calculation, solving for it explicitly would have been cumbersome, so it was determined through iteration. As part of the iterative procedure, Bove *et al*. (2005) [75] suggest calculating an energy balance around to the hotbox boundary. The

Bove *et al*. [75] approach is followed here. The energy balance around the hotbox is:

$$\frac{dE}{dt} = \dot{H}_{reformer\ feed}\left(T_{reformer\ feed}\right) + \dot{H}_{cathode\ feed}\left(T_{cathode\ feed}\right) - \dot{H}_{anode\ exhaust}\left(T_{cell,2}\right) - \dot{H}_{cathode\ exhaust}\left(T_{cell,2}\right) - P_{e,gross}\left(T_{cell,2}\right) \quad (3.3.2.9)$$

where the "$\dot{H}$" terms are simply the enthalpy flow values (calculated by UniSim Design™ as stream properties). As a side note, the $\dot{H}$ and $P_{e,gross}$ terms are functions of temperature, pressure, composition, and flow rate, but appear as functions of temperature only for brevity. Referring back to expression 3.3.2.9, steady-state conditions are achieved when $dE/dt = 0$. In order to achieve these conditions, the "Stack Temp. Adjust" function (see figure. 3.4.1) is used to iterate the value of $T_{cell,2}$. When dE/dt = 0 ± 0.01 W, the iteration stops and the final $T_{cell,2}$ value is taken as the solved hotbox temperature.

As mentioned in section 3.3.1, it is assumed that the system exhaust can provide a useful thermal power output until it is cooled to 100°C. Therefore, the thermal power output, P_{th}, is calculated as the heat liberated by cooling the system exhaust stream from its model-calculated temperature down to 100°C. The calculation carried out by the "Thermal Power Calculator" (see figure 3.4.1) according to expression 3.3.2.10:

$$P_{th} = \dot{H}_{system\ exhaust} - \dot{H}_{vented\ exhaust}(set\ to\ 100°C) \quad (3.3.2.10)$$

where $\dot{H}_{system\ exhaust}$ is the enthalpy flow rate of the system exhaust stream and $\dot{H}_{vented\ exhaust}$ is the enthalpy flow rate of the exhaust stream cooled to 100°C.

The calculations of the gross electrical and CHP efficiencies are based on the LHV of the biogas feed:

$$\eta_e = \frac{P_e}{\dot{n}_{biogas} LHV_{biogas}} \quad (3.3.2.11)$$

$$n_{CHP} = \frac{P_e + P_{th}}{\dot{n}_{biogas} LHV_{biogas}} \quad (3.3.2.12)$$

To evaluate the possibility of carbon formation in the pre-reformer and reformer, the principal of equilibrated gas is applied and programmed into the model. The principal of equilibrated gas posits that solid carbon can form on a surface (*i.e.* catalyst surface) if the overhead gas is calculated to precipitate solid carbon at equilibrium [70]. In the current case, for both the pre-reformer and reformer, the calculation is carried out by evaluating the "carbon activities" for each of the Bouduoard (BD), methane decomposition (MD), and carbon monoxide reduction (COR) reactions at the final equilibrium compositions. For the three reactions, the carbon activities are:

$$\alpha_{BD} = \left(\frac{Q_{BD}}{K_{eq,BD}}\right) \quad (3.3.2.13)$$

$$\alpha_{MD} = \left(\frac{Q_{MD}}{K_{eq,MD}}\right) \quad (3.3.2.14)$$

$$\alpha_{COR} = \left(\frac{Q_{COR}}{K_{eq,COR}}\right) \quad (3.3.2.15)$$

where, for each reaction, the Q values are the reaction quotients determined from the reactor equilibrium composition:

$$Q_{BD} = \frac{p_{CO2}}{p_{CO}^2} \quad (3.3.2.16)$$

$$Q_{MD} = \frac{p_{H2}^2}{p_{CH4}} \quad (3.3.2.17)$$

$$Q_{COR} = \frac{p_{H2O}}{p_{CO} p_{H2}} \quad (3.3.2.18)$$

and the K_{eq} values are the equilibrium constants determined at reactor temperature (T):

$$K_{eq,BD} = \exp\left(\frac{-\Delta G^0_{R,T,BD}}{RT}\right) \quad (3.3.2.19)$$

$$K_{eq,MD} = \exp\left(\frac{-\Delta G^0_{R,T,MD}}{RT}\right) \quad (3.3.2.20)$$

$$K_{eq,COR} = \exp\left(\frac{-\Delta G^0_{R,T,COR}}{RT}\right) \quad (3.3.2.21)$$

Carbon formation is considered thermodynamically possible if any of the carbon activities is less than 1.

For the determination of standard Gibbs free energies of reaction ($\Delta G^0_{R,T,BD}$, $\Delta G^0_{R,T,MD}$, and $\Delta G^0_{R,T,COR}$), graphite was assumed as the carbon species. Graphite approximates the "whisker carbon" species commonly found on spent catalysts [70].

It should be noted that this method only provides an estimate for possible carbon formation based on bulk gas composition. In reality, the local environment of the catalyst bed and kinetics will dictate carbon formation [70], meaning more detailed reactor modeling or experimental work will be required to fully establish the carbon-free operating window.

3.3.3. Process Model Reference Conditions

Some of the independent and dependent variables of the model were previously discussed in section 3.3.2. In this section, they are revisited and more explicitly stated. In addition, a reference design case is defined and discussed. The sensitivity analyses of section 4.2 are oriented around these reference conditions.

Tables 3.3.3.1 and 3.3.3.2 list the main independent and dependent variables along with their corresponding reference condition values.

Table 3.3.3.1. Reference condition input values for the process model. All independent variables are freely adjustable by the user. (*) marks the input variables adjusted in the analyses of section 4.2.

Independent (input) variables	Value(s)
Ambient temperature (°C)	25
Ambient pressure (bar)	1.013
Biogas composition* (vol. %)	63 % CH_4, 37 % CO_2
Air composition (vol. %)	79 % N_2, 21 % O_2
System pressure (bar)	1.013
Active cell surface area, A_{cell} (cm^2)	200
Average cell current density, i_{cell} ($mA \cdot cm^{-2}$)	75
Number of cells, N_{cell}	192
Fuel utilization*, u_f (%)	80
Oxidant utilization*, u_{ox} (%)	20
Steam-to-carbon ratio, $r_{H2O/C}$ (system entrance)*	2.8
Activated carbon bed temperature (°C)	25
Activated alumina bed temperature (°C)	400
Superheated steam temperature (°C)	200
Pre-reformer feed temperature (°C)	550
Hotbox feed temperature, $T_{reformer\ feed}$ (°C)	800
Cathode feed temperature, $T_{cathode\ feed}$ (°C)	650
Vented exhaust temperature (°C)	100
Steam generator (HX 1) U value ($W \cdot m^{-2} \cdot °C^{-1}$)	25
Biogas pre-heater (HX 2) U value ($W \cdot m^{-2} \cdot °C^{-1}$)	20
Air pre-heater 1 (HX 3) U value ($W \cdot m^{-2} \cdot °C^{-1}$)	20
Pre-reformer pre-heater (HX 4) U value ($W \cdot m^{-2} \cdot °C^{-1}$)	20
Fuel processor pre-heater (HX 5) U value ($W \cdot m^{-2} \cdot °C^{-1}$)	20
Air pre-heater 2 (HX 6) U value ($W \cdot m^{-2} \cdot °C^{-1}$)	20

Table 3.3.3.2. Various output values calculated by the process model at reference conditions.

Dependent (Output) Variables	Value(s)
Cell voltage, V_{cell} (V)	0.71
Gross electrical power output, P_e (W)	2048
Thermal power output, P_{th} (W)	308
Gross electrical efficiency, η_e (LHV basis) (%)	54.7
CHP efficiency, η_{CHP} (LHV basis) (%)	62.9
Hotbox temperature, T_{cell} (cells and reformer) (°C)	808
Afterburner temperature (°C)	937
System exhaust temperature, $T_{system\ exhaust}$ (°C)	149
Biogas feed rate, $\dot{n}_{biogas}$ (SLPM)	10.5
Air feed rate, $\dot{n}_{air}$ (SLPM)	252
Water feed rate, $\dot{n}_{water}$ ($mL \cdot min^{-1}$)	22.3
Steam generator (HX 1) minimum approach temp. (°C)	109
Biogas pre-heater (HX 2) minimum approach temp. (°C)	200
Air pre-heater 1 (HX 3) minimum approach temp. (°C)	164
Pre-reformer pre-heater (HX 4) minimum approach temp. (°C)	259
Reformer pre-heater (HX 5) minimum approach temp. (°C)	81.3
Air pre-heater 2 (HX 6) minimum approach temp. (°C)	287
Steam generator (HX 1) area (m^2)	0.360
Biogas pre-heater (HX 2) area (m^2)	0.018
Air pre-heater 1 (HX 3) area (m^2)	0.723
Pre-reformer pre-heater (HX 4) area (m^2)	0.0456
Reformer pre-heater (HX 5) area (m^2)	0.129
Air pre-heater 2 (HX 6) area (m^2)	0.070

Referring to the inputs (table 3.3.3.1), the biogas composition is based on the most recent measurements made at the Ravensview WWTP [76]. The chosen number of cells reflects the number of 8-celled demonstration stacks (see section 3.1) required to provide a gross electrical power output of 2 kW_e (approximate). A fuel utilization of 80 % is commonly-used throughout the literature as a base-case setting [3, 9, 13, 39]. This value ensures that a high amount of fuel is converted within the cells for electricity production, but also that enough is left over for production of the hot tail gas stream. Fuel utilization values (based on a single pass through the cell) rarely exceed 85 %. If the fuel utilization is additionally increased, there will come a point whereby the bulk fuel concentration near the exit

of the anode is too low to provide enough driving force to overcome the mass transport limitation of the porous material. This results in the heavy depletion of fuel near many of the catalytic sites and precipitous drop in cell voltage [25]. Moreover, in this operation, the anode material may be oxidized by water or oxygen in the local region where the fuel is heavily depleted [77].

Less standard are values for oxidant utilization, which generally vary between 10 and 25 %. Peters *et al.* (2013) [35] note that an upper limit of 50 % is generally used to ensure adequate cell performance. The value of 20 % listed in table 3.3.2.1 is in range of common values and ensured the hotbox temperature was approximately mid range of what was recorded during the cell experiments (see sections 3.1 and 3.2).

The pre-reforming of natural gas (which has a higher loading of non-polar higher hydrocarbons than biogas) can reportedly be carried out at steam-to-carbon ratios as low as 0.3 [40]. For steam reforming, a steam-to-carbon ratio of 2.5 is on the lower end of what is commonly used for the industrial steam reforming of CH_4 [25, 69, 78]. The steam-to-carbon ratio of 2.8 listed in table 3.3.3.1 (for the system entrance) is above both of these lower limits. However, it should be noted that some H_2O is initially consumed in the pre-reformer *(i.e.*, approx. 22 % CH_4 is converted) such that the steam-to-carbon ratio of the downstream reformer feed is reduced to about 2.5.

The current density was set high enough to provide a reasonable electrical power output from the cells, but not high enough that the cell voltage was below the minimum recommended value of 0.62 V. Low cell voltage is a proxy for cell degradation [62].

Activated carbon beds are usually operated at ambient conditions [29]. Therefore, the temperature of the activated carbon bed was set to 25°C and was not influenced by the heat exchanger adjustments.

The activated alumina bed was set to 400°C based on the work of Finocchio *et al*. [31], who found that, in the range of 250 to 400°C, adsorbent capacity is enhanced for higher bed temperatures.

The pre-reformer feed temperature was set to 550°C, which is on the higher end of their typical operating range [40]. This was to compensate for the 154°C temperature drop which was found to occur as a result of the 22 % conversion of CH_4 under the equilibrium assumption.

The hotbox feed is pre-heated (800°C) to the approximate hotbox temperature (808°C) in order to minimize the temperature gradients within the hotbox. In a modeling study, Dokmaingam *et al*. (2010) [71] showed that the maximum thermal gradient of a TSOFC can be kept to a safe value (*i.e.*, below 10 $K \cdot cm^{-1}$ [71]) if the IIR of biogas is carried out in the direction counter to the fuel and air flows. In their study, the reformer feed was fed at the approximate average temperature of the cell and reformer (900°C) [71].

The cathode air feed temperature was set to 650°C assuming that an additional 150°C (approx.) of pre-heating was possible within the portion of the air feed tube extending into the bottom of the cell. Suwanwarangkul *et al*. (2007) [79] demonstrated that up to 300°C of air pre-heating is possible within this portion of the air feed tube.

Although the reported performance in table 3.3.3.2 does not include pumping losses, the electrical performance is considered to be competitive with reciprocating engine and microturbine technologies, which are typically between 30 and 40 % electrically efficient [12]. Van herle *et al*. (2004) [39] estimate that pumping losses can reduce the gross electrical efficiency by as little as 1.2 percentage points for a non-pressurized biogas-fed SOFC systems.

Importantly, the afterburner temperature is lower than 1000°C and the ΔT_{min} values of all heat exchangers are greater than 50°C. SOFC systems that are considered economically feasible abide by these design constraints [35].

4. RESULTS AND DISCUSSION

The general purpose of section 4 is to demonstrate the process model as a design tool capable of estimating system performance and limitations relative to design conditions. However, first, in section 4.1, the general applicability of the empirical cell model is demonstrated through its calibration to a surrogate data set found in the literature. In section 4.2, the effect of biogas composition, steam-to-carbon ratio, oxidant utilization, and fuel utilization on pilot plant performance is explored. In section 4.2.5, a two-variable sensitivity analysis is performed relative to fuel and oxidant utilization, and conditions for maximum system performance on Ravensview biogas are estimated.

4.1. Case Study: Cell Model Calibration to Surrogate Performance Data

In order to demonstrate the general applicability of the empirical cell model, it was fit to a surrogate data set extracted from Sasaki *et al*. (2002) [80] using the DigitiseImage™ software. DigitiseImage™ allows the user to define a co-ordinate system along the borders of an image and record the locations of points within image relative to the co-ordinate system. The user can then command the software to generate a plot of the selected points in Excel™.

Similar to the current work, Sasaki *et al*. [80] used TSOFCs manufactured by TOTO Ltd. and collected their data largely in the ohmic region of the polarization curve. Every possible data point was extracted from their work whereby argon was used as anode diluent (it was proven that use of Ar and N_2 diluent gases yielded similar performances). A total of 95 data points were extracted and a summary of their experimental conditions is provided in table 4.1.1.

A beneficial quality of the Sasaki *et al*. [80] work was that the data was collected to generate polarization curves. This allowed for a more qualitative assessment of the calibrated cell model because it could be plotted against the polarization curve data.

Table 4.1.1. Summary of the experimental conditions of the data extracted from Sasaki *et al*. (2002) [80]. (*) the cell pressure was not provided; however, pressurized conditions were not mentioned. Therefore, it was assumed that the cell was operated at approximately atmospheric pressure.

Experimental Condition	Value(s)	Number of Data Points at Condition
Cell temp. 1 (T1) (°C)	900	40
Cell temp. 2 (T2) (°C)	1000	55
Cell pressure* (bar)	1.013	95
Anode feed comp. 1 (vol. %)	21 H_2, 0 CO, 1 H_2O, 78 Ar	19 (8 at T1, 11 at T2)
Anode feed comp. 2 (vol. %)	15 H_2, 6 CO, 1 H_2O, 78 Ar	19 (8 at T1, 11 at T2)
Anode feed comp. 3 (vol. %)	10 H_2, 10 CO, 1 H_2O, 78 Ar	19 (8 at T1, 11 at T2)
Anode feed comp. 4 (vol. %)	6 H_2, 15 CO, 1 H_2O, 78 Ar	19 (8 at T1, 11 at T2)
Anode feed comp. 5 (vol. %)	0 H_2, 21 CO, 1 H_2O, 78 Ar	19 (8 at T1, 11 at T2)
Cathode feed comp. (vol. %)	21 O_2, 79 N_2	95
Anode feed rate ($L \cdot min^{-1}$)	1.92	95
Cathode feed rate ($L \cdot min^{-1}$)	2.0	95

Before the final calibration, a series of trial-and-error calibrations were performed using the same procedure outlined in section 3.2. During these calibrations it was discovered that the 900°C and 1000°C polarization curves crossed in the region between 80 and 120 $mA \cdot cm^{-2}$. More specifically, for current densities less than 80 $mA \cdot cm^{-2}$ the cell voltage decreases with increasing temperature while for current densities greater than 120 $mA \cdot cm^{-2}$ the cell voltage increases with increasing temperature. This crossing behavior was discussed in section 2.1 (see figure 2.1.2), but in the current case, it confounded the regression because the assumption that cell voltage always increases with temperature is incorporated into the structure of the $\Delta V_{cell,T}$ correlation (expression 3.2.3). In light of this, all data points with current densities less than 120 $mA \cdot cm^{-2}$ (*i.e.*, all those with current densities of 0, 40, and 80 $mA \cdot cm^{-2}$) were rejected to eliminate the crossing behavior of the curves. In total, 30 of the original 95 data points were rejected. As a side note, this crossing behavior was not evident in the data set collected in the current work (see Appendix D).

The final cell model calibration is plotted against the raw Sasaki *et al*. [80] data in figure 4.1.1. For visual clarity, only four of the Sasaki *et al*. [80] polarization curves were plotted in the figure. The figure shows that the calibrated cell model can reproduce the cell performance with reasonable accuracy. It should be noted, however, that the model does not reproduce the slight curvature of the polarization curves. This curvature is most likely caused by mass transport

resistance in the cells (concentration polarization) which is not accounted for in the mathematical structure of the model. As long as the cell model is used within the current density range of the ohmic region this error should be minimal, as observed here.

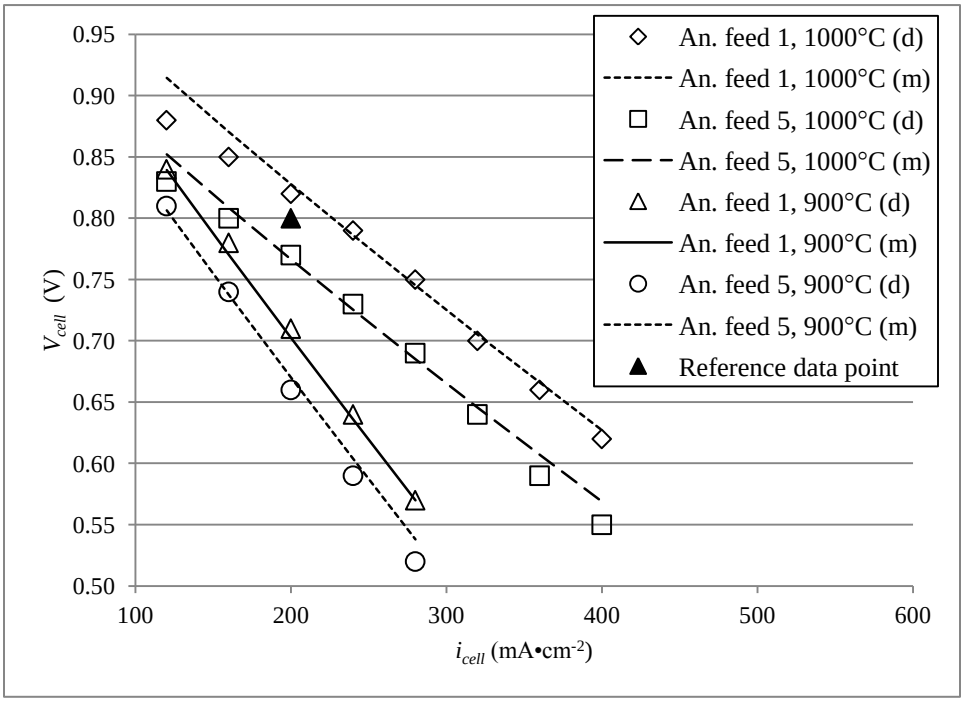

Figure 4.1.1. Results of the cell model calibration to data extracted from Sasaki *et al.* (2002) [80]. In the legend, "d" indicates a raw data point and "m" indicates values predicted by the calibrated model. The data point used for the model reference point is represented by the filled-in triangle.

The C_i, C_T, C_a, and C_c values determined from the Sasaki *et al.* [80] calibration are shown in table 4.1.1. Also shown are the calibration values determined from the data in this work and the values put forth by EG&G Services, Inc. [25].

Table 4.1.2. Values of C_i, C_T, C_a, and C_c after cell model calibration to the data in this work, the data Sasaki *et al.* (2002) [80], and the values recommended for use by EG&G Services, Inc. (2004) [25].

Source	C_i x 10^3 ($V \cdot cm^2 \cdot mA^{-1}$)	C_T x 10^6 ($V \cdot K^{-1} \cdot mA^{-1}$)	C_a x 10^2 (V)	C_c x 10^2 (V)
CanSES data (current work)	-1.8	8.3	7.4	2.3
EG&G Services, Inc. [25]	-0.73	40	7.5	4.0
Sasaki *et al*. [79]	-0.74	6.3	12.1	2.7

Due to the complex environment within the cells (*i.e.*, existence of thermal gradients and concentration gradients) and the highly empirical nature of the cell model, only a qualitative comparison should be made between the values in table 4.1.2. Also, consideration should be given to the fact that the values put forth by EG&G Services, Inc. [25] were roughly estimated by hand calculation and not regressed to the data they studied.

The values for C_i appear to be in line with the expected trend. Expanding, the $\Delta V_{cell,i}$ correlation can be thought of as a single polarization curve (line) of slope C_i that is a function of current density only. Furthermore, because it is only a single curve, it is unique to the span of data over which it is regressed. Therefore, it is expected that C_i have larger negative values for data collected at lower temperatures because, at lower temperatures, the cell resistance is greater and the voltage drops off quicker with current density. The C_i value determined from the Sasaki *et al*. [80] data was for data in the 900 to 1000°C range and the value provided by EG&G Services, Inc. [25] was for 1000°C operation; as expected, both of these values are less negative than the value determined from experimental component of this work, which was collected closer to 800°C.

The values for C_T are less well behaved. The expected trend is that C_T values be positive, but lower in magnitude for higher temperature data. This is because the cell conductivity follows an Arrhenius relationship with temperature which causes the magnitude of the voltage gain to decline with temperature. In fact, because of this Arrhenius relationship, EG&G Services, Inc. [25] suggest that C_T values are only valid over 100°C to 150°C temperature ranges. The expected trend for C_T values appears to hold between the Sasaki *et al*. [80] data and the data collected in the current work. However, the value taken from EG&G Services, Inc. [25], which is prescribed for the 800 – 900°C temperature range, appears to be an outlier. With that said, this is not entirely surprising given that EG&G Services, Inc. [25] value was estimated by hand. In addition, EG&G Services, Inc. [25] reportedly found C_T values to vary by almost an order of magnitude between published data sets involving common temperature ranges.

The C_a values appear to reasonably follow the expected trend. Expanding, the Nernst equation can be used to estimate C_a as $RT/2F$, which indicates that C_a should be greater for higher temperature data; this is approximately borne out between the Sasaki *et al*. [80] data and the data collected in this work. However, the C_a value provided by EG&G Services, Inc. [25], which is for 1000°C operation, might be expected to have a value closer to the value derived from the Sasaki *et al*. [80] data. Again, consideration should be given to the way the EG&G Services, Inc. [25] was determined (hand calculation).

In closing, the values in table 4.1.2 appear to be reasonable and in general agreement. Where discrepancies exist, the values tend to deviate according to expected trends.

4.2. Pilot Plant Performance Study

The purpose of section 4.2 is to demonstrate how the calibrated process model can be used as a tool for predicting system performance and practical design limits. To this end, a series of sensitivity analyses are performed to study the effects of key design variables on performance.

For the sensitivity analyses, table 3.3.1 provided the basis for the settings of the independent variables and table 3.3.2 includes many of the values that were allowed to vary as dependent variables. System performance is reported in terms of electrical power output, thermal power output, electrical efficiency, and CHP efficiency, which are calculated according to expressions 3.3.2.7, 3.3.2.10, 3.3.2.11, and 3.3.2.12, respectively.

Many design variables were possible for consideration, but focus was narrowed to those that define the feed streams to the system; these variables are biogas composition, steam-to-carbon ratio, oxidant utilization, and fuel utilization.

The effect of biogas composition is studied in section 4.2.1. It is important to establish that the pilot plant can be operated over the range of possible compositions generated at WWTPs and how the system might perform at the different sites. In the current work, the sensitivity analysis for biogas composition covers the range of compositions put forth by Wheeldon *et al*. [3] for WWTPs in Ontario (58 to 70 % CH_4) and has been extended for theoretical purposes. In all remaining sections (4.2.2 through 4.2.5), the biogas feed composition is fixed to the Ravensview composition (reference condition, 63 % CH_4, 37 % CO_2) because Ravensview is the location of interest and its biogas composition appears to serve as a good average for WWTPs in general.

The effect of steam-to-carbon ratio is studied in section 4.2.2. The steam-to-carbon ratio controls the water feed rate to the system. From a performance perspective, water feed rate is an important consideration because steam generation is a significant thermal sink within the system and the water feed rate influences the gas composition within the cells. The pre-reforming of natural gas can be carried out at steam-to-carbon ratios as low as 0.3 [40]. For MSR, practical industrial experience dictates that the steam-to-carbon ratio should be upward of 2.5 to avoid catalyst deactivation [25, 78]. However, some researchers found that the steam-to-carbon ratio might be reduced in the case of biogas SR (to a value of almost 1) using commercial Ni-based MSR catalysts [81, 82]. In light of its possible range of values, it is worth exploring the effect of the steam-to-carbon ratio.

The effect of oxidant utilization is studied in section 4.2.3. At any given time, air is the bulk mass flowing through the system; therefore its flow rate and impact on the system performance is of considerable interest. In the current work, whereby the current density is held constant, the oxidant utilization controls the flow rate of air fed to and through the system.

In section 4.2.4, the effect of fuel utilization is studied. Paralleling the case for oxidant utilization and air, the fuel utilization controls the biogas feed rate; however, it also controls the split between how much fuel consumed in the cells for electrical power production and amount the consumed in the afterburner for tail gas generation; in light of this, the effect of fuel utilization on performance is of considerable interest.

Lastly, in section 4.2.5, the effect of both fuel and oxidant utilization are simultaneously studied in a two-variable sensitivity study at the reference-case steam-to-carbon ratio (2.8). Later in the section, the steam-to-carbon ratio is adjusted to provide a global estimate for maximum system performance on Ravensview biogas.

The following constraints were considered in order to place practical restrictions on the modeling analysis and keep the analysis within a realm of feasible design conditions:

Table 4.2.1. Constraints applied throughout the variable sweeps of section 4.2.

Constraint	Value
Afterburner temperature (°C)	≤ 1000
Heat exchanger minimum approach temperature, ΔT_{min} (°C)	≥ 50
Fuel utilization, u_f (%)	≤ 85
Cell voltage, V_{cell} (V)	≥ 0.62
Carbon accumulation	< 0
System exhaust temperature, $T_{system\ exhaust}$ (°C)	≥ 100
Hotbox/average cell temperature, T_{cell} (°C)	$730 \leq T_{cell} \leq 880$

The afterburner constraint has been considered because it is generally accepted that units required to operate in excess of 1000°C are not economical in SOFC systems [35]. A similar argument holds for heat exchangers; it is generally accepted that units designed to achieve minimum approach temperatures less than 50°C are uneconomical [35].

The fuel utilization was manually restricted to be less than or equal to 85 % because of the argument previously made in section 3.3.3; namely that mass transfer limitations (concentration polarization) become significant past this value, causing a precipitous drop in cell performance [25]. In addition, the empirical cell model was not developed to predict performance in the region of high concentration polarization.

The cell voltage is calculated according to expression 3.3.2.8. The minimum value listed in table 4.2.1 was recommended by TOTO Ltd. because there is a significant risk of cell degradation if the cell voltage drops below 0.62 V [62].

The analysis was restricted to regions in which carbon accumulation in the pre-reformer and reformer is not likely. The calculations estimating carbon formation, which are based on thermodynamic arguments, are described in section 3.3.2, but are briefly revisited here. In either reactor, if any of the carbon activities for the Bouduoard (BD), methane decomposition (MD), or carbon monoxide reduction (COR) reactions are calculated to be less than 1 carbon formation is considered to be thermodynamically possible. Although it is common to use thermodynamic arguments to identify regions of possible carbon formation, more detailed modeling or experimental work is usually required to fully define the carbon-free operating window to account for local conditions within the catalyst bed and reaction kinetics [70].

The remaining constraints do not necessarily limit the viability of the system, but are unique to the current modeling exercise. For example, the possibility of condensing-out and recovering the water content of the system

exhaust stream was not considered in this work; therefore, the modeling analysis has been restricted to regions in which the system exhaust stream is above its approximate dew point (taken as 100°C). Additionally, in general, it is possible for SOFCs to operate between 600 and 1000°C [25]. However, in the current case, the analysis has been restricted to regions in which the average cell temperature is between 730 and 880°C. This is because, as discussed in section 4.1, the $\Delta V_{cell,T}$ correlation is only a linear approximation to how the cell voltage varies with temperature; in reality, the voltage response is not linear because the cell conductivity follows an Arrhenius relationship with temperature [25]. In light of this, EG&G Services, Inc. [25] suggest that the correlation is only applicable over ranges of approximately 100°C to 150°C. The 730 to 880°C temperature range is the 150°C range surrounding the average cell temperature of the experimentally-collected data (805°C).

It should be noted that the process model can be operated beyond the boundaries listed in table 4.2.1, but, in the current work, data collection was manually ceased when one of the constraints were reached. With that said, some of these constraints are violated in section 4.2.5 in order to maintain the square base of the three-dimensional plots; however, the regions where this occurs are divulged to the reader.

4.2.1. Effect of Biogas Composition on System Performance

The effect of biogas composition is plotted in figure 4.2.1.1. The sweep range extends from 47 to 100 CH_4 content with the balance being CO_2 only. As shown, all performance metrics are improved as the biogas CH_4 content increases; most pronounced are the rise in thermal power output and CHP efficiency.

The only feed streams influenced by the increase in CH_4 content are the biogas and water feeds. To begin, $\dot{n}_{CH4,biogas}$ is constant according to the condition identified in section 3.3.2:

$$\dot{n}_{CH4,biogas} \approx \frac{1}{4}(\dot{n}_{H2} + \dot{n}_{CO})_{fuel} \approx \frac{1}{4}\left(\frac{i_{cell,2}A_{cell}N_{cell}}{2Fu_f}\right) \quad (3.3.2.4)$$

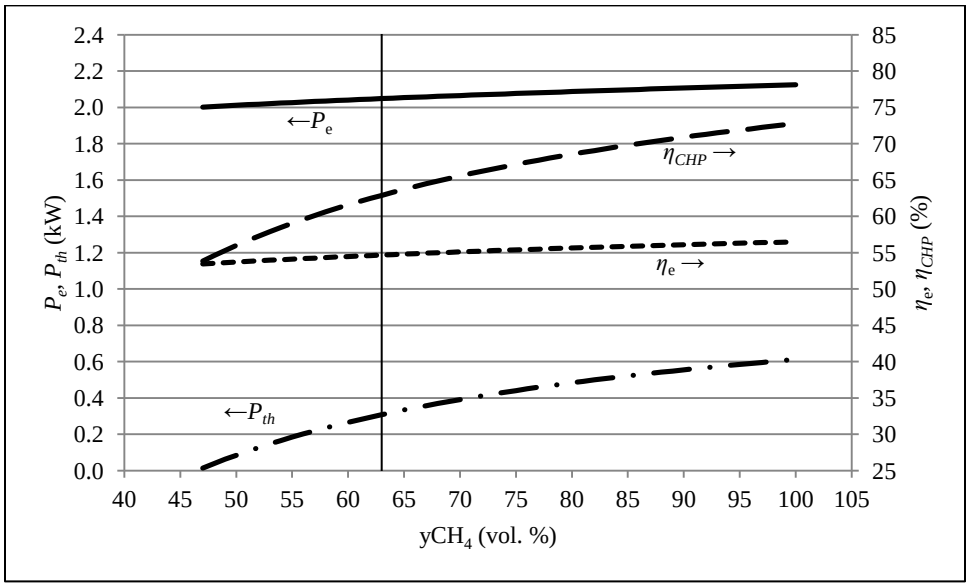

Figure 4.2.1.1. System performance as a function of biogas CH_4 content. The vertical black line indicates the reference conditions (Ravensview biogas composition).

None of the variables in the right-most bracketed term are varied, so $\dot{n}_{CH4,biogas}$ is unchanged. In order to carry out the composition sweep (increase the CH_4 content) and keep the $\dot{n}_{CH4,biogas}$ constant, the model lowers the co-feed rate of the CO_2 in the biogas. Therefore, the biogas feed rate is reduced in the process. By extension, the water feed rate is also reduced because it is tethered to the biogas flow via the steam-to-carbon ratio (2.8). Therefore, all mass flow rates on the anode-side are reduced leading to a decline in system exhaust flow.

The electrical power output rises because the reduction in water and CO_2 feed rate leads to an increase in H_2 concentration downstream in the cells. Expanding, according to expression 3.3.2.4 the molar flow rate of H_2 equivalents exiting the reformer is constant (4 times $\dot{n}_{CH4,biogas}$), so the declining water and CO_2 flows leads to a general rise in concentration of H_2 equivalents in the cells. Additionally, the molar feed rate of CO_2 decreases at a sharper rate than that of water so that a forward-shifting of the WGS toward H_2 production occurs in the reformer and cells.

Interestingly, the hotbox temperature declines over the sweep range (from 820 to 789°C), which opposes the rise in electrical power output through a reduction in cell conductivity. The reduction in hotbox temperature is influenced heavily by the behavior of the pre-reformer. For example, unlike the reformer, only a fraction of the CH_4 is ever converted in the pre-reformer at equilibrium.

The reduction in CO_2 and water feed rates causes the conversion of CH_4 in the pre-reformer to drop, meaning a greater proportion of it is converted downstream in the reformer (always full conversion at the reformer exhaust). Because SR and DR are endothermic, the heat sink within the hotbox increases causing it to cool. However, despite the decline in hotbox temperature, the effect of rising H_2 concentration within the cells dominates the reduction in cell conductivity. For example, over the sweep range, $\Delta V_{cell,T}$ decreases by 18.8 mV, but $\Delta V_{cell,a}$ increases by 61.4 mV resulting in a total rise of 43 mV in the cell voltage over the sweep range.

Considering that the feed rate of chemical energy to the system remains constant (*i.e.*, $\dot{n}_{CH4,biogas}$ is constant), the enhancement in gross electrical efficiency follows directly from the rise in gross electrical power output.

The rise in thermal power output is now addressed. As mentioned above, the hotbox temperature declines with increasing CH_4 content and this encourages the observed decline in downstream afterburner temperature. However, this temperature decline is not propagated to end of the tail gas line. In fact, the temperature of the system exhaust stream actually rises by 99°C over the sweep range. This occurs because of how dramatically the pre-heating duty falls as a result of the declining biogas and water feed rates. Therefore, the rise in the system exhaust temperature is what ultimately leads to the rise in thermal power output.

The increase in CHP efficiency results directly from the concurrent rise in both electrical and thermal power output.

The range of the analysis is now addressed. On the high end of the sweep range, no constraints were encountered and it was possible to bring the CH_4 composition up to 100 %. This is an interesting result because it suggests that the system could possibly be packaged to run on pure CH_4 or even natural gas. However, when the CH_4 content drops to below 47 % the biogas and water flow rates are large enough that the sensible heat drawn from the tail gas reduces the system exhaust temperature to below 100°C. Therefore, the 6th constraint listed in table 4.2.1 limited the current analysis to CH_4 contents above 47 %. In any event, the results show that the system can be designed to operate over the full range of biogas compositions produced at WWTPs in Ontario (58 to 70 dry %) [3], and that the feasible design range is at least from 47 to 100 % CH_4 content.

In summary, all performance metrics are enhanced for richer biogases; however the largest gains are expected in terms of thermal power output and CHP efficiency, as electrical performance is only modestly affected. The slight enhancement of electrical performance occurs largely from an increase in H_2 concentration within the cells. Thermal power output is enhanced because the declining biogas and water feed rates lower the amount of sensible heat drawn from the tail gas stream, yielding a rise in system exhaust temperature. The pilot plant is feasible over the full range of expected biogas compositions produced at

Ontario WWTPs, and the feasible range extends at least from 47 to 100 % CH_4 content. At the low bound, the system exhaust temperature drops below 100°C; on the high end, no constraint was reached suggesting that the system can be configured for operation on pure CH_4 or perhaps even natural gas.

4.2.2. Effect of Steam-to-Carbon Ratio on System Performance

The effect of steam-to-carbon ratio for the system operating on Ravensview biogas is shown in figure 4.2.2.1. The sweep range extends from 1.6 to 3.7 steam-to-carbon ratio. As shown, all performance metrics are adversely affected as the steam-to-carbon ratio is increased, particularly thermal power output and CHP efficiency.

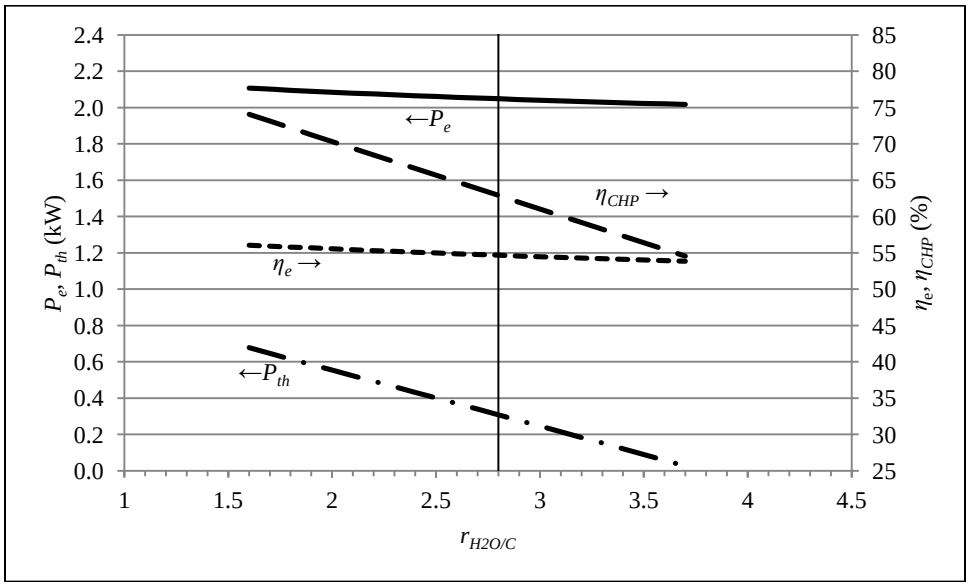

Figure 4.2.2.1. System performance as a function of steam-to-carbon ratio. The vertical black line indicates the reference conditions ($r_{H2O/C}$ of 2.8).

The only feed stream affected by the steam-to-carbon ratio is the water feed. Expanding, similar to the previous section, $\dot{n}_{CH4,biogas}$ is constant because all

variables in the far-right bracketed term in expression 3.3.2.4 are unchanged. By extension, the biogas feed rate is constant because the CO_2 content is unchanged. Therefore, increasing the steam-to-carbon ratio causes water feed rate to rise relative to the constant biogas feed. Ultimately, the exhaust flow rate is increased by the rise in water feed through the system.

The fall in electrical power output is ultimately caused by the dilution of H_2 in the reformer and cells by steam, which reduces the cell voltage.

The cell voltage declines despite a 28°C rise in hotbox temperature over the sweep range (from 789 to 818°C). Contrasting the case of increasing CH_4 content (see section 4.2.1), the water feed rate is increasing here as the steam-to-carbon ratio is swept forward (increased). As a result, the amount of CH_4 ($\dot{n}_{CH4,biogas}$) converted in the pre-reformer is increased, which diminishes the reforming heat sink downstream in the hotbox. Overall, the $\Delta V_{cell,T}$ correlation increases by 18 mV, but the $\Delta V_{cell,a}$ drops 49 mV leading to a total drop of 32 mV in the cell voltage over the sweep range.

Given the constant biogas fed rate ($\dot{n}_{CH4,biogas}$), the decline in gross electrical efficiency follows directly from the decline in electrical power output.

Similar to the case of varying biogas composition (see section 4.2.1), the thermal power output is heavily influenced by the pre-heating demand put on the tail gas stream. Expanding, the afterburner temperature rises in response to the rise in hotbox temperature, but the increase in sensible heat drawn for steam generation/superheating is significant enough to cause a decline in system exhaust temperature. Referring back to figure 4.2.2.1, the observed effect is a drastic reduction in thermal power output.

The decline in CHP efficiency is a consequence of the concurrent decline in both electrical and thermal power outputs. It can be said that adding water simply causes a greater proportion of the chemical energy of the fuel (CH_4) to be carried away in the vented exhaust as water vapour.

Addressing the sweep range of the analysis, carbon formation by the COR reaction is predicted in the pre-reformer for steam-to-carbon ratios lower than 1.6. At steam-to-carbon ratios greater than 3.7, the pre-heating demand on the tail gas stream becomes excessive and the system exhaust temperature drops below 100°C. Therefore, the feasible range for steam-to-carbon ratio extends from 1.6 to 3.7 if the system exhaust stream is to be above 100°C for the avoidance of condensation.

In summary, all performance metrics are adversely affected by an increase in steam-to-carbon ratio, particularly the thermal power output and CHP efficiency. The reduction in electrical performance results largely from the dilution of H_2 by steam in the reformer and cells. The drop in thermal power is a consequence of the increase in sensible heat drawn from the tail gas stream for steam generation/superheating, which significantly reduces the system exhaust temperature.

For the Ravensview WWTP, the feasible range for steam-to-carbon ratio extends from 1.6 to 3.7: at the low bound, carbon formation is predicted in the pre-reformer; at the high bound, the system exhaust stream drops to below 100°C.

4.2.3. Effect of Oxidant Utilization on System Performance

The effect of oxidant utilization for the system operating on Ravensview biogas is shown in figure 4.2.3.1. The sweep range extends from 17.5 to 26.5 %. As shown, all performance metrics are enhanced as oxidant utilization is increased.

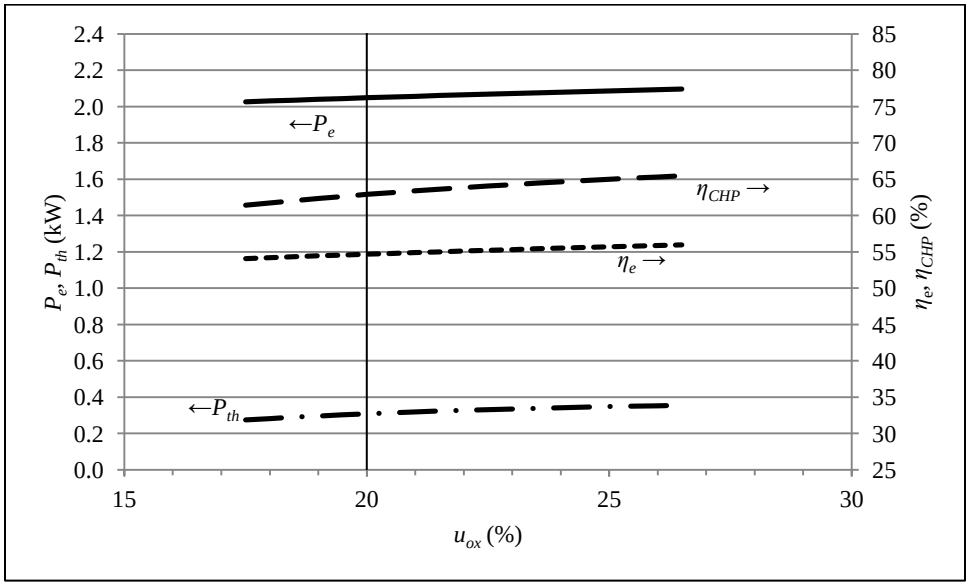

Figure 4.2.3.1. System performance as a function of oxidant utilization. The vertical black line indicates the reference conditions (u_{ox} of 20 %).

Increasing the oxidant utilization reduces the air feed rate; no other feed stream is affected. The biogas and water feed rates are unchanged because the variables in expression 3.3.2.4, biogas composition and steam-to-carbon ratio are all unchanged. Ultimately, the exhaust flow is reduced by the decline in air feed rate.

The electrical power output increases primarily through an enhancement of the cell conductivity. Expanding, increasing the oxidant utilization reduces the amount of air fed to the hotbox[3] at 650°C from HX 6. In turn, this diminishes the heat sink within the hotbox because there is less cooling air to absorb the heat generated by the exothermic cell reactions. As a result, the hotbox temperature rises (from 794 to 838°C over the sweep range), which leads to the enhancement in cell conductivity and voltage. As a side note, the reformer, which is also housed within the hotbox, has little influence because the CH_4 conversions in both the pre-reformer and reformer were unchanged throughout this analysis *(i.e.* the reformer duty is largely invariant).

With that said, there were two effects which tend to oppose the rise in electrical power output and cell voltage as oxidant utilization is increased. First, the WGS reaction, being exothermic, shifts backward and consumes H_2 in the cells as the hotbox temperature rises. Second, the concentration of O_2 in the cathodes decreases as a greater proportion of it is electrochemically utilized from the air stream. Overall, $\Delta V_{cell,a}$ and $\Delta V_{cell,c}$ drop by 2 and 1 mV, respectively, but $\Delta V_{cell,T}$ increases by 27 mV leading to a total rise of 24 mV in cell voltage over the sweep range.

Given the constant biogas feed rate, the rise in electrical efficiency follows directly from the rise in electrical power output.

Thermal power output is enhanced because, as the air flow through the system is lowered, there is progressively less mass to quench the exothermic processes occurring in the hotbox and afterburner; this leads to a rise in system exhaust temperature and the enhancement of the thermal power output. With the biogas feed rate unchanged, the rise in CHP efficiency results directly from the concurrent rise in both electrical and thermal power output.

As mentioned above, as the oxidant utilization is increased, the convective cooling effect by air decreases; as a result, the afterburner temperature exceeds 1000°C upward of 26.5 %. Conversely, reducing the oxidant utilization increases the convective cooling. Due to the significant cooling of the tail gas stream, the minimum approach temperature constraint for HX 5 is violated below 17.5 % utilization. For the heat exchanger, the violation occurs between the hot-side inlet (tail gas, which lowers to 850°C), and the cold-side outlet (reformer feed, which is held at 800°C). Noting these constraint violations, the feasible range for oxidant utilization extends from 17.5 to 26.5 %.

In summary, all performance metrics are enhanced with increasing oxidant utilization because the reduction in air feed lowers the convective cooling of the system. As a result, the hotbox, afterburner, and system exhaust temperatures all rise. The feasible range for oxidant utilization on Ravensview biogas extends from 17.5 to 26.5 %: at the low bound, the minimum approach

[3] Recall that the hotbox houses the cells and reformer and is assumed to operate isothermally.

temperature constraint is violated for HX 5; at the high bound, the afterburner temperature exceeds 1000°C.

4.2.4. Effect of Fuel Utilization on System Performance

The effect of fuel utilization for the system operating on Ravensview biogas is shown in figure 4.2.4.1. The sweep extends from 71 % to 85 %. As shown, the performance behavior is more complicated than that of the previous cases. For example, as fuel utilization is increased, the gross electrical efficiency increases while the CHP efficiency and thermal power output decrease. The electrical power output is largely unaffected.

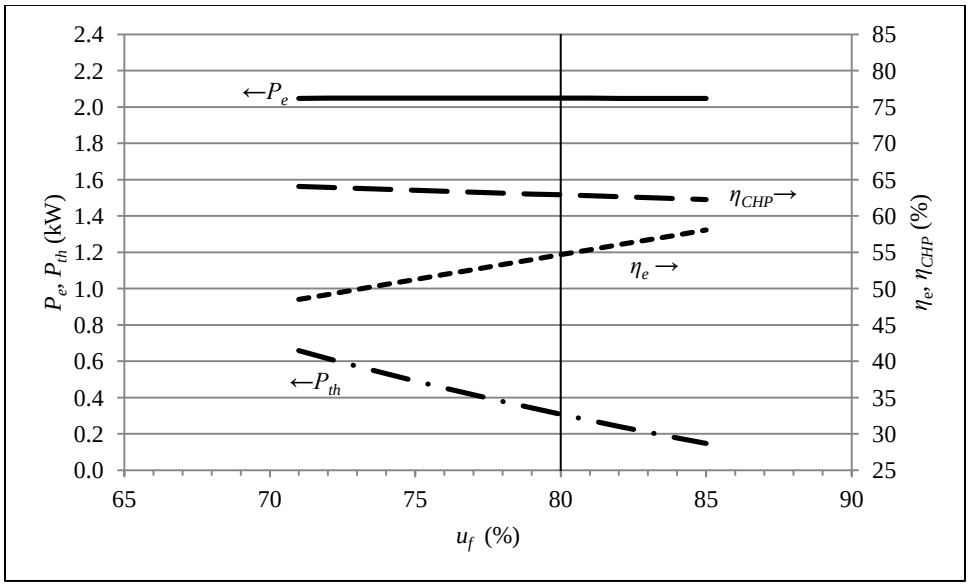

Figure 4.2.4.1. System performance as a function of fuel utilization. The vertical black line indicates the reference conditions (u_f of 80 %).

The biogas and water feed rates are both decreased by increasing the fuel utilization. Expanding, referring back to expression 3.3.2.4, increasing the fuel utilization decreases the molar flow of CH_4 required by the system ($\dot{n}_{CH4,biogas}$). By

extension, the biogas and water feed rate are reduced because the biogas composition and steam-to-carbon ratio are fixed. Ultimately, the exhaust flow rate is reduced as well.

The electrical power output appears relatively constant because of two competing effects acting on the cell voltage: a rise in hotbox temperature balanced by a concurrent decline in H_2 concentration.

The hotbox temperature rises primarily because the heat sink within the hotbox is diminished relative to the constant extent of electrochemical combustion. More specifically, the decline in biogas feed rate ultimately leads to a reduction in CH_4 being processed in the reformer, but the heat generated by the electrochemical reactions is constant according to the current density setting (75 $mA \cdot cm^{-2}$).

The decline in H_2 concentration occurs because the electrochemical consumption rate is constant but the amount of H_2 equivalents passing through the cells decreases. Within the cells, the WGS reaction shifts forward (re-equilibrates) to replenish some of the consumed H_2, but it's not enough to fully counter the amount electrochemically-consumed. Over the sweep range, $\Delta V_{cell,T}$ increases by 13 mV, but $\Delta V_{cell,a}$ drops by 13 mV. As a result, the net change in cell voltage is close to 0 mV.

The electrical efficiency increases with fuel utilization because the electrical power output remains fairly constant relative to the declining biogas feed rate. Put another way, there is a greater proportion of electrical power produced by the system for a given amount of biogas.

The decline in thermal power output occurs largely because increasing the fuel utilization reduces the amount of residual fuel passed to the afterburner; this leads to a dramatic decline in afterburner temperature which is propagated down the tail gas line to the exhaust.

The CHP efficiency declines largely because of the marked drop in thermal power output. More specifically, the fall in thermal power output is dramatic enough to cause the total power output to fall at a sharper rate than the biogas feed rate (denominator of efficiency calculation).

When the fuel utilization is lowered below 71 %, the afterburner temperature exceeds 1000°C due to the high amount of residual fuel being passed from the stack. In contrast, increasing the fuel utilization reduces the residual fuel amount, which causes the afterburner and tail gas temperatures to fall; upward of 85 % the tail gas temperature lowers to the point at which the minimum approach temperature of HX 5 is violated. Similar to the case of decreasing oxidant utilization (see section 4.2.4), the violation occurs between the hot-side inlet (tail gas, which lowers to 850°C) and the cold-side outlet (reformer feed, which is held at 800°C). Noting these constraint violations, the feasible range for fuel utilization is found to be between 71 and 85 %.

In summary, the system performance is more complicated than the previous cases. For example, in previous cases all performance metrics either

increased or decreased throughout the variable sweeps. In this case, as the fuel utilization is increased, the electrical power output is barely affected because the increase in cell temperature is well balanced by a decrease in H_2 concentration. Despite a considerable rise in electrical efficiency, there is a slight reduction in CHP efficiency largely because the drop-off in thermal power output is so dramatic.

The feasible range for fuel utilization on Ravensview biogas extends from 71 to 85 %. At the low bound, the afterburner temperature exceeds 1000°C; at the high bound, the minimum approach temperature constraint of HX 5 is violated.

4.2.5. Estimation of the Maximum System Performance

The purpose of this section is to estimate the conditions of maximum feasible performance for the pilot plant operating on Ravensview biogas. To this end, the following procedure is followed: an initial two-variable sensitivity analysis is carried relative to fuel and oxidant utilization with the steam-to-carbon ratio held at 2.8. Conditions yielding maximum values for electrical power output, electrical efficiency, and CHP efficiency are identified subject to the design constraints of table 4.2.1. Because the steam-to-carbon ratio is held at 2.8, these initial maximum values correspond to conservative performance whereby a safety factor is applied against carbon formation. In a second analysis, these performance values are upgraded to global maxima by reducing the steam-to-carbon ratio to the carbon-forming limit. In either case, emphasis was placed on electrical and CHP performance such that conditions for maximum thermal power output were not identified. With that said, conditions that approach the maximum thermal power output are demonstrated.

Figure 4.2.5.1 illustrates the system performances relative to fuel and oxidant utilization (two-variable sensitivity analysis). To enhance the readability of figure 4.2.5.1, the surfaces have been subdivided into 1 % by 1 % elements by white gridlines. In addition, each shade colouring corresponds with the range the surfaces pass through on the vertical axes.

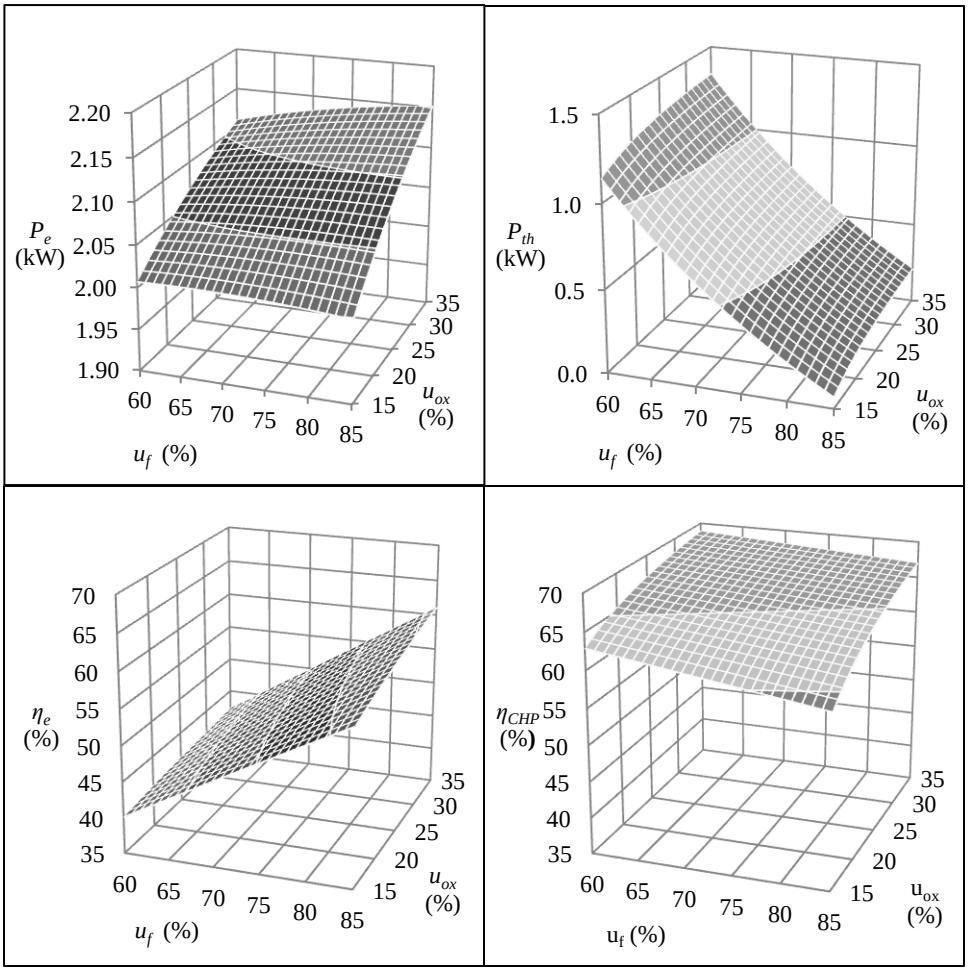

Figure 4.2.5.1 System performance relative to fuel and oxidant utilization (two-variable sensitivity analysis). The surfaces have been subdivided into 1 % x 1 % square units of fuel and oxidant utilization.

The performance behaviors mirror those determined in previous sections. For example, it was found in section 4.2.3 that increasing the oxidant utilization increases all performance metrics, which is the pattern observed in figure 4.2.5.1. In section 4.2.4 it was found that increasing the fuel utilization increases the electrical efficiency, but lowers the CHP efficiency and thermal power output. Again, these trends are apparent in figure 4.2.5.1. With that said, there is a behavioral deviation in the electrical power output. For example, in section 4.2.4,

the electrical power output was shown to be relatively unchanged by fuel utilization adjustment. However, figure 4.2.5.1 (top-left) shows that, at higher oxidant utilizations (greater than 20 %), the electrical power output actually increases with rising fuel utilization. The explanation for this is as follows. From section 4.2.4, it was noted that increasing the fuel utilization reduces the heat sink within the hotbox because the molar amount of CH_4 converted within the reformer is diminished relative to the extent of the electrochemical reaction; this encourages a rise in hotbox temperature. In the current context, at higher oxidant utilizations, there is less air mass passing through the hotbox to buffer against the temperature rise. As a result, at higher oxidant utilizations, the hotbox temperature becomes more sensitive to the fuel utilization (demonstrated below in figure 4.2.5.2). By extension, the electrical power output also becomes more sensitive to the fuel utilization because of the strong response in cell conductivity to the hotbox temperature. It is worth noting here that, as the hotbox temperature varies, the influence of cell conductivity on cell voltage is much more significant that the shifting cell gas composition.

It can easily be seen that figure 4.2.5.1 contains maximum values for electrical power output, electrical efficiency, CHP efficiency and thermal power output. However, unlike in previous sections, the variable ranges of figure 4.2.5.1 extend into regions where some design constraints are violated; this was allowed in order to maintain the square base of the three-dimensional plots. Figure 4.2.5.2 shows the regions where the constraints are violated. For example, figure 4.2.5.2 (top-left) shows that at low fuel utilization and high oxidant utilization the afterburner temperature exceeds 1000°C. Figure 4.2.5.2 (bottom-left and right) shows that conditions of high fuel utilization and low oxidant utilization lead to the minimum approach temperatures of HX 1 and HX 5 falling below 50°C. In fact, at a fuel utilization of 85 % and oxidant utilization of 15 %, the minimum approach temperature of HX 5 is close to zero. Figure 4.2.5.2 (top-right) simply shows that the hotbox/cell temperature reaches 880°C (high end of the 150°C temperature range constraint recommended for the C_T constant) at 85 % fuel utilization and 35 % oxidant utilization.

The feasible operating region is the region in which none of the constraints are violated; it is within this region that the maximum performance values were determined. Table 4.2.5.1 lists the maximum values for electrical power output, electrical efficiency and CHP efficiency that were identified within the feasible region. All of these values occur at the design conditions of 85 % fuel utilization and 31 % oxidant utilization. From figure 4.2.5.2 it can be seen that this design point has the maximum allowable fuel utilization (85 %) and that if the oxidant utilization is increased further the afterburner temperature will exceed 1000°C.

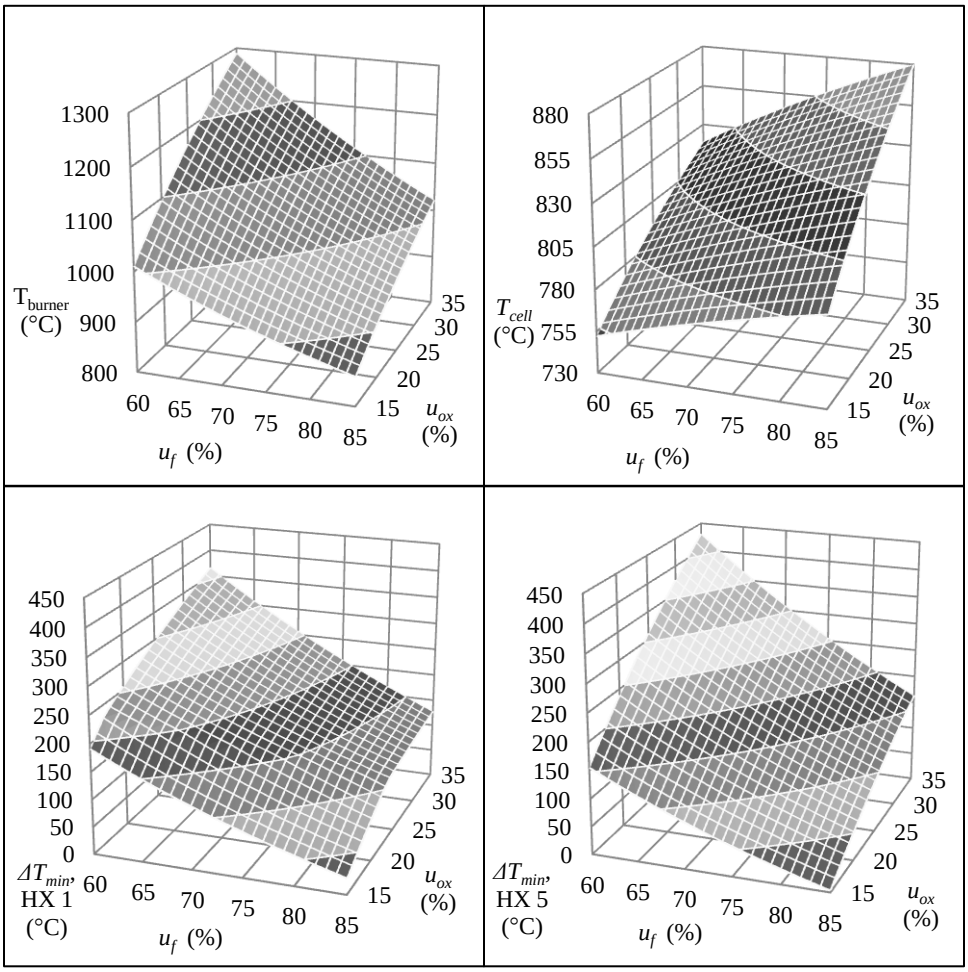

Figure 4.2.5.2. Afterburner temperature (top left), hotbox/cell temperature (top right), and minimum approach temperatures of heat exchangers 1 (bottom left) and 5 (bottom right) as a function of fuel and oxidant utilization (two-variable sensitivity analysis). The surfaces have been subdivided into 1 % x 1 % square units of fuel and oxidant utilization.

Table 4.2.5.1. Estimates for maximum feasible gross electrical power output, gross electrical efficiency, and CHP efficiency at a steam-to-carbon ratio of 2.8.

Performance Metric	Maximum Performance Value	Design Conditions
Gross electrical power output, P_e (kW)	2.1	u_f = 85 %, u_{ox} = 31 %, $r_{H2O/C}$ = 2.8
Gross electrical efficiency, η_e (%)	60	u_f = 85 %, u_{ox} = 31 %, $r_{H2O/C}$ = 2.8
CHP efficiency, η_{CHP} (%)	66	u_f = 85 %, u_{ox} = 31 %, $r_{H2O/C}$ = 2.8

Considering figures 4.2.5.1 and 4.2.5.2, the maximum thermal power output is 1.02 kW and occurs at 62 % fuel utilization and 15 % oxidant utilization. However, this is not the true maximum feasible value because there is still freedom to enhance the value outside of the bounds of the figure. For example, further lowering the fuel and oxidant utilizations along the afterburner temperature limit of 1000°C will continue to enhance the thermal power output. In any event, focus was kept to measures that include the electrical performance and maximum thermal performance was not determined.

In section 4.2.2 it was found that lowering the steam-to-carbon ratio would increase all performance metrics until the carbon formation limit was reached. Therefore, as a final exercise, the reduction of the steam-to-carbon ratio was carried out at the design point of 85 % fuel utilization and 31 % oxidant utilization. Table 4.2.5.2 lists the new performance estimates.

Table 4.2.5.2. Estimates for maximum feasible gross electrical power output, gross electrical efficiency, and CHP efficiency at a steam-to-carbon ratio of 1.6 (carbon-forming limit).

Performance Metric	Maximum Performance Value	Design Conditions
Gross electrical power output, P_e (kW)	2.2	u_f = 85 %, u_{ox} = 31 %, $r_{H2O/C}$ = 1.6
Gross electrical efficiency, η_e (%)	62	u_f = 85 %, u_{ox} = 31 %, $r_{H2O/C}$= 1.6
CHP efficiency, η_{CHP} (%)	77	u_f = 85 %, u_{ox} = 31 %, $r_{H2O/C}$= 1.6

As expected, there is an increase in performance compared to the values of table 4.2.5.1, with the largest gains accrued for the CHP efficiency.

It should be noted that the values of table 4.2.5.2 are only estimates for the global maximum feasible performance values. For example, lowering the steam-to-carbon ratio to 1.6 lowers the afterburner temperature from 995 to 986°C. This means that the oxidant utilization can be further increased by a percentage point to enhance the system performance before the afterburner temperature constraint is reached again. With that said, when this final adjustment was carried out, the gains in performance were minimal (less than a percentage point for each metric), suggesting that the maximum values presented in table 4.2.5.2 are reasonable estimates for the global maximum feasible values. In the strictest sense, the global maximum feasible values should be determined from a constrained multivariable optimization procedure whereby the fuel utilization, oxidant utilization and steam-to-carbon ratio are all concurrently and iteratively adjusted.

5. CONCLUSIONS AND RECOMMENDATIONS

Biogas is a renewable source of energy that is currently underutilized at smaller WWTPs because of the capital and maintenance costs associated with CHP technologies and biogas purification. Compared to other CHP technologies, SOFC technology has typically been more expensive and restricted to the demonstration phase of development. However, since 2010, a number of manufacturers have broken into commercial markets and the capital cost of SOFC systems seems to be declining. Given the superior efficiency and more environmentally-friendly emissions profiles of SOFC systems relative to other CHP technologies, the further development of integrated AD-SOFC systems could increase the incidence of biogas utilization at WWTPs.

In this work, a process model of 2 kW_e SOFC pilot plant that can be directly integrated with the AD process was developed using UniSim Design™. Crucially, the pilot plant uses the inexpensive adsorbent materials, alkali-impregnated AC and heated activated alumina, to selectively target the two main biogas contaminants, H_2S and siloxanes. The pilot plant is proposed for construction at the Ravensview WWTP in Kingston, Ontario.

At reference conditions, the system was estimated to provide gross electrical and thermal power outputs of 2.1 kW_e and 0.31 kW_{th}, respectively. At these conditions, the gross electrical and CHP efficiencies were 54.7 % and 62.9 %, respectively. The process model was then used to explore the effect of biogas composition and feed stream flow rates (key design variables) on system performance. The feed flow rates were controlled according to the steam-to-carbon ratio, oxidant utilization, and fuel utilization.

Conclusions from the sensitivity analyses are as follows:

- The pilot plant can be feasibly operated over the full range of expected biogas compositions reported by Wheeldon *et al*. [3]. If condensation is to be avoided in the exhaust stream, the pilot plant can be operated on biogases as lean as 47 % CH_4 content. The results also indicated that operation on 100% CH_4 is possible, suggesting that the system might also be designed for operation on natural gas fuel.
- Overall performance increases with increasing CH_4 content, and the thermal power output and CHP efficiency are particularly affected.
- Gains in system performance are expected if the steam-to-carbon ratio can be reduced below that typically used for natural gas fuel processing. Similar to the case of varying biogas composition, the thermal power output and CHP efficiency are particularly affected.

- Increasing the oxidant utilization enhances all performance metrics; however, the effect was not as pronounced as with the other design variables.
- Varying the fuel utilization can be used to adjust the balance between gross electrical efficiency and thermal power output without significantly compromising the gross electrical power output and CHP efficiency.
- Based on a two-variable sensitivity study between fuel and oxidant utilization, the maximum feasible performance in terms of gross electrical power output, gross electrical efficiency and CHP efficiency were estimated to be 2.1 kW_e, 60 % and 66 %, respectively; all of these performances were achieved at 85 % fuel utilization and 31 % oxidant utilization. It was then determined that if the steam-to-carbon ratio could be reduced at this point from 2.8 to 1.6 (the thermodynamic carbon formation limit), the gross electrical power output, gross electrical efficiency, and CHP efficiency could all be enhanced to 2.2 kW_e, 62 %, and 77 %, respectively. The latter design point was considered to be an estimate for global maximum performance between the three independent variables.

This work also included an experimental component which led to the following outcomes:

- The successful operation of an 8-celled prospective TSOFC stack on processed biogas (simulated reformate).
- The development of an empirical cell model that can be regressed to the experimental performance of SOFCs.
- The successful regression of the empirical cell model to the performance of the prospective TSOFC stack, which was subsequently programmed into the process model. Therefore, the modeled performance of the pilot plant was based on the experimental performance of a real, prospective SOFC stack.

Although the process model was demonstrated as a useful design tool, details can be added to make it more useful. For example, pressure drops can be specified throughout the system to allow for pump sizing. Adding pumps to the model and accounting for their parasitic draw would give a more realistic estimate for the electrical power output. Perfect insulation was assumed throughout the system, which implies that the system must be heavily insulated to yield the performances reported in this work. It is always possible to add enough insulation to make the heat losses negligible, but this can be better addressed from an economic perspective if the trade-off between insulation thickness and heat loss is programmed into the model. Additional benefits could be realized by converting

the model from a steady-state design model into either a steady-state predictive model or dynamic predictive model.

Lastly, the biogas purification sequence still must be proven. It is based on the reported selectivity of alkali-impregnated AC and heated activated alumina toward H_2S and siloxane, respectively. In addition, both materials are also likely to remove other trace contaminant species. Further testing is required to determine the optimal bed sizes and performance of the purification sequence.

WORKS CITED

[1] Wiser, J. R., Schettler, J. W., & Willis, J. L. (2010). *Evaluation of Combined Heat and Power Technologies for Wastewater Facilities.* Atlanta: Brown and Caldwell.

[2] Shuler, M. L., & Kargi, F. (2002). *Bioprocess Engineering: Basic Concepts. 2nd. ed.* Upper Saddle River: Prentice Hall, Inc.

[3] Wheeldon, I., Caners, C., Karan, K., & Peppley, B. (2007). Utilization of Biogas Generated from Ontario Wastewater Treatment Plants in Solid Oxide Fuel Cell Systems: A Process Modeling Study. *International Journal of Green Energy*, 221–231.

[4] Spiegel, R. J., & Preston, J. L. (2000). Test Results for Fuel Cell Operation on Anaerobic Digester Gas. *Journal of Power Sources*, 283-288.

[5] Rasi, S., Veijanen, A., & Rintala, J. (2007). Trace Compounds of Biogas from Different Biogas Production Plants. *Energy*, 1375–1380.

[6] Ajhar, M., Travesset, M., Yüce, S., & Melin, T. (2010). Siloxane Removal from Landfill and Digester Gas – A Technology Overview. *Bioresource Technology*, 2913–2923.

[7] Rasi, S., Läntelä, J., & Rintala, J. (2011). Trace compounds affecting biogas energy utilisation – A review. *Energy Conversion and Management*, 3369–3375.

[8] Eastern Research Group (ERG), Inc. and Resource Dynamics Corporation (RDC). (2011). *Opportunities for Combined Heat and Power at Wastewater Treatment Facilities: Market Analysis and Lessons from the Field.* U.S. Environmental Protection Agency and Combined Heat and Power Partnership.

[9] Farhad, S., Yoo, Y., & Hamdullahpur, F. (2010). Effects of Fuel Processing Methods on Industrial Scale Biogas-Fuelled Solid Oxide Fuel Cell System for Operating in Wastewater Treatment Plants. *Journal of Power Sources*, 1446–1453.

[10] Corigliano, O., Florio, G., & Fragiacomo, P. (2010). Employing Solid Urban Waste in an IIR-SOFC in Cogenerative Arrangement. *International Journal of Energy*, 17-28.

[11] Energy and Environmental Analysis, Inc. and Eastern Research Group (ERG), Inc. (2007). *Biomass Combined Heat and Power Catalog of Technologies.* U. S. Environmental Protection Agency and Combined Heat and Power Partnership.

[12] Onovwiona, H. I., & Ugursal, V. I. (2006). Residential Cogeneration Systems: Review of the Current Technology. *Renewable and Sustainable Energy Reviews*, 389–431.

[13] Van herle, J., Marechal, F., Leuenberger, S., & D. Favrat, D. F. (2003). Energy Balance Model of a SOFC Cogenerator Operated with Biogas. *Journal of Power Sources*, 375–383.

[14] Shiratori, Y., Oshima, T., & Sasaki, K. (2008). Feasibility of Direct-Biogas SOFC. *International Journal of Hydrogen Energy*, 6316–6321.

[15] Biocell. (2012, 10 18). *Biocell*. Retrieved 12 29, 2012, from http://www.life-biocell.eu/index.php

[16] Schwarz, K., Peuker, P., Freund, S., & Kunath, R. (2009). *2008 Annual Report.* Dresden: Fraunhofer Institute for Ceramic Technologies and Systems IKTS.

[17] Sandström, C.-E., Noponen, M., & Hottinen, T. (2011, 6 21). *WFC20 Biogas Unit Operation.* Retrieved 12 31, 2012, from Elforsk: http://www.elforsk.se/PageFiles/2163/W%C3%A4rtsil%C3%A4_Carl-Erik_Sandstr%C3%B6m.pdf

[18] Monge, I. G. (n.d.). *BioSOFC - Design and Demonstration of 3 CHP Plants using Two 5kW Solid Oxide Fuel Cells (SOFC) Working with Landfill Gas and Biogas from Anaerobic Digestion.* Retrieved 12 31, 2012, from European Commission LIFE Programme: http://ec.europa.eu/environment/life/project/Projects/index.cfm?fuseaction=search.dspPage&n_proj_id=3076&docType=pdf

[19] Van herle, J., Membrez, Y., & Bucheli, O. (2004). Biogas as a Fuel Source for SOFC Co-Generators. *Journal of Power Sources*, 300–312.

[20] Carter, D., Ryan, M., & Wing, J. (2012, 07). *The Fuel Cell Industry Review 2012.* Retrieved 03 17, 2013, from Fuel Cell Today: http://www.fuelcelltoday.com/media/1713685/fct_review_2012.pdf

[21] Fuel Cell Today. (2011, 07). *The Fuel Cell Today Industry Review 2011*. Retrieved 03 18, 2013, from Fuel Cell Today: http://www.fuelcelltoday.com/media/1351623/the_industry_review_2011.pdf

[22] Adams, T. A., Nease, J., Tucker, D., & Barton, P. I. (2012). Energy Conversion with Solid Oxide Fuel Cell Systems: A Review of Concepts and Outlooks for the Short- and Long-Term. *Industrial & Engineering Chemistry Research*, 3089 - 3011.

[23] Eastern Research Group (ERG), Inc. and Energy and Environmental Analysis, Inc. (2007). *Opportunities for and Benefits of Combined Heat and Power at Wastewater Treatment Facilities.* U.S. Environmental Protection Agency and Combined Heat and Power Partnership.

[24] Champagne, P. (2009). *Development of an Integrated Anaerobic Digestion - Solid Oxide Fuel Cell System.* Research Grant Application, Kingston.

[25] EG&G Technical Services, Inc. (2004). *Fuel Cell Handbook 7th ed.* Morgantown: U.S. Department of Energy.

[26] Bartholomew, C. H. (2001). Mechanisms of Catalyst Deactivation. *Applied Catalysis A*, 17–60.

[27] Haga, K., Adachi, S., Shiratori, Y., Itoh, K., & Sasaki, K. (2008). Poisoning of SOFC Anodes by Various Fuel Impurities. *Solid State Ionics*, 1427 – 1431.

[28] Sasaki, K., Haga, K., Yoshizumi, T., Minematsu, D., Yuki, E., Liu, R., . . . Yokomoto, K. (2011). Chemical Durability of Solid Oxide Fuel Cells: Influence of Impurities on Long-Term Performance. *Journal of Power Sources*, 9130 – 9140.

[29] Abatzoglou, N., & Boivin, S. (2009). A Review of Biogas Purification Processes. *Biofuels, Bioproducts & Biorefining*, 42–71.

[30] Urban, W., Lohmann, H., & Salazar Gómez, J. I. (2009). Catalytically Upgraded Landfill Gas as a Cost-Effective Alternative for Fuel Cells. *Journal of Power Sources*, 359–366.

[31] Finocchio, E., Garuti, G., Baldi, M., & Busca, G. (2008). Decomposition of Hexamethylcyclotrisiloxane over Solid Oxides. *Chemosphere*, 1659–1663.

[32] TOTO Ltd. (2013). *About TOTO: Fuel Cell Stack*. Retrieved from TOTO: http://www.toto.co.jp/company/profile_en/technology/sofc/index.htm

[33] Shiratori, Y., Quang, T. T., Takahashi, Y., Taniguchi, S., & Sasaki, K. (2011). Highly Efficient Biomass Utilization with Solid Oxide Fuel Cell Technology. In M. Nayeripour, & M. Kheshti, *Renewable Energy - Trends and Applications* (pp. 165 - 190). Rijeka: InTech.

[34] Larminie, J., & Dicks, A. (2003). *Fuel Cell Systems Explained. 2nd. ed.* Chichester: John Wiley & Sons Ltd.

[35] Peters, R., Deja, R., Blum, L., Pennanen, J., Kiviaho, J., & Hakala, T. (2013). Analysis of Solid Oxide Fuel Cell System Concepts with Anode Recycling. *International Journal of Hydrogen Energy*, 6809 - 6820.

[36] Deutschmann, O., & Schmidt, L. D. (1998). Modeling the Partial Oxidation of Methane in a Short-Contact-Time Reactor. *AIChE Journal*, 2465 - 2477.

[37] Holladay, J. D., Hu, J., King, D. L., & Wang, Y. (2009). An Overview of Hydrogen Production Technologies. *Catalysis Today*, 244 – 260.

[38] Er-rbib, H., Bouallou, C., & Werkoff, F. (2012). Dry Reforming of Methane – Review of Feasibility Studies. *Chemical Engineering Transactions*, 163 - 168.

[39] Van herle, J., Maréchal, F., Leuenberger, S., Membrez, Y., Bucheli, O., & Favrat, D. (2004). Process Flow Model of Solid Oxide Fuel Cell System Supplied with Sewage Biogas. *Journal of Power Sources*, 127–141.

[40] Christensen, T. S. (1996). Adiabatic Prereforming of Hydrocarbons - An Important Step in Syngas Production. *Applied Catalysis A: General*, 285 - 309.

[41] Arespacochaga, d., Mesa, Hornero, Larrotcha, Sánchez, Peregrina, & Bouchy. (2011, December 12). *Sewage Biogas-Powered SOFC: Possibilities and Limitations.* Retrieved April 25, 2012, from European Fuel Cell Conference & Exhibition: www.europeanfuelcell.it/images/6b/11095.pdf

[42] Laine, J. (2008, 10 29). *Status of the Solid Oxide Fuel Cell System Development at Wärtsilä.* Retrieved 08 08, 2013, from Fuel Cell Seminar & Energy Exposition: http://www.fuelcellseminar.com/assets/pdf/2008/wednesday/RDP31-3_JLaine.ppt.pdf

[43] Mogensen, D., Grunwaldt, J. D., Hendriksen, P. V., Dam-Johansen, K., & Nielsen, J. U. (2011). Internal Steam Reforming in Solid Oxide Fuel Cells: Status and Opportunities of Kinetic Studies and their Impact on Modelling. *Journal of Power Sources*, 25–38.

[44] Ormerod, M., & Staniforth, J. (2001). Running Fuel Cells on Biogas - a Renewable Fuel. *Green Chemistry*, G61-G63.

[45] Shiratori, Y., Ijichi, T., Oshima, T., & Sasaki, K. (2010). Internal Reforming SOFC Running on Biogas. *International Journal of Hydrogen Energy*, 7905-7912.

[46] Shiratori, Y., & Sasaki, K. (2008). NiO–ScSZ and Ni0.9Mg0.1O–ScSZ-Based Anodes Under Internal Dry Reforming of Simulated Biogas Mixtures. *Journal of Power Sources*, 738 – 741.

[47] Staniforth, J., & Kendall, K. (1998). Biogas Powering a Small Tubular Solid Oxide Fuel Cell. *Journal of Power Sources*, 275 – 277.

[48] Staniforth, J., & Kendall, K. (2000). Cannock Landfill Gas Powering a Small Tubular Solid Oxide Fuel Cell — a Case Study. *Journal of Power Sources*, 401–403.

[49] Staniforth, J., & Ormerod, M. (2002). Implications for Biogas as a Fuel Source for Solid Oxide Fuel Cells: Internal Dry Reforming in Small Tubular Solid Oxide Fuel Cell. *Catalysis Letters*, 19-23.

[50] Yentekakis, I. V. (2006). Open- and Closed-Circuit Study of an Intermediate Temperature SOFC Directly Fueled with Simulated Biogas Mixtures. *Journal of Power Sources*, 422–425.

[51] Farhad, S., Hamdullahpur, F., & Yoo, Y. (2010). Performance Evaluation of Different Configurations of Biogas-Fuelled SOFC Micro-CHP Systems for Residential Applications. *International Journal of Hydrogen Energy*, 3758–3768.

[52] Meusinger, J., Riensche, E., & Stimming, U. (1998). Reforming of Natural Gas in Solid Oxide Fuel Cell Systems. *Journal of Power Sources*, 315 – 320.

[53] Nishino, T., & Szmyd, J. (2010). Numerical Analysis of a Cell-Based Indirect Internal Reforming Tubular SOFC Operating With Biogas. *Journal of Fuel Cell Science and Technology*, 051004-1-051004-8.

[54] Yi, Y., Rao, A. D., Brouwer, J., & Samuelsen, G. S. (2005). Fuel Flexibility Study of an Integrated 25kW SOFC Reformer System. *Journal of Power Sources*, 67–76.

[55] Piroonlerkgul, P., Laosiripojana, N., Adesina, A. A., & Assabumrungrat, S. (2009). Performance of Biogas-Fed Solid Oxide Fuel Cell Systems Integrated with Membrane Module for CO2 Removal. *Chemical Engineering and Processing*, 672–682.

[56] Stelter, M., Jahn, M., Heddrich, M., Kuznezoff, M., & Friedrich, E. (2008, 10 29). *SOFC-CHP System Operated on Biogas.* Retrieved 08 07, 2013, from Fuel Cell Seminar & Energy Exposition: http://www.fuelcellseminar.com/assets/pdf/2008/wednesday/RDP31-6_Stelter.ppt.pdf

[57] Schwarz, K., Peuker, P., Preis, S., & Kunath, R. (2008). *2007 Annual Report.* Dresden: Fraunhofer Institute for Ceramic Technologies and Systems IKTS.

[58] Wärtsilä Corporation. (2010, 02 22). *Wärtsilä has been Highly Successful in Operating its Groundbreaking Fuel Cell Unit.* Retrieved 08 08, 2013, from Wärtsilä: http://www.wartsila.com/en/press-releases/wartsila-has-been-highly-successful-in-operating-its-groundbreaking-fuel-cell-unit

[59] Sandström, C.-E., Noponen, M., & Hottinen, T. (2011, 6 21). *WFC20 Biogas Unit Operation.* Retrieved 12 31, 2012, from Elforsk: http://www.elforsk.se/PageFiles/2163/W%C3%A4rtsil%C3%A4_Carl-Erik_Sandstr%C3%B6m.pdf

[60] Biocell. (2012). *Biocell. Energy Self-Sustaining and Environmental Footprint Reduction on Wastewater Treatment Plants via Fuel Cells.* Barcelona: Life+ Programme (European Commission).

[61] Eastern Research Group (ERG), Inc. and Resource Dynamics Corporation. (2011). *Opportunities for Combined Heat and Power at Wastewater Treatment Facilities: Market Analysis and Lessons from the Field.* U.S. Environmental Protection Agency and Combined Heat and Power Partnership.

[62] Chun, S. (2010). *CanSES SOFC Test Rig Test Plan.* Kingston: Fuel Cell Research Centre.

[63] Baron, S., Brandon, N., Atkinson, A., Steele, B., & Rudkin, R. (2004). The Impact of Wood-Derived Gasification Gases on Ni-CGO Anodes in Intermediate Temperature Solid Oxide Fuel Cells. *Journal of Power Sources*, 58–66.

[64] Mogensen, D., Grunwaldt, J. D., Hendriksen, P. V., Dam-Johansen, K., & Nielsen, J. U. (2011). Internal Steam Reforming in Solid Oxide Fuel Cells: Status and Opportunities of Kinetic Studies and their Impact on Modelling. *Journal of Power Sources*, 25–38.

[65] Campanari, S. (2001). Thermodynamic Model and Parametric Analysis of a Tubular SOFC Module. *Journal of Power Sources*, 26-34.

[66] Hirschenhofer, J. H., Stauffer, D. B., & Engleman, R. R. (1994). *Fuel Cells, A Handbook (rev.3).* Morgantown: Gilbert and Commonwealth Inc. for US Department of Energy (DOE).

[67] Kim, K.-J., Kang, C.-S., You, Y.-J., Chung, M.-C., Woo, M.-W., Jeong, W.-J., . . . Ahn, H.-G. (2006). Adsorption–Desorption Characteristics of VOCs Over Impregnated Activated Carbons. *Catalysis Today*, 223 – 228.

[68] Bashkova, S., Bagreev, A., & Bandosz, T. J. (2005). Catalytic Properties of Activated Carbon Surface in the Process of Adsorption/Oxidation of Methyl Mercaptan. *Catalysis Today*, 323 – 328.

[69] Ferreira-Aparicio, P., Benito, M. J., & Sanz, J. L. (2005). New Trends in Reforming Technologies: from Hydrogen Industrial Plants to Multifuel Microreformers. *Catalysis Reviews*, 491–588.

[70] Rostrup-Nielsen, J. R. (1984). Catalytic Steam Reforming. In J. R. Anderson, & M. Boudart, *Catalysis: Science and Technology Vol. 5* (pp. 1 - 117). Berlin: Springer-Verlag.

[71] Dokmaingam, P., Assabumrungrat, S., Soottitantawat, A., & Laosiripojana, N. (2010). Modelling of Tubular-Designed Solid Oxide Fuel Cell with Indirect Internal Reforming Operation Fed by Different Primary Fuels. *Journal of Power Sources*, 69–78.

[72] Petersson, A., & Wellinger, A. (2009). *Biogas Upgrading Technologies – Developments and Innovations.* IEA Bioenergy.

[73] Honeywell. (2010). *UniSim Thermo: Reference Guide.* London: Honeywell.

[74] Kreith, F., & Bohn, M. S. (2001). *Principles of Heat Transfer. 6th ed.* Pacific Grove: Brooks/Cole.

[75] Bove, R., Lunghi, P., & Sammes, N. M. (2005). SOFC Mathematical Model for Systems Simulations - Part 2: Definition of an Analytical Model. *International Journal of Hydrogen Energy*, 189–200.

[76] OSB Services. (2009). *Characterizing Sludge Digester Gases at Ravensview WPCP.* Mississauga: OSB Services.

[77] Larrain, D., Van herle, J., & Favrat, D. (2006). Simulation of SOFC Stack and Repeat Elements Including Interconnect Degradation and Anode Reoxidation Risk. *Journal of Power Sources*, 392 – 403.

[78] Baade, W. F., Parekh, U. N., & Raman, V. S. (2003). Hydrogen. In *Kirk-Othmer Encyclopedia of Chemical Technology* (pp. 759-808). John Wiley & Sons, Inc.

[79] Suwanwarangkul, R., Croiset, E., Pritzker, M. D., Fowler, M. W., Douglas, P. L., & Entchev, E. (2007). Modelling of a Cathode-Supported Tubular Solid Oxide Fuel Cell Operating with Biomass-Derived Synthesis Gas. *Journal of Power Sources*, 386 – 399.

[80] Sasaki, K., Hori, Y., Kikuchi, R., Eguchi, K., Ueno, A., Takeuchi, H., . . . Uchida, Y. (2002). Current-Voltage Characteristics and Impedance Analysis of Solid Oxide Fuel Cells for Mixed H2 and CO Gases. *Journal of The Electrochemical Society*, A227 - A233.

[81] Kolbitsch, P., Pfeifer, C., & Hofbauer, H. (2008). Catalytic Steam Reforming of Model Biogas. *Fuel*, 701–706.

[82] Effendi, A., Zhang, Z. G., Hellgardt, K., Honda, K., & Yoshida, T. (2002). Steam Reforming of a Clean Model Biogas over Ni/Al2O3 in Fluidized- and Fixed-bed Reactors. *Catalysis Today*, 181–189.

REFERENCES

[83] Atlas Steels. (2011, Jan.). *Grade Data Sheet.* Retrieved Nov. 19, 2012, from Atlas Steels: http://www.atlassteels.com.au/documents/Atlas_Grade_datasheet_310_rev_Jan_2011.pdf

[84] Bhattacharyya, D., Rengaswamy, R., & Finnerty, C. (2009). Dynamic Modeling and Validation Studies of a Tubular Solid Oxide Fuel Cell. *Chemical Engineering Science*, 2158--2172.

[85] Blum, L., Deja, R., Peters, R., & Stolten, D. (2011). Comparison of Efficiencies of Low, Mean, and High Temperature Fuel Cell Systems. *International Journal of Hydrogen Energy*, 11056 - 11067.

[86] Bove, R., Lunghi, P., & Sammes, N. M. (2005). SOFC Mathematic Model for Systems Simulations. Part One: from a Micro-Detailed to Macro-Black-Box Model. *International Journal of Hydrogen Energy*, 181–187.

[87] Division of Fuel Cell & Energy Technology Ningbo Institute of Materials Technology & Engineering, Chinese Academy of Sciences. (n.d.). *Electrolyte-supported Cells.* Retrieved 1 5, 2013, from Ningbo Institute of Materials Technology & Engineering, Chinese Academy of Sciences, Division of Fuel Cell & Energy Technology : http://www.sofc.com.cn/sszcell.html

[88] Lee, J. H., Kim, K. M., Kim, S. H., & Lee, C. S. (2004). Effect of Steam on Coking in the Non-catalytic Pyrolysis of Naphtha Components. *Korean Journal of Chemical Engineering*, 252-256.

[89] Montgomery, D. C., & Runger, G. C. (2003). *Applied Statistics and Probability for Engineers. Third Edition.* New York: John Wiley & Sons, Inc.

[90] Ningbo Ningbo Institute of Materials Technology & Engineering, Chinese Academy of Sciences. (2012, 11 1). *NIMTE SOFC Cell Performances Recently Improved.* Retrieved 1 5, 2013, from Ningbo Ningbo Institute of Materials Technology & Engineering Chinese Academy of Sciences: http://english.nimte.cas.cn/ns/ne/201211/t20121101_94442.html

[91] Piroonlerkgul, P., Wiyaratn, W., Soottitantawat, A., Kiatkittipong, W., Arpornwichanop, A., Laosiripojana, N., & S. Assabumrungrat, S. A. (2009). Operation Viability and Performance of Solid Oxide Fuel Cell Fuelled by Different Feeds. *Chemical Engineering Journal*, 411 – 418.

[92] Santarelli, M., Gariglio, M., De Benedictis, F., Delloro, F., Calì, M., & Orsello, G. (2010). SOFC 5 kWe CHP Field Unit: Effect of the Methane Dilution. *Fuel Cells*, 453–462.

[93] Siebert, O. W., Brooks, K. M., Craigie, L. J., Hodge, F. G., Hutton, L. T., Laronge, T. M., . . . Stoecker, J. G. (2008). Materials of Construction. In D. W. Green, & R. H. Perry, *Perry's Chemical Engineers' Handbook. 8th ed.* (pp. 25-1 - 25-51). New York: McGraw-Hill.

[94] Standaert, F., Hemmes, K., & Woudstra, N. (1996). Analytical Fuel Cell Modeling. *Journal of Power Sources*, 221-234.

[95] Wärtsilä Corporation. (2008, 02 21). *Wärtsilä to Deliver the World's First SOFC Fuel Cell Power Plant using Landfill Gas to the Vaasa Housing Fair Site.* Retrieved 08 08, 2013, from Wärtsilä: http://www.wartsila.com/en/press-releases/first-sofc-fuel-cell-power-plant-using-landfill-gas

APPENDIX A: P&ID FOR THE CANSES TEST RIG

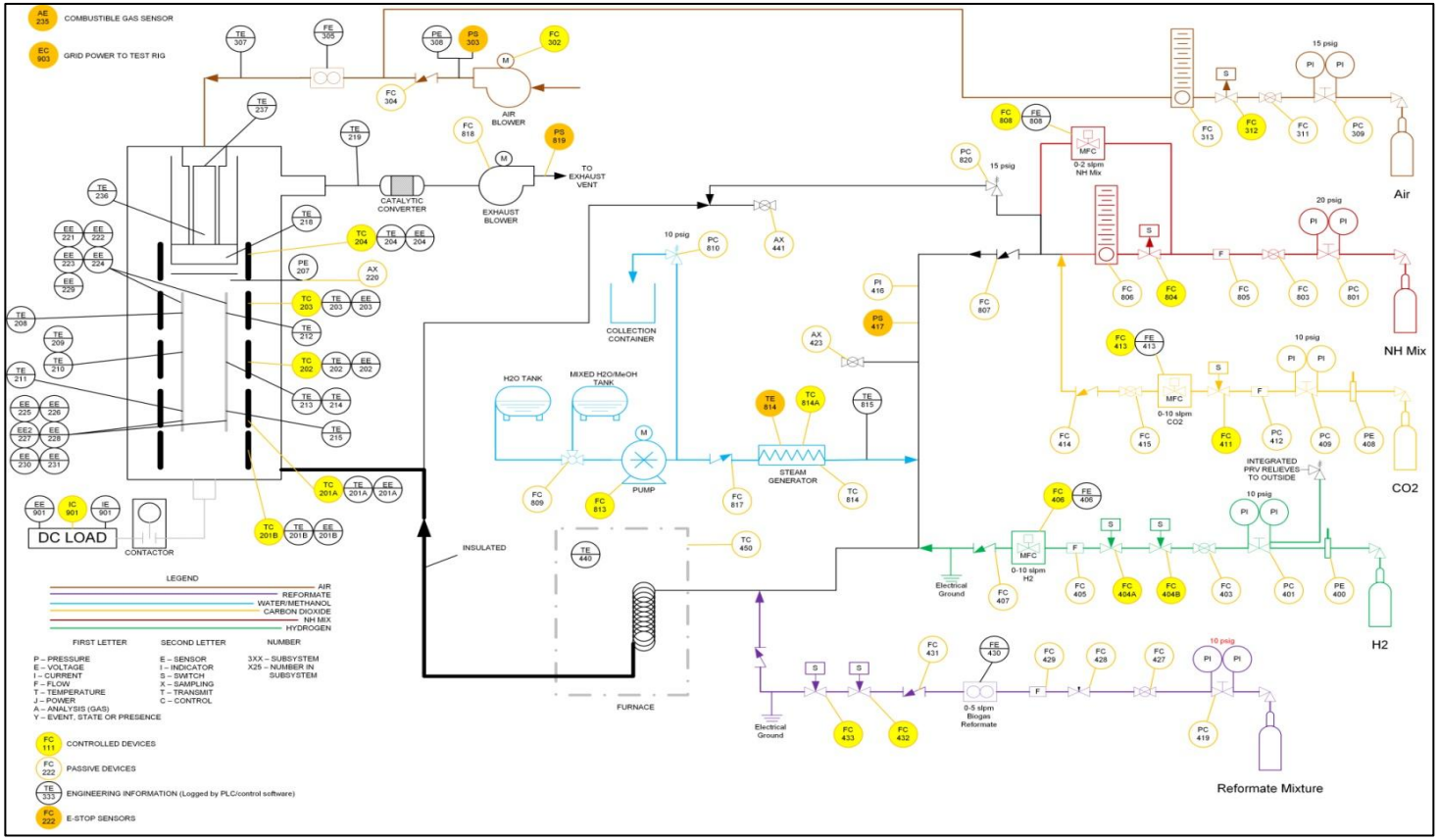

Figure A.1. P&ID for the CanSES test rig.

APPENDIX B: TAG LISTS FOR THE CANSES TEST RIG

Table B.1. Instruments within the CanSES test rig logged by the PLC/control software.

Tag ID	Instrument	Measurement
TE 201A	Type K Thermocouple	Bottom heater A temp.
TE 201B	Type K Thermocouple	Bottom heater B temp.
TE 202	Type K Thermocouple	Middle heater temp.
TE 203	Type K Thermocouple	Top heater temp.
TE 204	Type K Thermocouple	Combustion zone heater temp.
TE 208	Type K Thermocouple	Top left bundle temp.
TE 209	Type K Thermocouple	Middle left bundle 1 temp.
TE 210	Type K Thermocouple	Middle left bundle 2 temp.
TE 211	Type K Thermocouple	Bottom left bundle temp.
TE 212	Type K Thermocouple	Top right bundle temp.
TE 213	Type K Thermocouple	Middle right bundle 1 temp.
TE 214	Type K Thermocouple	Middle right bundle 2 temp.
TE 215	Type K Thermocouple	Bottom right bundle temp.
TE 218	Type K Thermocouple	Right combustion zone temp.
TE 219	Type K Thermocouple	Recuperator exhaust temp.
TE 236	Type K Thermocouple	Recuperator entrance temp. (from combustion zone)
TE 237	Type K Thermocouple	Air manifold bottom surface temp.
TE 250	Type K Thermocouple	Cathode feed tube exit temperature
TE 307	Type K Thermocouple	Air inlet temp. to recuperator
TE 440	Type K Thermocouple	Furnace temp.
EE 201A	2-wire voltage tap	Bottom heater A applied voltage readback
EE 201B	2-wire voltage tap	Bottom heater B applied voltage readback
EE 202	2-wire voltage tap	Middle heater applied voltage readback
EE 203	2-wire voltage tap	Top heater applied voltage readback
EE 204	2-wire voltage tap	Combustion zone heater voltage readback
EE 221	2-wire voltage tap	Cell 1 top voltage
EE222	2-wire voltage tap	Cell 2 top voltage
EE 223	2-wire voltage tap	Cell 3 top voltage
EE 224	2-wire voltage tap	Cell 4 top voltage

Table B.1, Continued.

Tag ID	Instrument	Measurement
EE 225	2-wire voltage tap	Cell 1 bottom voltage
EE 226	2-wire voltage tap	Cell 2 bottom voltage
EE 227	2-wire voltage tap	Cell 3 bottom voltage
EE 228	2-wire voltage tap	Cell 4 bottom voltage
EE 229	2-wire voltage tap	Stack top voltage
EE 230	2-wire voltage tap	Stack bottom voltage
EE 231	2-wire voltage tap	Busbar voltage
EE 901	Electronic load	Voltage readback from electronic load
FE 305	Mass flow meter	Air flow readback
FE 406	Mass flow controller	H_2 flow readback
FE 413	Mass flow controller	CO_2 flow readback
FE 430	Mass flow meter	Reformate flow readback
FE 808	Mass flow controller	NH Mix flow readback
PE 308	Differential pressure sensor	Stack air backpressure readback
PE 207	Differential pressure sensor	Anode-side stack pressure readback
IE 901	Electronic load	Current readback from electronic load

Table B.2. Devices within the CanSES test rig controlled by the PLC/control software.

Tag ID	Device	Function
TC 201A	Resistance heating element	Bottom heater A temp.
TC 201B	Resistance heating element	Bottom heater B temp.
TC 202	Resistance heating element	Middle heater temp.
TC 203	Resistance heating element	Top heater temp.
TC 204	Resistance heating element	Combustion zone heater temp.
FC 302	Centrifugal blower	Air flow control
FC 312	Solenoid value (fault open)	Air flow control
FC 404A	Solinoid valve (fault close)	H_2 flow control
FC 404B	Solinoid valve (fault close)	H_2 flow control
FC 406	Mass flow controller	H_2 flow control
FC 411	Solenoid valve (fault close)	CO_2 flow control
FC 413	Mass flow controller	CO_2 flow control
FC 432	Solenoid valve (fault close)	Reformate flow control
FC 433	Solenoid valve (fault close)	Reformate flow control
FC 804	Solenoid valve (fault open)	NH mix flow control
FC 808	Mass flow controller	NH mix flow control
FC 813	Low flow external gear pump	Water flow control

Table B.3. Instruments and devices within the CanSES test rig not controlled by the PLC/control software (passive devices/instruments).

Tag ID	Instrument/Device	Function
TC 450	Analogue temp. controller	Furnace temp. control
TC 814	Analogue temp. controller	Steam generator temp. control
FC 304	Check valve	Air flow control
FC 311	2-way ball valve	Air flow control
FC 313	Rotameter needle valve	Air flow control
FI 313	Rotameter	Air flow reading
FI 806	Rotameter	NH mix flow reading
PC 401	Regulator valve	H_2 flow control
FC 403	2-way ball valve	H_2 flow control
FC 407	Check valve	H_2 flow control
PC 409	Regulator valve	CO_2 flow control
FC 414	Check valve	CO_2 flow control
FC 415	2-way ball valve	CO_2 flow control
PC 419	Regulator valve	Reformate flow control
FC 427	2-way ball valve	Reformate flow control
FC 428	Needle valve	Reformate flow control
FC 431	Check valve	Reformate flow control
FC 803	2-way ball valve	NH mix flow control
FC 806	Rotameter needle valve	NH mix flow control
FC 807	Check valve	NH mix flow control
FC 809	3-way ball valve	Water flow control
FC 817	Check valve	Water flow control
FC 818	Centrifugal blower	Exhaust stream flow control
PC 309	Regulator valve	Air flow control
PC 801	Regulator valve	NH mix flow control
PC 810	Pressure releif valve	Water feed line pressure releif
PC 820	Pressure relief valve	Pressure releif for NH mix bypass to anode
PI 416	Pressure guage	Main anode feed line pressure reading
AX 207	2-way ball valve	Anode chamber exhaust sample port
AX 423	2-way ball valve	Main anode feed line sampling port
AX 441	2-way ball valve	Main anode feed line sampling port

APPENDIX C: CALCULATION OF THE SIMULATED REFORMATE AND SIMULATED DRY REFORMATE COMPOSITOINS

The simulation used to calculate the simulated reformate and simulated dry reformate compositions discussed section 3.1 is outlined below in figure C.1.

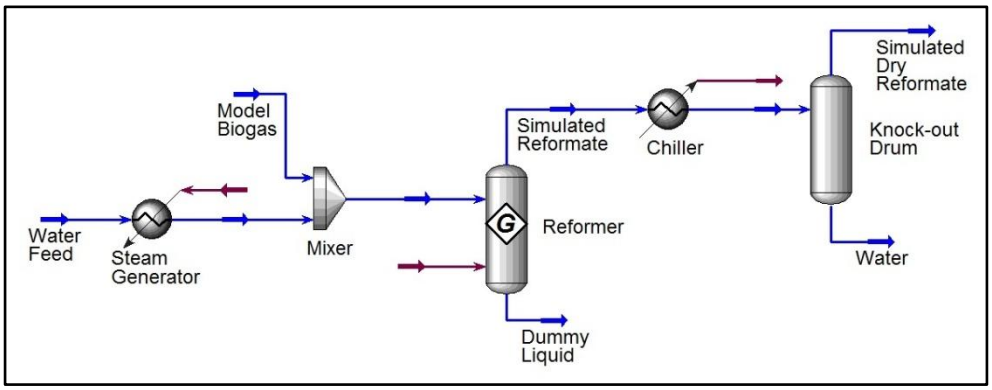

Figure C.1. UniSim Design™ simulation used to estimate the simulated reformate and simulated dry reformate compositions.

The simulation was developed to provide a quick estimate for the reformate composition exiting the fuel processor in the eventual pilot plant and the dry composition of the mixture (simulated dry reformate). Therefore, only sub-components necessary to carry out the calculation have been included. The process begins with the mixing of steam and a model biogas at a steam-to-carbon ratio of 2.76, which is a value typically used for steam reforming [25]. The composition of the model biogas is provided in table C.1 below. The mixture is then fed to the reformer which calculates the equilibrium composition of the reacting mixture. The gas stream exiting the reformer was taken as the simulated reformate composition and is listed in table C.1. The simulated reformate is then cooled to 15°C by a hypothetical chiller and proceeds on to a knock-out drum where water content is removed. The gas stream exiting the knock-out drum is taken as the simulated dry reformate composition and is listed in table C.1.

A gas cylinder with the simulated dry reformate composition was ordered from a chemical manufacturing company for the purpose of carrying out the experimental component of this work. Note that the only species considered for the cylinder mixture were H_2, CO, CO_2, and N_2. The residual amounts of other

species were omitted. H_2S would not likely appear in the reformate stream because the VOCs which gave rise to its formation in the reformer in this simulation would have been removed upstream in the purification stages.

During the experiments, the simulated reformate mixture was reconstituted by adding an appropriate amount of steam to the cylinder mixture.

Table C.1. Model biogas, simulated reformate and simulated dry reformate compositions.

	Stream					
	Model Biogas		Simulated Reformate		Simulated Dry Reformate	
Species	Molar Flow	Mole Fraction	Molar Flow	Mole Fraction	Molar Flow	Mole Fraction
CH_4	3.5874	0.5979	0.0038	0.0001	0.0038	0.0002
CO_2	2.0533	0.3422	3.1708	0.1008	3.1698	0.1616
O_2	0.0885	0.0148	0.0000	0.0000	0.0000	0.0000
N_2	0.1416	0.0236	0.1416	0.0045	0.1416	0.0072
H_2O	0.0006	0.0001	12.1448	0.3862	0.3223	0.0164
CO	0.0006	0.0001	3.0932	0.0984	3.0932	0.1577
H_2	0.0006	0.0001	12.8313	0.4081	12.8313	0.6540
H_2S	0.0046	0.0008	0.0576	0.0018	0.0575	0.0029
Toluene	0.0307	0.0051	0.0000	0.0000	0.0000	0.0000
Dimethylsulphide	0.0519	0.0086	0.0000	0.0000	0.0000	0.0000
1-Butanol	0.0132	0.0022	0.0000	0.0000	0.0000	0.0000
n-Decane	0.0149	0.0025	0.0000	0.0000	0.0000	0.0000
p-Cymene	0.0098	0.0016	0.0000	0.0000	0.0000	0.0000
Napthalene	0.0006	0.0001	0.0000	0.0000	0.0000	0.0000
SO_2	0.0006	0.0001	0.0000	0.0000	0.0000	0.0000
COS	0.0006	0.0001	0.0001	0.0000	0.0001	0.0000
2-Propanol	0.0006	0.0001	0.0000	0.0000	0.0000	0.0000
Total	6.0000	1.0000	31.4432	1.0000	19.6196	1.0000

APPENDIX D: EXPERIMENTAL DATA

Table D.1. Experimental data collected during the experiments formatted for the empirical cell model calibration.

Sample #	i_{cell} (mA·cm^{-2})	T_{cell} (°C)	$\bar{p}_{H2}$ (bar)	$\bar{p}_{H2O}$ (bar)	$\bar{p}_{O2}$ (bar)	V_{cell} (V)
1	25	803	0.35	0.45	0.21	0.85
2	25	807	0.33	0.48	0.21	0.85
3	50	811	0.27	0.54	0.21	0.77
4	50	811	0.30	0.51	0.21	0.78
5	50	810	0.33	0.48	0.21	0.79
6	50	804	0.36	0.45	0.21	0.79
7	78	815	0.28	0.53	0.21	0.72
8	78	821	0.28	0.53	0.21	0.73
9	78	820	0.30	0.51	0.21	0.74
10	78	815	0.33	0.47	0.21	0.75
11	78	801	0.36	0.45	0.21	0.75
12	108	807	0.28	0.53	0.21	0.67
13	108	806	0.30	0.51	0.21	0.68
14	108	797	0.33	0.47	0.21	0.68
15	108	785	0.36	0.45	0.21	0.68
16	138	787	0.30	0.51	0.21	0.60
17	108	787	0.30	0.51	0.21	0.65
18	108	795	0.30	0.51	0.21	0.66
19	108	801	0.30	0.51	0.21	0.67
20	78	807	0.30	0.51	0.21	0.73
21	50	814	0.30	0.51	0.21	0.79
22	25	815	0.35	0.46	0.21	0.85

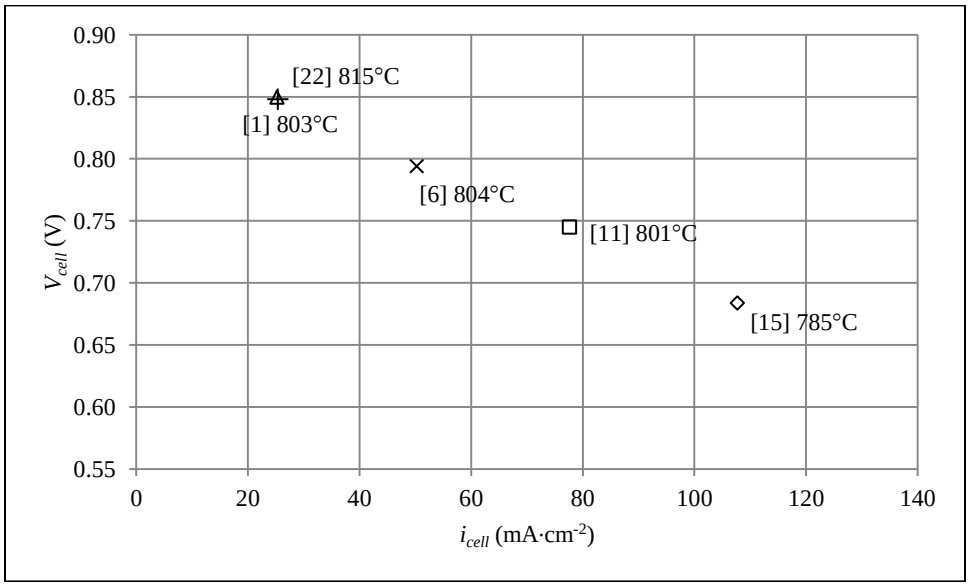

Figure D.1. Graphical depiction of all experimental data points collected at 27% fuel utilization. The sample numbers appear in square brackets. Note: samples 1 and 22 appear overlaid in the figure; sample 1 is represented by a triangle and sample 22 as a cross.

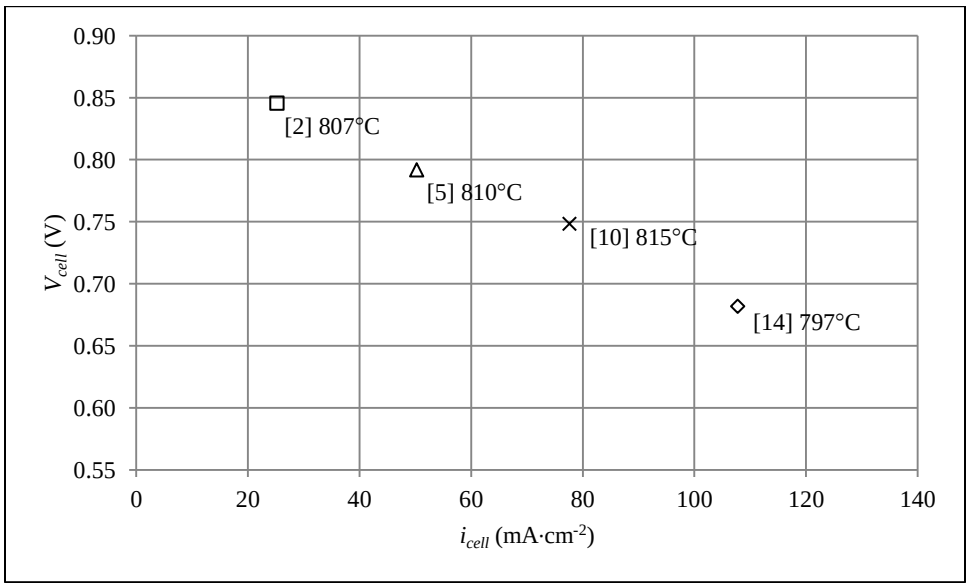

Figure D.2. Graphical depiction of all experimental data points collected at 38% fuel utilization.

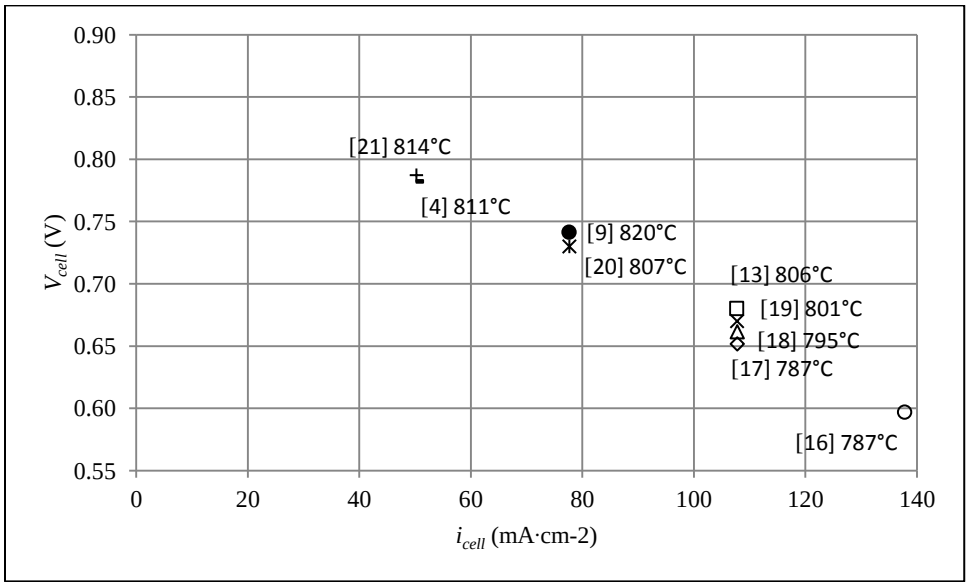

Figure D.3. Graphical depiction of all experimental data points collected at 54 % fuel utilization.

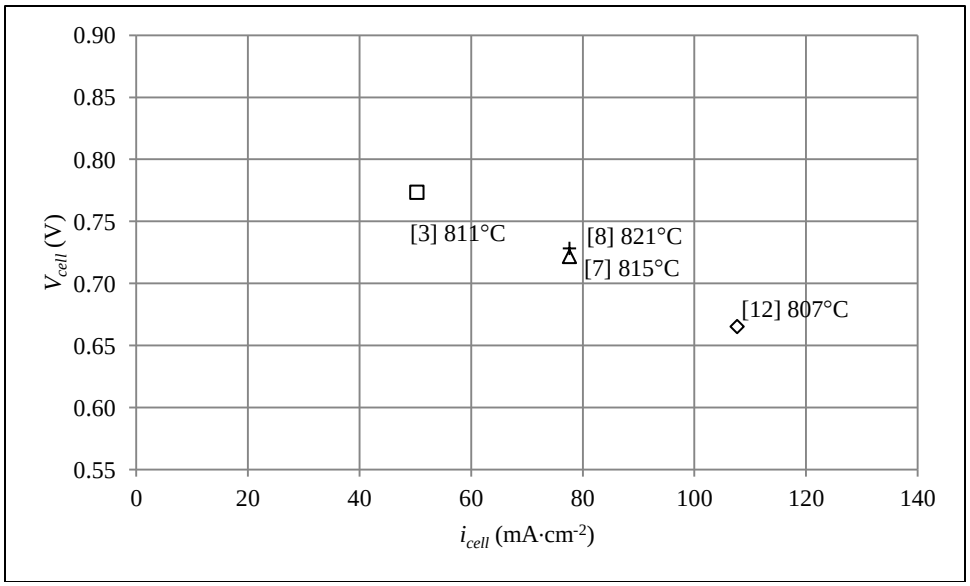

Figure D.4. Graphical depiction of all experimental data points collected at 65 % fuel utilization.

APPENDIX E: SOLVER SETTINGS

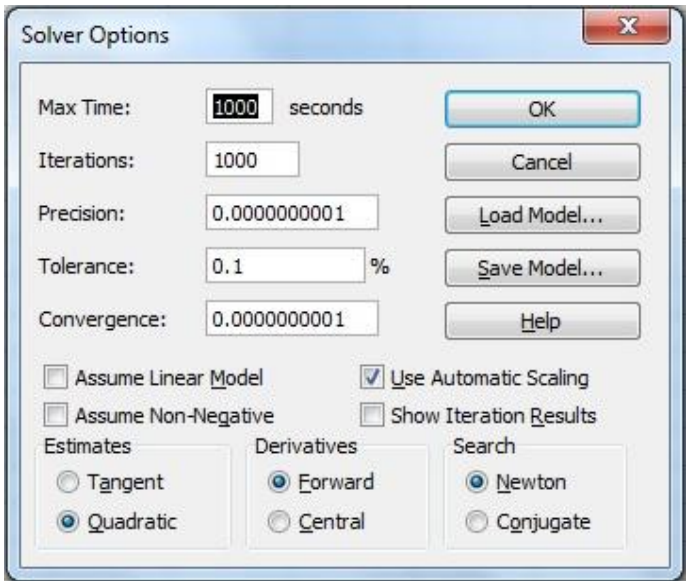

Figure E.1. SOLVER Options settings used for the empirical cell model calibrations.

Table E.1. Constraints placed on the values of C_i, C_T, and C_a in the SOLVER Parameters settings.

Regression Coefficient	Constraint
C_i	≤ 0
C_T	≥ 0
C_a	≥ 0

APPENDIX F: EFFECT OF OMITTING HIGHER HYDROCARBONS ON THE PRE-REFORMER

In this section, the effect of omitting the higher hydrocarbons from the biogas feed is investigated for the pre-reformer. To facilitate the analysis, the pre-reformer sub-component model has been isolated from the main process model as a separate simulation. The sub-component model is shown in figure F.1.

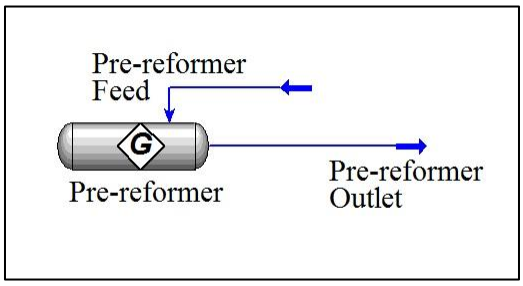

Figure F.1. Isolated sub-component model used to study the influence of higher-hydrocarbons on the pre-reformer.

Subsequently, the sub-component model is run through two simulation cases; one in which the higher-hydrocarbons are omitted and one in which they are included based on measurements made on the Ravensview biogas. In both cases, the reference conditions of Section 3.3.3 serve as the basis for the calculation.

To begin, a ratio was determined for the Ravensview biogas; this ratio relates the moles of higher-hydrocarbons to the moles of dry biogas, and is symbolized as $r_{decane/biogas}$. OSB Services, Inc. (2009) [76] report the most recent TVOC measurement as 1016 $mg \cdot m^{-3}$. However, this value includes all VOC compounds (siloxane, sulphur species, halogenated species, etc.) and specific loadings for the various species were not provided. Chromatography analysis revealed that the biogas contained negligible amounts of low to mid boiling point VOCs (ethane, propane, propylene, etc.), but high boiling point compounds such as toluene, nonane, decane, limonene, undecane were identified. In the extreme case, the greatest fuel processing demand will be placed on the pre-reformer when all VOCs are assumed to be high boiling point, reformable (non-poisoning) species. In this calculation, n-decane is taken as the surrogate species. Therefore,

if the biogas is assumed to have a loading of 1016 mg·m^{-3} n-decane, the number of moles present in 1 m^3 of biogas will be:

$$n_{decane} = \frac{1016\ mg\ decane}{1\ m^3\ biogas} \times \frac{1\ g}{1000\ mg} \times \frac{1\ mol\ decane}{142.29\ g}$$

$$= 0.007140\ mol\ decane\ per\ m^3\ biogas$$

If the temperature and pressure of the gas sample bag are assumed to be 25°C and 1 atm, respectively, the number of moles in 1 m^3 of biogas will be:

$$n_{bioags} = \frac{101325\ Pa}{(8.314\ J \cdot mol^{-1} \cdot K^{-1})(273.15\ K + 25\ K)}$$

$$= 40.9\ mol\ biogas\ per\ m^3\ biogas$$

Therefore,

$$r_{decane/biogas} = \frac{n_{decane}}{n_{biogas}} = 0.00017468\ mol\ decane\ per\ mol\ biogas$$

The $r_{decane/biogas}$ ratio is used to determine the amount of n-decane to be passed with the biogas for the simulation case in which higher hydrocarbons are included. The simulation results are shown below in table F.1.

Table F.1. Summary of the simulations carried out to study the influence of higher hydrocarbons on the pre-reformer.

	Higher-hydrocarbons Omitted	Higher-hydrocarbons Included
Pre-reformer Feed Conditions		
CH_4 flow rate ($mol \cdot s^{-1}$)	4.67E-03	4.67E-03
CO_2 flow rate ($mol \cdot s^{-1}$)	2.74E-03	2.74E-03
H_2O flow rate ($mol \cdot s^{-1}$)	2.07E-02	2.07E-02
n-decane flow rate ($mol \cdot s^{-1}$)	0	1.29E-06
$r_{H2O/C}$	2.8	2.8
Pre-reformer feed temperature (°C)	550	550
Pre-reformer Outlet Conditions		
CH_4 flow rate ($mol \cdot s^{-1}$)	3.64E-03	3.65E-03
CO_2 flow rate ($mol \cdot s^{-1}$)	3.71E-03	3.71E-03
H_2O flow rate ($mol \cdot s^{-1}$)	1.88E-02	1.87E-02
H_2 flow rate ($mol \cdot s^{-1}$)	4.04E-03	4.04E-03
CO flow rate ($mol \cdot s^{-1}$)	5.89E-05	5.91E-05
n-decane flow rate ($mol \cdot s^{-1}$)	0	0
Pre-reformer outlet temperature (°C)	395.6	395.6

Table E.1 shows that the additional hydrocarbons do little to influence the pre-reformer outlet conditions; for example, the molar flow rates and temperature are largely unaffected. Therefore, although the pre-reformer can be useful for converting the higher-hydrocarbons omitting them in the current work is not expected to impact the reported system performance.